Synthesis and Development of Hydrophilic Iron Oxide Nanoparticles for Biomedical Applications

by

He Wei

B. S. in Chemistry
Department of Chemical Physics, University of Science and Technology of China
Hefei, Anhui Province, P. R. China (2009)

Submitted to the Department of Chemistry
in Partial Fulfillment of the Requirements for the Degree of

Doctor of Philosophy

at the

MASSACHUSETTS INSTITUTE OF TECHNOLOGY

September 2014

Signature redacted

Signature of Author _____
Department of Chemistry
August 15, 2014

Signature redacted

Certified by _____
Moungi G. Bawendi
Professor of Chemistry
Thesis Supervisor

Signature redacted

Accepted by _____
Robert W. Field
Chairman, Departmental Committee on Graduate Students

This doctoral thesis has been examined by a committee of the Department of Chemistry as follows:

Professor Keith A. Nelson — Signature redacted
Chairman

Professor Moungi G. Bawendi — Signature redacted
Thesis Supervisor

Professor Robert G. Griffin — Signature redacted
Department of Chemistry

Synthesis and Development of Hydrophilic Iron Oxide Nanoparticles
for Biomedical Applications

by

He Wei

Submitted to the Department of Chemistry on August 15, 2014 in Partial Fulfillment
Of the requirements for the Degree of Doctor of Philosophy in Chemistry

ABSTRACT

Uniformly sized superparamagnetic iron oxide nanoparticles (SPIONs) with inorganic diameters of 3-35 nm were synthesized. New surface ligand coatings were designed and synthesized, and the resulting hydrophilic SPIONs in biological buffers were found to be compact, stable, highly magnetic, and biocompatible. Furthermore, the hydrophilic SPIONs were stable in vitro in serums and cells as well as in vivo in mice. Functionalized SPIONs demonstrated the ability of specific labeling. Finally, the hydrophilic SPIONs have potential as a non-toxic alternative to Gadolinium based contrast agents for T_1-weighted magnetic resonance imaging (MRI) and they have shown potential in multicolor MRI as well as magnetic particle imaging.

Thesis Supervisor: Moungi G. Bawendi
Title: Professor of Chemistry

1. Chapter 1: Introduction to magnetic nanoparticles

1.1 Introduction to magnetism

1.1.1 Introduction to magnetic field

A magnetic field in space is characterized by its magnetic vector $\vec{B}$ or its field strength H (when the orientation of a magnetic field is not considered). A magnetic field can also be described by its magnetic vector potential $\vec{A}$ in space, in which the magnetic vector $\vec{B} = \nabla \times \vec{A}$. For example, a magnetic field can be generated by a time-dependent electric field, a permanent magnet, or an electromagnet. However, magnetic field lines are not visible. In order to show the spatial distribution of magnetic field lines, a magnetic material is needed. As shown in Figure 1.1a and b, ~50 μm sized magnetite (Fe_3O_4) powders on a piece of white paper were used to show the magnetic field lines that are created by a permanent magnet beneath the white paper.

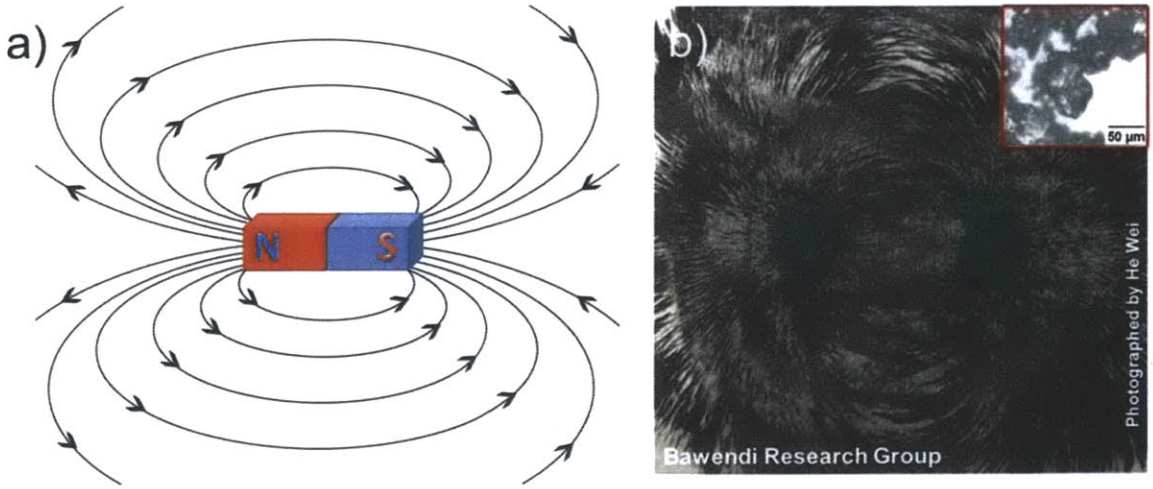

Figure 1.1 a) Magnetic field lines of a permanent magnet and b) a visualization of magnetic field lines using magnetite powders. (Inset: an optical transmission image of magnetite powders.)

1.1.2 Introduction to the types of magnetism

Magnetism describes the interaction between matters and a magnetic field. Based on the type of interactions, magnetism has been categorized into six groups: diamagnetism, paramagnetism, ferromagnetism, anti-ferromagnetism, ferrimagnetism, and superparamagnetism. Accordingly, materials that have the above properties are called diamagnetic, paramagnetic, ferromagnetic, anti-ferromagnetic, ferrimagnetic, and superparamagnetic materials.

When placed in an external magnetic field, diamagnetic materials such as bismuth will generate a magnetic field with its direction opposing to the external magnetic field. This effect will cause diamagnetic materials to be repelled by the external magnetic field. In contrast to diamagnetic materials, paramagnetic materials such as Gadolinium-based compounds (T_1-weighted MRI contrast agents) will be attracted by the external magnetic field. Unlike diamagnetic and paramagnetic materials, ferromagnetic (e. g., iron and cobalt metals) and ferrimagnetic (e.g., magnetite) materials have non-zero total magnetic moments and they will be magnetized by applying an external magnetic field; even if the external magnetic field is removed afterwards, they will retain their magnetization. A new magnetic field in opposition to the previous external magnetic field is required to neutralize their magnetization and the field strength required is called the coercivity (H_C). Antiferromagnetic materials such as hematite (α-Fe_2O_3) have zero total magnetic moments without an external magnetic field; when an external magnetic field is applied, antiferromagnetic materials may show non-zero total magnetic moments. The difference between ferromagnetic, ferrimagnetic, and antiferromagnetic materials is the alignment of magnetic moments in a crystal unit cell.

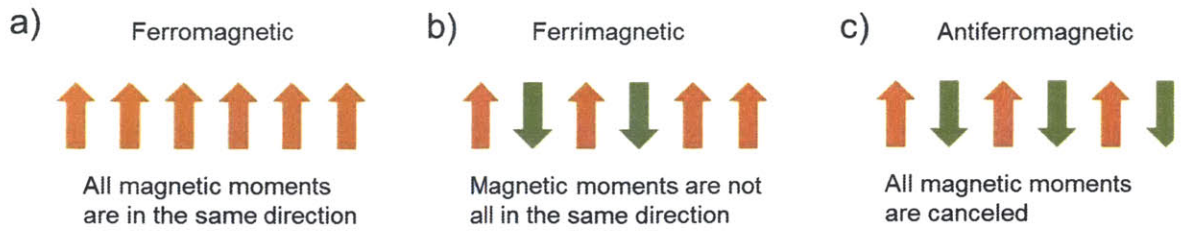

Figure 1.2 a) In a crystal unit cell of ferromagnetic materials, all magnetic moments are aligned to the same direction; b) in a crystal unit cell of ferrimagnetic materials, magnetic moments with opposing directions exist, but the total magnetic moment is non-zero; and c) in a crystal unit cell of antiferromagnetic materials, neighboring magnetic moments are in opposing directions, so the total magnetic moment is zero.

Figure 1.2a, b, and c show the different alignments of magnetic moments in ferromagnetic, ferrimagnetic, and antiferromagnetic materials, respectively. Figure 1.2a shows that all magnetic moments in a crystal unit cell of ferromagnetic materials point to the same direction; as a result, these magnetic moments will be added up to a large total magnetic moment. Figure 1.2b shows that not all magnetic moments in a crystal unit cell of ferrimagnetic materials point to the same direction, and thus the sum of these magnetic moments will be a relatively small total magnetic moment. Figure 1.3b illustrates that, in contrast to ferromagnetic materials, neighboring magnetic moments are with opposing directions and hence the sum of these magnetic moments will vanish, giving rise to a zero total magnetic moment.

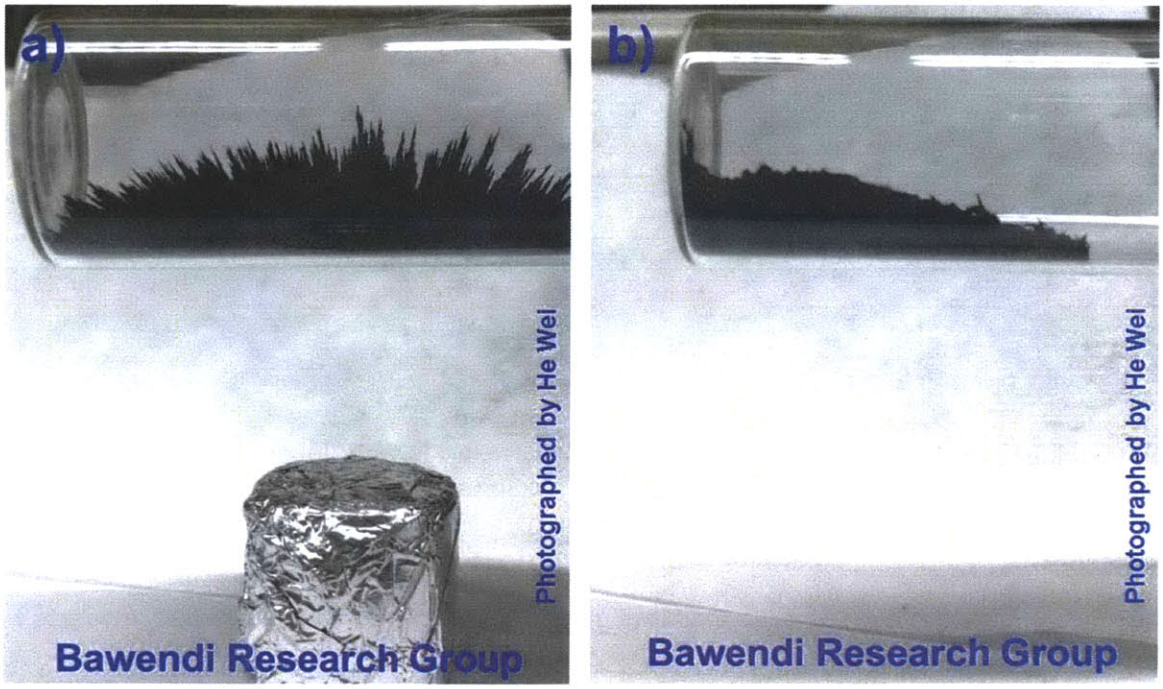

Figure 1.3 a) Magnetite powders were attracted by a permanent magnet, aligning themselves to the magnetic field lines; and b) upon the removal of the permanent magnet, magnetite powders were no longer aligned.

In Figure 1.3a, in the presence of a permanent magnet, ~50 μm sized ferrimagnetic magnetite powders that were confined in a 40-mL cylindrical glass vial aligned themselves to the magnetic field lines, showing a needle-like appearance. When the permanent magnet is removed, the ferrimagnetic magnetite powders were no longer strongly attracted and thus the needle-like appearance collapsed.

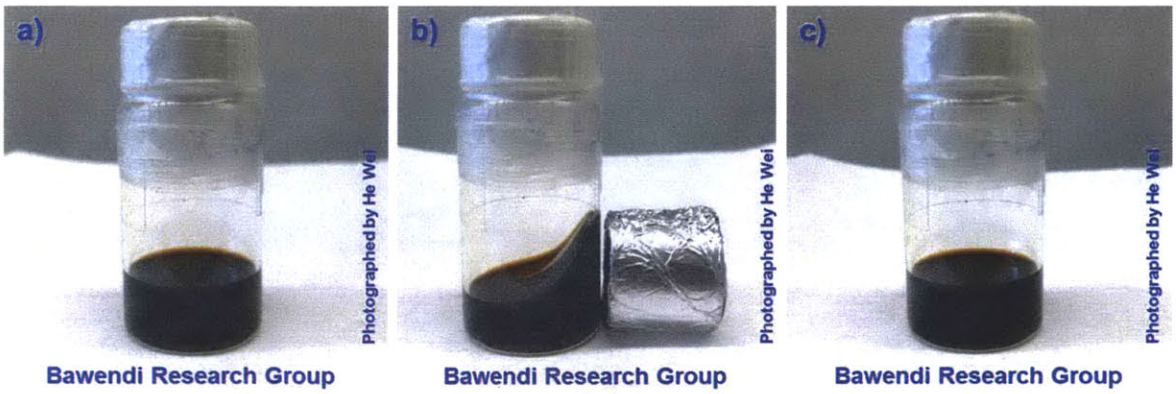

Figure 1.4. a) Superparamagnetic maghemite nanoparticles dispersed in a hexane solution; b) superparamagnetic maghemite nanoparticles in a hexane solution were attracted by a permanent magnet; and c) upon the removal of the permanent magnet, superparamagnetic maghemite nanoparticles in a hexane solution immediately returned to their initial non-magnetized state.

The last type of magnetism is superparamagnetism, in which the magnetic moments of superparamagnetic materials can freely flip their directions at certain temperatures. Nanometer sized (e.g., 2.5-35 nanometers) magnetite and maghemite (γ-Fe_2O_3) particles are good examples of superparamagnetic materials at room temperature. As shown in Figure 1.4a, ~10 nanometers (nm) sized superparamagnetic maghemite nanoparticles were well-dispersed in a hexane solution in their initial non-magnetized state. As shown in Figure 1.4b, when applying a permanent magnet, superparamagnetic maghemite nanoparticles were immediately magnetized. Therefore, the black-brown hexane solution containing superparamagnetic maghemite nanoparticles moved towards the permanent magnet. In Figure 1.4c, when the permanent magnet is removed, the magnetic moments of superparamagnetic maghemite nanoparticles can freely flip their directions at room temperature; then these superparamagnetic maghemite nanoparticles immediately randomized their magnetic moments to return to the initial non-magnetized state, resulting in a vanishing total magnetic moment.

1.1.3 Temperature-dependence and size-dependence of magnetism

The magnetic behavior of materials depends on several parameters such as temperature and size. Generally, permanent magnetizations become weaker at higher temperatures. When reaching a critical temperature, the permanent magnetization of materials will disappear. For ferromagnetic and ferrimagnetic materials, this critical temperature is called the Curie temperature; for antiferromagnetic materials, this critical temperature is called the Neel temperature. When the environment temperature is higher than Curie temperature or Neel temperature, ferromagnetic, ferrimagnetic, and antiferromagnetic materials will all become paramagnetic.

The size-dependence of the magnetism of materials is due to the size-dependence of magnetocrystalline anisotropy energy E_{MA}, which is defined as the energy that takes to change the directions of magnetic moments in materials. To the lowest order approximation, E_{MA} is a linear function of the magnetic domain's volume V. When a magnetic domain's volume V becomes small enough (e. g., on the order of nanoparticles' volume), E_{MA} can be on the order of k_BT or even smaller than k_BT, where k_B is the Boltzmann constant and T is the environment temperature. In this case, the magnetic moments of ferromagnetic and ferrimagnetic materials will be able to freely flip their directions, and this is the origin of superparamagnetism.

1.2 The definition and types of magnetic nanoparticles

1.2.1 The definition of magnetic nanoparticles

Nanoparticles are usually defined as crystals with their sizes of a few nanometers to a hundred nanometers (nm). Nanoparticles can show novel properties that are different from bulk materials even with the same chemical compositions. For example, cadmium selenide (CdSe) nanoparticles (a. k. a. quantum dots) have photoluminescence properties due to the nanoscale confinement of electrons. Silver (Ag) nanoparticles have surface plasmon resonance properties owing to the collective oscillation of conduction electrons on the nanoscale.

Magnetic nanoparticles are defined as nanoparticles that are made of magnetic materials. They are also good examples of nanoparticles showing novel properties unlike their bulk materials. For instance, bulk magnetite and maghemite are both ferrimagnetic, while magnetite nanoparticles and maghemite nanoparticles can both be superparamagnetic.

1.2.2 The types of magnetic nanoparticles

Magnetic nanoparticles (NPs) can be divided into ferrite NPs, metallic NPs, and core/shell NPs.

Magnetic ferrite NPs include maghemite (γ-Fe_2O_3) NPs,[1] magnetite (Fe_3O_4) NPs,[2] cobalt ferrite ($CoFe_2O_4$) NPs,[3] manganese ferrite ($MnFe_2O_4$) NPs,[4] nickel ferrite ($NiFe_2O_4$) NPs [5] and so on. Magnetic ferrite NPs are highly stable and they have been extensively studied.

Magnetic metallic NPs include iron (Fe) NPs, cobalt (Co) NPs, nickel (Ni) NPs, iron platinum alloy (FePt) NPs,[6] cobalt platinum alloy (CoPt) NPs[7] and so on. Magnetic metallic NPs are well known for their high saturation magnetizations.

Magnetic core/shell NPs include iron/iron oxide core/shell ($Fe@Fe_3O_4$) NPs[8] as well as cobalt/silica core/shell ($Co@SiO_2$) NPs[9] and so on. The crystalline oxide shells are commonly used to protect the metallic cores, as their oxidation by air can lead to lower saturation magnetizations.[8,9]

1.3 Biomedical applications of magnetic nanoparticles

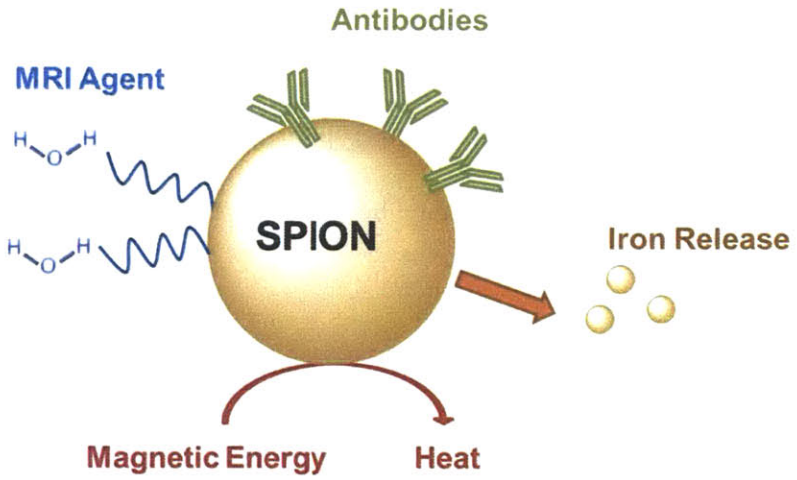

Figure 1.5 A schematic show of biomedical applications of superparamagnetic iron oxide nanoparticles (SPIONs)

1.3.1 Magnetic resonance imaging and magnetic particles imaging

As shown in Figure 1.5, Magnetic nanoparticles (NPs) have been used as contrast agents for T_1-weighted magnetic resonance imaging (positive MRI) and T_2-weighted MRI (a. k. a. negative MRI) in biological research and in the clinic.[10] In these cases, magnetic NPs are able to change the relaxation times of water protons in MRI. In T_1-weighted (T_2-weighted) MRI, water protons close to magnetic NPs will show brighter (darker) signals compared to water protons far from magnetic NPs. Therefore, contrast-enhanced MR images of brain, liver, spleen, bone marrow, as well as tumors can be obtained by intravenous injection of hydrophilic magnetic NPs. There exist negative MRI contrast agents based on magnetic NPs such as Feridex® and Resovist® that are approved by the U.S. Food and Drug Administration (FDA).

Magnetic particles imaging (MPI),[11] which uses the nonlinear magnetization-field (M-H) response of magnetic NPs, is a novel imaging technique currently under development. Superparamagnetic iron oxide NPs (SPIONs) such as Resovist® can be tracked by MPI in vitro and in vivo with near-zero backgrounds and high spatial resolutions. Potential SPIONs-based MPI pre-clinical and clinical applications may be angiography, tagged-cell detections, and cancer detections.[12]

1.3.2 Targeted drug delivery

In contrast to conventional therapeutic strategies, drugs can be attached to magnetic NPs with specific targeting moieties. These drug-NP complexes can be directed to target sites when their specific targeting moieties find receptors or when they are manipulated by an magnetic field

gradient;[13] this results in a higher concentration of drug-NP complexes at target sites (such as organs and tissues) and hence the efficacy of drugs are expected to be improved.

1.3.3 Magnetic separation

Magnetic separation using magnetic NPs enables sorting of microscopic biological targets (e.g., malignant tumor cells). The surfaces of magnetic NPs are first modified chemically or biologically in order to endow magnetic NPs with a specific labeling ability. The binding receptors of biological targets will then be labeled by the above modified magnetic NPs during an incubation process. Afterwards, a high magnetic field can be applied in order to concentrate and collect the modified magnetic NPs along with their labeled biological targets.[14]

1.3.4 Hyperthermia treatment

As shown in Figure 1.5, hyperthermia treatment (thermo- therapy) is usually defined as heating the temperature of a body region up to 41-46 ^{o}C for damaging or killing cancerous cells.[15] Hyperthermia treatment can have more specificity than radio- and chemo- therapies, which are efficient in destroying cancer cells but at the same time have side effects such as anemia and infections.[16] Under an alternating magnetic field, magnetic NPs are able to convert electromagnetic energy into heat energy through the excitation and relaxation of their magnetizations.[17] This property has rendered magnetic NPs as excellent materials for hyperthermia treatment in biomedical research and pre-clinical trials.[18,19]

1.3.5 Iron supplementation

As shown in Figure 1.5, ferrite magnetic NPs are iron-rich; hence they can be used as iron supplements for treating iron deficiency anemia. Ferrite magnetic NPs are integrated nanostructures and thus ferrite magnetic NPs have the advantage of reduced free iron release compared to conventional injectable iron supplements, which otherwise may introduce a high concentration of free iron in the bloodstream that can possibly lead to a higher chance of infections and injuries to organs.[20] For example, Feraheme®, which is a type of hydrophilic iron oxide magnetic NP, is a U.S. Food and Drug Administration (FDA) approved iron supplementation for intravenous administration.

2. Chapter 2: Synthesis of high-quality inorganic cores of magnetic nanoparticles

2.1 Introduction to synthetic methods and motivation

Superparamagnetic iron oxide nanoparticles (SPIONs) are single magnetic domain maghemite (γ-Fe_2O_3) and magnetite (Fe_3O_4) particles with their sizes of a few nanometers (nm) to a hundred nanometers. SPIONs are capable of distinguishing themselves from other types of magnetic nanoparticles (NPs) that are made from different materials, due to SPIONs' superior stability in organic solvents and aqueous media, monodisperse (a. k. a. uniformly sized) cores after synthesis, high saturation magnetizations, and potentially minimized non-toxicity towards living animals.[21] SPIONs can be synthesized by several methods, including co-precipitation, hydrothermal, sol-gel, and high-temperature decomposition techniques and so on.[22]

2.1.1 Co-precipitation method

In the co-precipitation method,[23] for example, an aqueous solution mixture containing ferrous (Fe^{2+}) and ferric (Fe^{3+}) salts is added drop-wise into a aqueous alkaline solution (e.g., a sodium hydroxide solution) under the protection of nitrogen gas. The reaction occurs at room temperature and the resulting SPIONs (magnetite in this case) are separated from its reaction mixture by an external magnetic field. After being washed by water and neutralized by hydrochloride aqueous solution, the colloidal SPIONs are purified by centrifugations.

2.1.2 Hydrothermal method

In the hydrothermal method,[24] for instance, an aqueous solution of ferrous sulfate in the presence of n-decanoic acid or n-decylamine is capped in a reactor and then heated to 473 K. After 10 minutes (mins) of reaction, the reactor is quenched by a room-temperature water bath and the resulting solid products are purified by centrifugations using water and ethanol. It is revealed that the presence of n-decanoic acid gives rise to hematite (α-Fe_2O_3) NPs while n-decylamine gives rise to SPIONs (magnetite in this case).

2.1.3 Sol-gel method

In the sol-gel method,[25] for example, tetraethylorthosilicate (TEOS) is added into an ethanol solution of ferric nitrate nonahydrate ($Fe(NO_3)_3 \cdot 9H_2O$) in order to make the iron-containing silica sol-gel matrix, which is then incubated for 7 days at 45 °C. This treated iron-containing silica matrix is then heated for 10 hours (hrs) at 400 °C in air and SPIONs (maghemite in this case) are formed in the silica matrix. It may be useful to note that the substitution of ferric nitrate nonahydrate ($Fe(NO_3)_3 \cdot 9H_2O$) into ferric chloride hexahydrate ($FeCl_3 \cdot 6H_2O$) in this sol-gel method would result in hematite NPs.

2.1.4 High-temperature decomposition method

In the high-temperature decomposition (HTD) method, organometallic precursors are used to produce SPIONs with narrow size distribution and high crystallinity. The HTD method is pivotal and dominant for uniform-sized and high saturation magnetization (M_s) SPIONs synthesis.[1, 26]

Commonly used organometallic precursors include iron(0) pentacarbonyl,[27] iron(III) oleate,[27] iron(III) acetylacetonate[2] and so on. For example, hydrophobic SPIONs of diameters ranging from 3-25 nanometers (nm) can be synthesized by the high-temperature decomposition of iron pentacarbonyl in the presence of oleic acid or stearic acid native ligands in a di-octyl ether solvent, followed by an mild oxidation using trimethylamine N-oxide.[28] Iron oleate is a more environmentally friendly iron precursor that can also decompose at high temperatures to form hydrophobic SPIONs with or without the use of oxidizing agents.[27] Furthermore, iron oleate is able to serve as an iron source to continuously grow on existing SPIONs, where the growth of iron oleate on SPIONs of diameters ranging from 4-11 nm gives rise to larger SPIONs of diameters ranging from 6-15 nm.[29]

2.1.5 Applications of different sized magnetic nanoparticles

Different biomedical applications require the corresponding SPIONs to have different sizes. For instance, T_1-weighted magnetic resonance imaging (MRI) prefers small SPIONs. In contrast, T_2-weighted MRI and magnetic particles imaging (MPI) both prefer large SPIONs. Moreover, large SPIONs generally have higher M_s than small SPIONs while small SPIONs are more easily dispersed in solvents than large SPIONs. Therefore, it is imperative to precisely control the size of SPIONs in synthesis and to produce monodisperse SPIONs in a large size range.

2.1.6 Motivation to the synthesis of different sized magnetic nanoparticles

The production of high-quality SPIONs is essential for their biomedical applications. For instance, good magnetic and crystalline properties are both crucial factors for high-performance SPIONs in the applications of magnetic separations and magnetic resonance imaging. As discussed in Chapter 1, the size and the corresponding volume play important roles in the superparamagnetism of SPIONs. Fortunately, the size and volume of SPIONs can be well-controlled by synthetic conditions. Therefore, it is imperative to investigate and optimize the synthesis of different sized SPIONs.

The synthesis of medium-sized SPIONs using high-temperature decomposition (HTD) methods has been extensively studied in the last decade.[30] With the development of SPION-based T_1-weighted MRI, the synthesis of small-sized SPIONs using HTD methods has attracted more and more attentions in recent years.[31] The synthesis of 16-25 nm large-sized SPIONs using HTD methods has also been reported;[28] however, the synthesis of large-sized SPIONs (inorganic diameter > 25 nm) using HTD methods is so far lagging behind. In the following sections of this chapter, we will first describe our HTD method of synthesizing small-sized and medium-sized SPIONs, with modifications to previously reported HTD methods, and then we will report our new HTD method of synthesizing large-sized (especially >25 nm) SPIONs.

2.2 Synthesis of 2.5-6 nm magnetic nanoparticles

With modifications to previously reported methods,[32,27] the first step of synthesizing a size series of monodisperse SPIONs of inorganic diameters ranging from 2.5-6 nm involves the decomposition of organometallic iron precursors at a specific reaction temperature. The specific reaction temperature, which is the key to control the size of as-synthesized SPIONs, is the boiling point of corresponding reaction solvent.[33] Other factors that can affect the size of as-synthesized SPIONs include the concentration of iron precursors, the concentration of native organic ligands, the speed of heating up to the reaction temperature, and the growth (incubation) time at the reaction temperature, and other variables. The reaction solvent can be a mixture of 1-tetradecene (1-TDE), 1-hexadecene (1-HDE), and 1-octadecene (1-ODE), in which the boiling point of reaction solvent is easily modulated by the ratio of its components. 1-TDE, 1-HDE, and 1-ODE have boiling points of ~251 °C, ~274 °C, ~314 °C;[34,35] therefore, the mixed solvent can have a tunable boiling point between ~251 °C and ~314 °C. The reaction solvent can also be a single component such as di-octyl ether, which has an appropriate boiling point of ~287 °C.[35]

In addition to the specific reaction temperatures, native organic ligands play an important role in the formation of SPIONs. After SPIONs are formed, the native organic ligands also coat on the surfaces of as-synthesized SPIONs and ensure the solubility of SPIONs in organic solvents such as hexanes and chloroform. Oleic acid, stearic acid, and oleylamine are commonly used native organic ligands.

In the presence of native organic ligands, the iron precursors in a certain solvent will be slowly heated to the specific reaction temperature (i. e. the boiling point of solvent used) and be kept at this temperature to form SPIONs. Interestingly, different types of iron precursors will

decompose into different types of nanoparticles (NPs). For example, iron pentacarbonyl ($Fe(CO)_5$) would result in the formation of metal iron NPs.[36] In contrast, iron acetylacetonate ($Fe(acac)_3$) would result in the formation of magnetite NPs.[2] In another case, iron oleate ($Fe(oleate)_3$) would result in the formation of mixed maghemite-magnetite NPs.[27] Metal iron NPs are highly magnetic but unfortunately they are unstable in air at room temperature.[37] Therefore, if iron pentacarbonyl is used as the precursor to synthesize SPIONs, a mild oxidizing agent such as trimethylamine N-oxide is usually employed to oxidize the intermediate metal iron NPs into maghemite NPs.[26] If iron oleate or iron acetylacetonate is used as the precursor, such additional oxidizing process is not necessary; however, trimethylamine N-oxide can still be used to turn the mixed maghemite-magnetite NPs or magnetite NPs into full maghemite NPs.

In the following sections, we will show a size series of monodisperse iron oxide nanoparticles that were synthesized upon the high decomposition of iron precursors using well-controlled reaction conditions.

2.2.1 About 6 nm magnetic nanoparticles

Figure 2.1 shows monodisperse SPIONs that were synthesized by the decomposition of iron pentacarbonyl in a solvent mixture of 1-HDE and 1-ODE in the presence of oleic acid. The ratio of 1-HDE to 1-ODE in the solvent was 5:2, leading to a boiling point of ~290 °C. This temperature controls the inorganic diameter of as-synthesized NPs which are ~6 nm in this case. Because of the use of iron pentacarbonyl, trimethylamine N-oxide was used here in order to oxidize metal iron NPs into full SPIONs (maghemite).

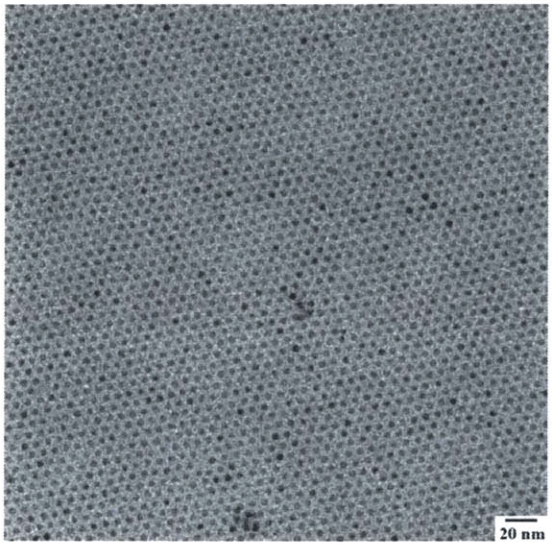

Figure 2.1 Transmission electron microscopy (TEM) images of SPIONs (maghemite) with ~6 nm inorganic diameter

2.2.2 About 3 nm magnetic nanoparticles

Figure 2.2 shows the monodisperse SPIONs with an inorganic diameter of ~3.0 nm that were synthesized by the decomposition of iron oleate in a solvent mixture of 1-TDE and 1-HDE in the presence of oleic acid. Here the ratio of 1-TDE to 1-HDE in the solvent was 4:1, resulting in a boiling point of ~270 ^{o}C that gives rise to ~3.0 nm NPs. Trimethylamine N-oxide was used in order to fully oxidize mixed maghemite-magnetite SPIONs into full maghemite SPIONs.

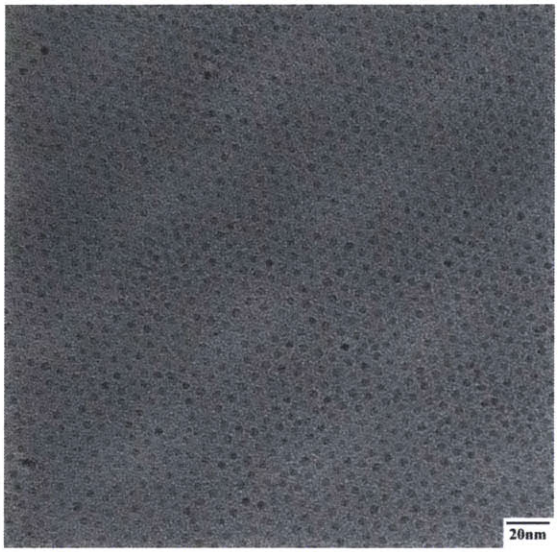

Figure 2.2 TEM images of SPIONs (maghemite) with ~3 nm inorganic diameter

2.2.3 About 2.5 nm magnetic nanoparticles

In Figure 2.3, SPIONs of ~2.5 nm inorganic diameter were shown. Although the type and concentration of iron precursor (iron oleate) used for ~2.5 nm SPIONs were the same as those of ~3 nm SPIONs, the solvent was different (a mixture of 1-HDE and 1-ODE with a ratio of 7:3) and heating rate was much slower. Similarly, trimethylamine N-oxide was employed to ensure the final formation of maghemite SPIONs.

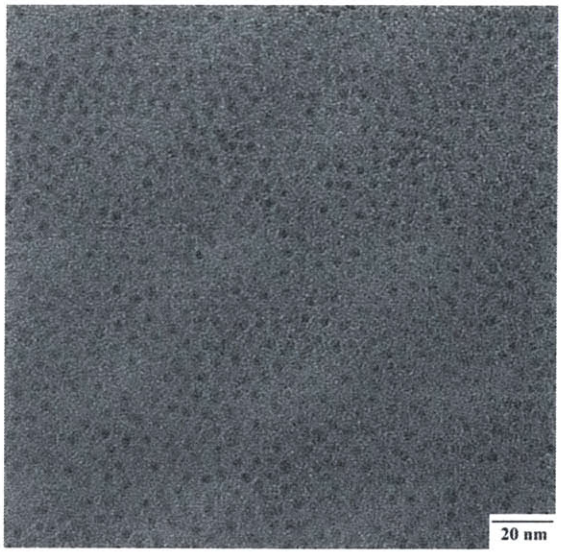

Figure 2.3 TEM images of SPIONs (maghemite) with ~2.5 nm inorganic diameter

2.2.4 Experimental details

Experimental details of Figure 2.1: To a 100 °C solvent of mixed 5.7 mL 1-octadecene and 14.3 mL 1-hexadecene, 400 μL of $Fe(CO)_5$ and 1.91 mL of oleic acid were added. The temperature was increased by 2 °C/min to 290 °C, at which the reaction was allowed to proceed for 1 hr. Upon the completion of reaction, the reaction mixture was allowed to cool down to room temperature, and 0.32 g of $(CH_3)_3NO$ oxidizing agent was added. The temperature was then increased to 130 °C (2 hrs) and 275 °C (15 min) for the oxidation reaction. After the mixture was cooled to room temperature, ethanol was added and the resulting solution was centrifuged. Finally, the supernatant was discarded and the SPION pellets were dispersed and stored in hexane.

Experimental details of Figure 2.2: 0.900 g of $Fe(oleate)_3$ was added to 190 µL of oleic acid in a mixture of 4.0 mL 1-tetradecene and 1.0 mL 1-hexadecene at room temperature. This reaction mixture was degassed at 100 °C for 30 mins. The temperature was rapidly heated to a final temperature of 270 °C and was kept constant for 1 hr. Upon the completion of reaction, the reaction mixture was allowed to cool down to room temperature, and 0.113 g of $(CH_3)_3NO$ oxidizing agent was added. The temperature was then increased to 130 °C (1 hr). After the mixture was cooled to room temperature, acetone was added and the resulting solution was centrifuged. Finally, the supernatant was discarded and the SPION pellets were dispersed and stored in hexane.

Experimental details of Figure 2.3: 0.910 g of $Fe(oleate)_3$ was added to 190 µL of oleic acid in a mixture of 3.5 mL 1-hexadecene and 1.5 mL 1-octadecene at room temperature, followed by a 30 mins degassing at 100 °C. The temperature was raised at a rate of 7 °C/min to a final temperature of 300 °C and was kept constant for 1 hr. Upon the completion of reaction, the reaction mixture was allowed to cool down to room temperature, and 0.126 g of $(CH_3)_3NO$ oxidizing agent was added. The temperature was then increased to 130 °C (1 hr). Afterwards, the mixture was cooled to room temperature, acetone was added and the resulting solution was centrifuged. Finally, the supernatant was discarded and the SPION pellets were dispersed and stored in hexane.

2.3 Synthesis of 7-15 nm magnetic nanoparticles

2.3.1 About 7 nm and 8 nm magnetic nanoparticles

Compared to the synthesis of small-sized SPIONs, medium-sized SPIONs were generally produced at higher temperatures, longer reaction times, or a smaller amount of native organic ligands. Figure 2.4a shows ~7 nm monodisperse SPIONs that were synthesized by the decomposition of iron pentacarbonyl in a di-octyl ether solvent with native oleic acid organic ligands. A smaller amount of oleic acid was used compared to the synthesis of small-sized SPIONs. As the SPIONs were larger in this case, the oxidation reaction time with trimethylamine N-oxide was increased and the oxidation reaction temperature was increased in order to ensure the full oxidation of metal iron NPs into maghemite SPIONs. Figure 2.4b shows ~8 nm monodisperse SPIONs which were synthesized using conditions similar to those of ~7 nm monodisperse SPIONs (see experimental details). SPIONs in Figure 2.4b were already ligand-exchanged and hydrophilic. More details will be discussed in Chapter 3 and 4.

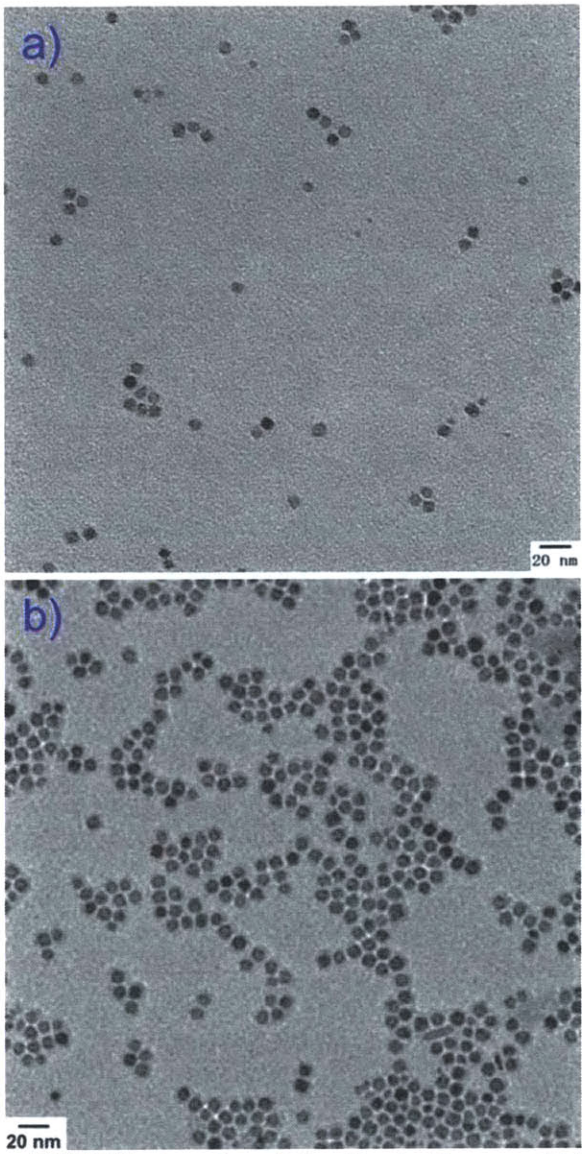

Figure 2.4 TEM images of SPIONs (maghemite) with a) ~7 nm and b) ~8 nm inorganic diameters; b) is adapted with permission from (Wei H.; et al. "Compact Zwitterion-Coated Iron Oxide Nanoparticles for Biological Applications" Nano Letters 2012, 12, 22). Copyright (2011) American Chemical Society.

2.3.2 About 11 nm and 12 nm magnetic nanoparticles

Figure 2.5a and b shows monodisperse magnetite SPIONs with inorganic diameters of ~11 nm and ~12 nm, respectively. Unlike the synthesis of 7-8 nm maghemite SPIONs, iron oleate was used as the iron precursor and the heating rate was much faster for the synthesis of 11-12 nm mixed maghemite-magnetite SPIONs (see experimental details). No oxidizing agent was used here, and thus the SPIONs are mixed maghemite-magnetite NPs.

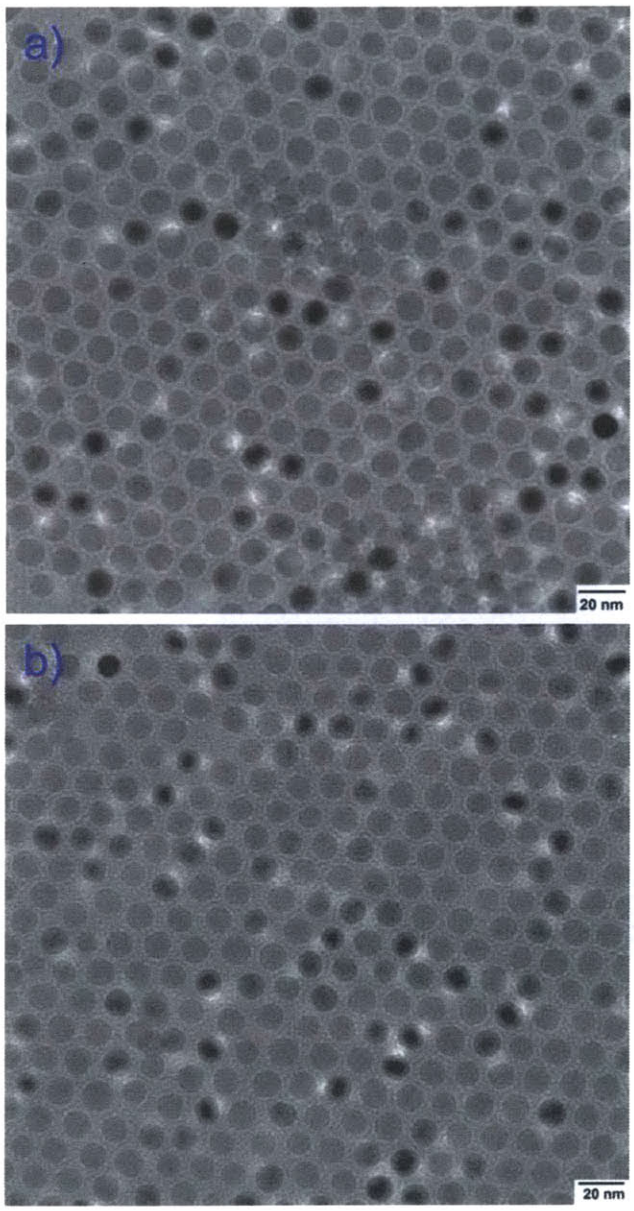

Figure 2.5 TEM images of SPIONs with a) ~11 nm and b) ~12 nm inorganic diameters

2.3.3 About 15 nm magnetic nanoparticles

Even larger SPIONs can also be produced using the same iron precursors and native organic ligands under well-controlled reaction conditions. When the reaction temperature was increased to ~320 ^{o}C, monodisperse mixed maghemite-magnetite SPIONs of a ~15 nm inorganic diameter can be synthesized, as shown in Figure 2.6. Interestingly, these ~15 nm SPIONs can self-assemble and then form a super lattice structure, as shown in Figure 2.7.

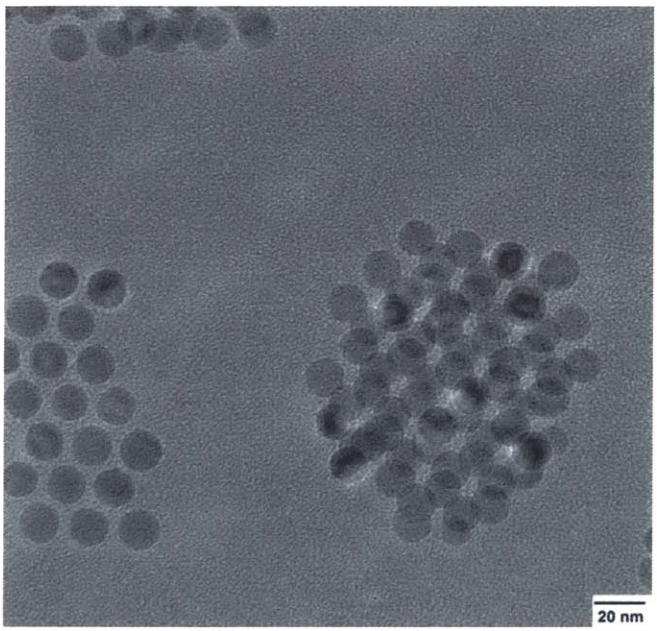

Figure 2.6 TEM images of SPIONs with ~15 nm inorganic diameters

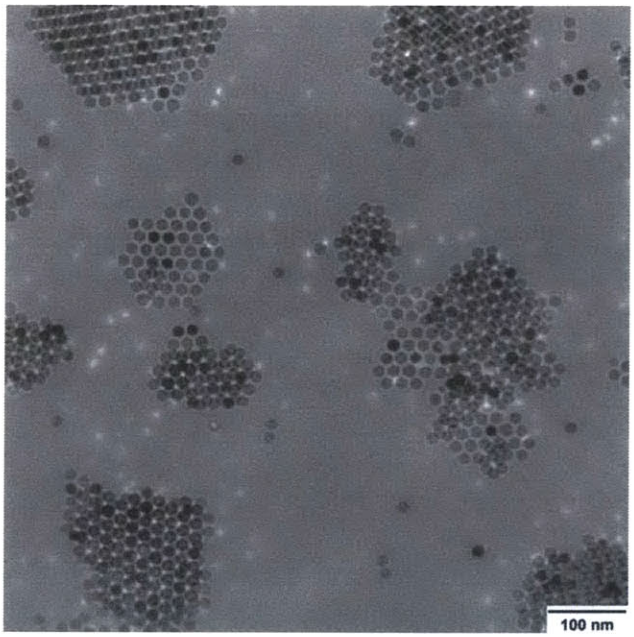

Figure 2.7 TEM images of SPIONs with ~15 nm inorganic diameters forming super lattice

2.3.4 Experimental details

Experimental details of Figure 2.4a: To a 100 °C solvent of 20 mL di-octyl ether, 400 µL of $Fe(CO)_5$ and 0.70 mL of oleic acid were added. The temperature was increased by 2 °C/min to 290 °C, at which the reaction was allowed to proceed for 1 hr. Upon the completion of reaction, the reaction mixture was allowed to cool down to room temperature, and 0.32 g of $(CH_3)_3NO$ oxidizing agent was added. The temperature was then increased to 130 °C (2 hrs) and 275 °C (15 min) for the oxidation reaction. After the mixture was cooled to room temperature, ethanol was added and the resulting solution was centrifuged. Finally, the supernatant was discarded and the SPION pellets were dispersed and stored in hexane.

Experimental details of Figure 2.4b: To a 100 °C solvent of 20 mL di-octyl ether, 400 μL of $Fe(CO)_5$ and 0.75 mL of oleic acid were added. The temperature was increased by 2 °C/min to 290 °C, at which the reaction was allowed to proceed for 1 hr. Upon the completion of the reaction, the reaction mixture was allowed to cool down to room temperature, and 0.32 g of $(CH_3)_3NO$ oxidizing agent was added. The temperature was then increased to 130 °C (2 hrs) and 275 °C (15 min) for the oxidation reaction. After the mixture was cooled to room temperature, ethanol was added and the resulting solution was centrifuged. Finally, the supernatant was discarded and the SPION pellets were dispersed and stored in hexane.

Experimental details of Figure 2.5a: 0.894 g of $Fe(oleate)_3$ was added to 200 μL of oleic acid in 5.0 mL 1-octadecene at room temperature, followed by a 30 mins degassing at 100 °C. The temperature was rapidly heated to a final temperature of 290 °C and was kept constant for 1 hr. Upon the completion of reaction, the reaction mixture was allowed to cool down to room temperature, and acetone was added and the resulting solution was centrifuged. Finally, the supernatant was discarded and the SPION pellets were dispersed and stored in hexane.

Experimental details of Figure 2.5b: 0.903 g of $Fe(oleate)_3$ was added to 200 μL of oleic acid in a mixture of 1.7 mL 1-octadecene and 3.3 mL 1-hexadecene at room temperature, followed by a 30 mins degassing at 100 °C. The temperature was rapidly heated to a final temperature of 300 °C and was kept constant for 1 hr. Upon the completion of reaction, the reaction mixture was allowed to cool down to room temperature, and acetone was added and the resulting solution was centrifuged. Finally, the supernatant was discarded and the SPION pellets were dispersed and stored in hexane.

Experimental details of Figure 2.6: 0.920 g of $Fe(oleate)_3$ was added to 200 μL of oleic acid in 5 mL 1-octadecene at room temperature, followed by a 60 mins degassing at 100 °C. The temperature was rapidly heated to a final temperature of 320 °C and was kept constant for 1 hr. Upon the completion of reaction, the reaction mixture was allowed to cool down to room temperature, and acetone was added and the resulting solution was centrifuged. Finally, the supernatant was discarded and the SPION pellets were dispersed and stored in hexane.

2.4 Synthesis of 16-35 nm magnetic nanoparticles

In order to synthesize 16-35 nm SPIONs, solvents with boiling points higher than 320 °C can sometimes be used. Under these reaction temperatures, 1-tetradecene, 1-hexadecene, and 1-octadecene are no longer satisfactory; and thus 1-eicosene, 1-dococene, and 1-tetracosane are introduced. Moreover, if reaction temperatures are higher than the boiling point of oleic acid, then oleic acid will be evaporated and no longer stay in the liquid reaction mixture. In such conditions, native organic ligands with higher boiling points such as stearic acid and nonadecanoic acid can be introduced.

2.4.1 About 16 nm magnetic nanoparticles

Figure 2.8 shows monodisperse maghemite SPIONs with an inorganic diameter of ~16 nm, which were produced from the iron pentacarbonyl precursor. Compared to previous synthetic conditions, the main difference here is a prolonged reaction time and the use of a stronger

oxidizing agent. 2 hours (hrs) of reaction time was used instead of the commonly-used 1 hr of reaction time. The oxidizing agent was changed from commonly used trimethylamine N-oxide to 4-phenylpyridine N-oxide, because larger metal iron NPs are generally more difficult to be fully oxidized into maghemite SPIONs.

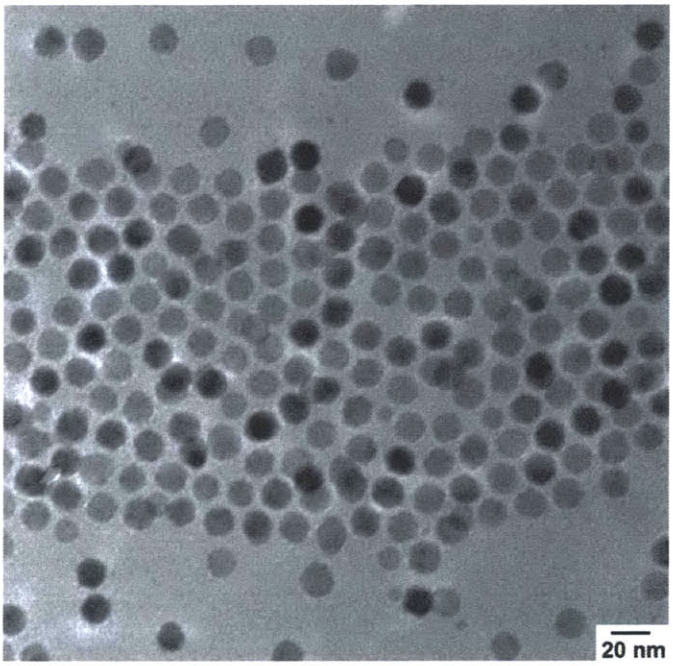

Figure 2.8 TEM images of SPIONs (maghemite) with ~16 nm inorganic diameters

2.4.2 About 18 nm magnetic nanoparticles

Figure 2.9 demonstrates monodisperse SPIONs of a ~18 nm inorganic diameter that were produced from the decomposition of iron oleate precursors in a solvent of 1-docosene. The reaction temperature used here was 360 ^{o}C, which is much higher than that in previous synthetic routes. Oleic acid as a native organic ligand was still usable under this temperature. No oxidizing agent was added and thus the SPIONs are mixed maghemite-magnetite particles.

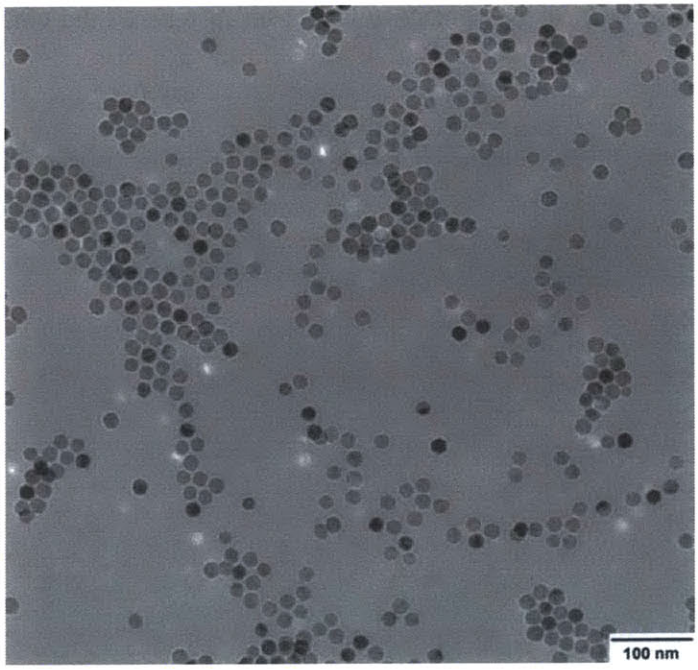

Figure 2.9 TEM images of SPIONs with ~18 nm inorganic diameters

2.4.3 About 20 nm magnetic nanoparticles

If the reaction temperature is increased further, then larger SPIONs can be obtained. As shown in Figure 2.10, monodisperse SPIONs of a ~20 nm inorganic diameter was produced from the decomposition of iron oleate in a solvent of 1-docosene at 370 °C. Similarly, no oxidizing agent was added and thus mixed maghemite-magnetite SPIONs were formed.

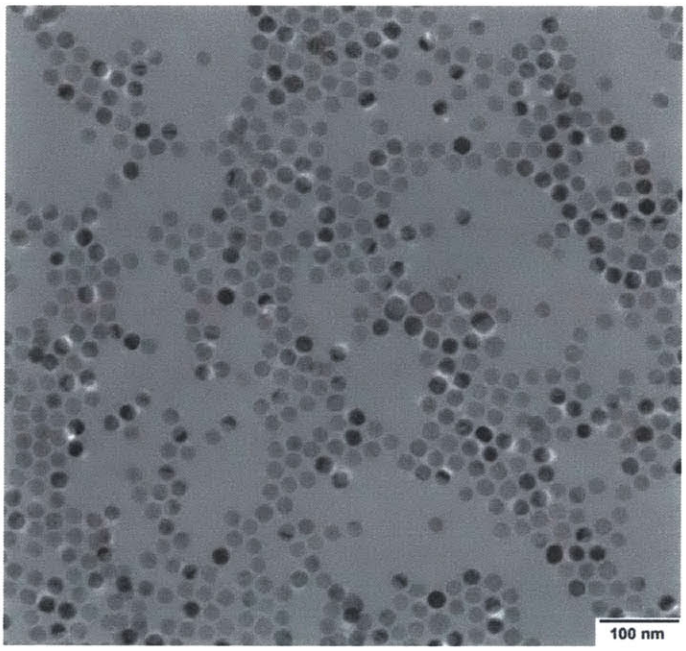

Figure 2.10 TEM images of SPIONs with a ~20 nm inorganic diameter

2.4.4 Polydisperse magnetic nanoparticles

Further increase of reaction temperatures did not give rise to monodisperse SPIONs so far. For example, the reaction of iron oleate in a solvent of tetracosane with stearic acid (here the stearic acid was used because the reaction temperature was higher than the boiling point of oleic acid) was carried at 380 °C. No oxidizing agent was used. The resulted mixed maghemite-magnetite SPIONs were polydisperse (not uniformly sized), as shown in Figure 2.11a: within one TEM image, smallest SPION has an inorganic diameter of ~10 nm while largest SPION has an inorganic diameter of ~30 nm. Figure 2.11b shows SPIONs that were synthesized by the reaction of iron oleate in a tetracosane solvent with stearic acid at 390 °C. Similar to Figure 2.11a, the SPIONs in Figure 2.11b were polydisperse too.

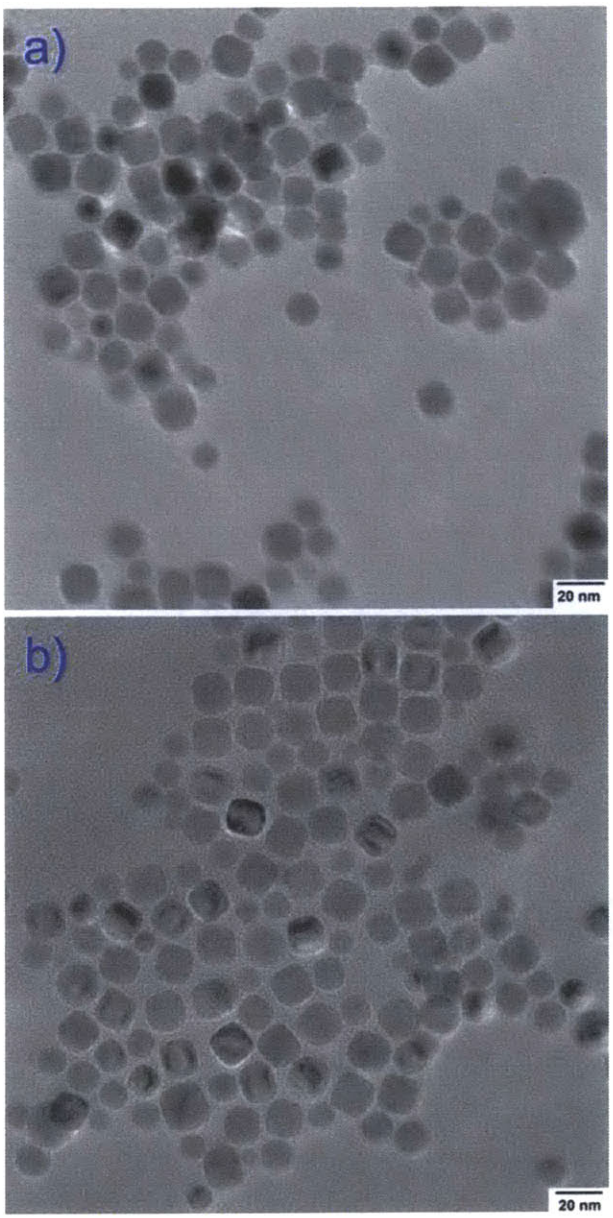

Figure 2.11 TEM images of polydisperse SPIONs synthesized at a) 380 °C and b) 390 °C

Monodisperse and high-quality SPIONs with an inorganic diameter larger than 25 nm are generally difficult to be synthesized using the high-temperature decomposition method. This observation is in agreement with other published reports.

2.4.5 About 35 nm magnetic nanoparticles

As a result, instead of further increasing reaction temperature, other reaction parameters such as native organic ligand concentration were tuned. We developed a new technique of high-temperature decomposition synthesis, in which the reaction temperature was kept at 360 °C and four times more oleic acid than usual was added. This new method has enabled the synthesis of >25 nm monodisperse SPIONs. As shown in Figure 2.12a and b, these monodisperse mixed maghemite-magnetite SPIONs have an inorganic diameter of ~35 nm, which is close to the upper size limit for superparamagnetic iron oxide NPs (larger iron oxide NPs are not magnetically single-domain and become ferrimagnetic).

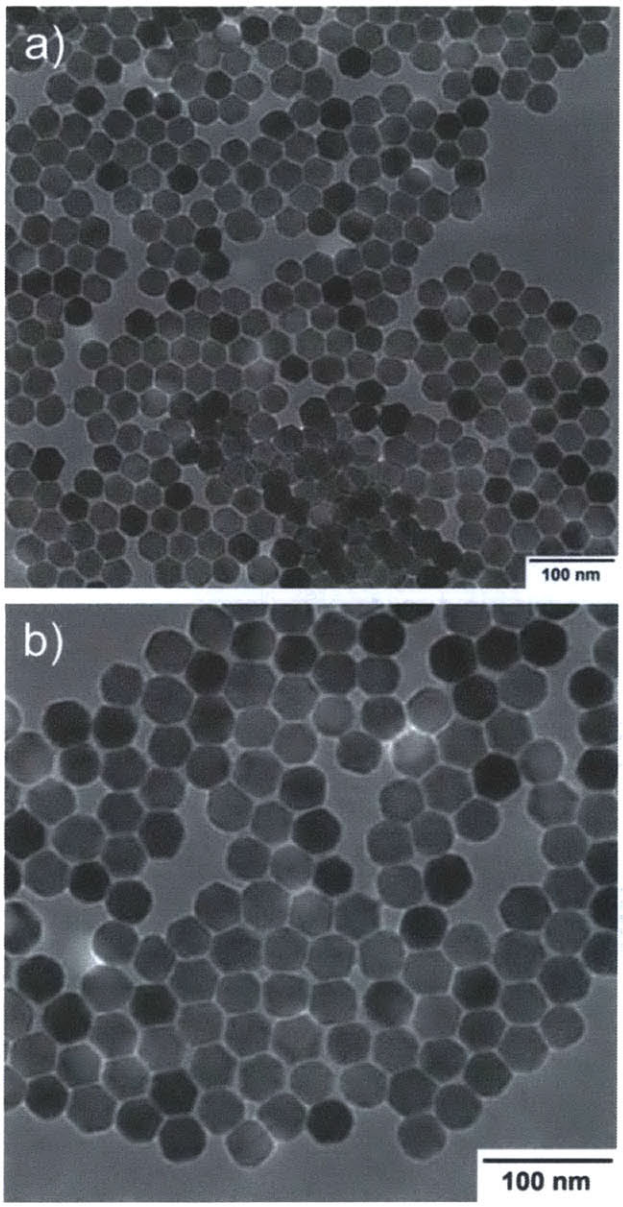

Figure 2.12 TEM images of a) and b) SPIONs with a ~35 nm inorganic diameter under different magnifications

2.4.6 Experimental details

Experimental details of Figure 2.8: To a 100 °C solvent of 20 mL 1-octadecene, 400 μL of $Fe(CO)_5$ and 1.91 mL of oleic acid were added. The temperature was increased by 2.3 °C/min up to 320 °C, at which the reaction was allowed to proceed for 2 hrs. Upon the completion of reaction, the reaction mixture was allowed to cool down to room temperature, and 0.729 g of 4-phenylpyridine N-oxide oxidizing agent was added. The temperature was then increased to 130 °C (2 hrs) for the oxidation reaction. After the mixture was cooled to room temperature, ethanol was added and the resulting solution was centrifuged. Finally, the supernatant was discarded and the SPION pellets were dispersed and stored in hexane.

Experimental details of Figure 2.9: 0.918 g of $Fe(oleate)_3$ was added to 200 μL of oleic acid in 5 mL 1-docosene at room temperature, followed by a 60 mins degassing at 100 °C. The temperature was rapidly heated to a final temperature of 360 °C and was kept constant for 1 hr. Upon the completion of reaction, the reaction mixture was allowed to cool down to room temperature, and chloroform and acetone were added and the resulting solution was centrifuged. Finally, the supernatant as well as solid-phase 1-docosene were discarded and the SPION pellets were dispersed and stored in hexane.

Experimental details of Figure 2.10: 0.935 g of $Fe(oleate)_3$ was added to 400 μL of oleic acid in 5 mL 1-docosene at room temperature, followed by a 60 mins degassing at 100 °C. The temperature was rapidly heated to a final temperature of 370 °C and was kept constant for 1 hr. Upon the completion of reaction, the reaction mixture was allowed to cool down to room temperature, and chloroform and acetone were added and the resulting solution was centrifuged.

Finally, the supernatant as well as solid-phase 1-docosene were discarded and the SPION pellets were dispersed and stored in hexane.

Experimental details of Figure 2.11a: 0.900 g of $Fe(oleate)_3$ was added to 0.180 g of stearic acid in 5 mL tetracosane, followed by a 60 mins degassing at 100 °C. The temperature was rapidly heated to a final temperature of 380 °C and was kept constant for 1 hr. Upon the completion of reaction, the reaction mixture was allowed to cool down to room temperature, and chloroform and acetone were added and the resulting solution was centrifuged. Finally, the supernatant was discarded and the SPION pellets were dispersed and stored in hexane.

Experimental details of Figure 2.11b: 0.912 g of $Fe(oleate)_3$ was added to 0.180 g of stearic acid in 5 mL tetracosane, followed by a 60 mins degassing at 100 °C. The temperature was rapidly heated to a final temperature of 390 °C and was kept constant for 1 hr. Upon the completion of reaction, the reaction mixture was allowed to cool down to room temperature, and chloroform and acetone were added and the resulting solution was centrifuged. Finally, the supernatant was discarded and the SPION pellets were dispersed and stored in hexane.

Experimental details of Figure 2.12a&b: 0.935 g of $Fe(oleate)_3$ was added to 800 μL of oleic acid in 5 mL 1-docosene at room temperature, followed by a 60 mins degassing at 100 °C. The temperature was rapidly heated to a final temperature of 360 °C and was kept constant for 1 hr. Upon the completion of reaction, the reaction mixture was allowed to cool down to room temperature, and chloroform and acetone were added and the resulting solution was centrifuged. Finally, the supernatant was discarded and the SPION pellets were dispersed and stored in hexane.

2.5 Summary of synthetic routes

The synthetic routes of different sized SPIONs are summarized in the following Figure 2.13 and Table 2.1. Iron precursors switched between iron pentacarbonyl (6, 7, 8, and 16 nm SPIONs) and iron oleate (other SPIONs). This is because iron pentacarbonyl was used in early synthesis (6, 7, 8, and 16 nm SPIONs); but the precursor was changed to iron oleate, as it is less toxic than iron pentacarbonyl and can be more easily controlled in producing SPIONs.

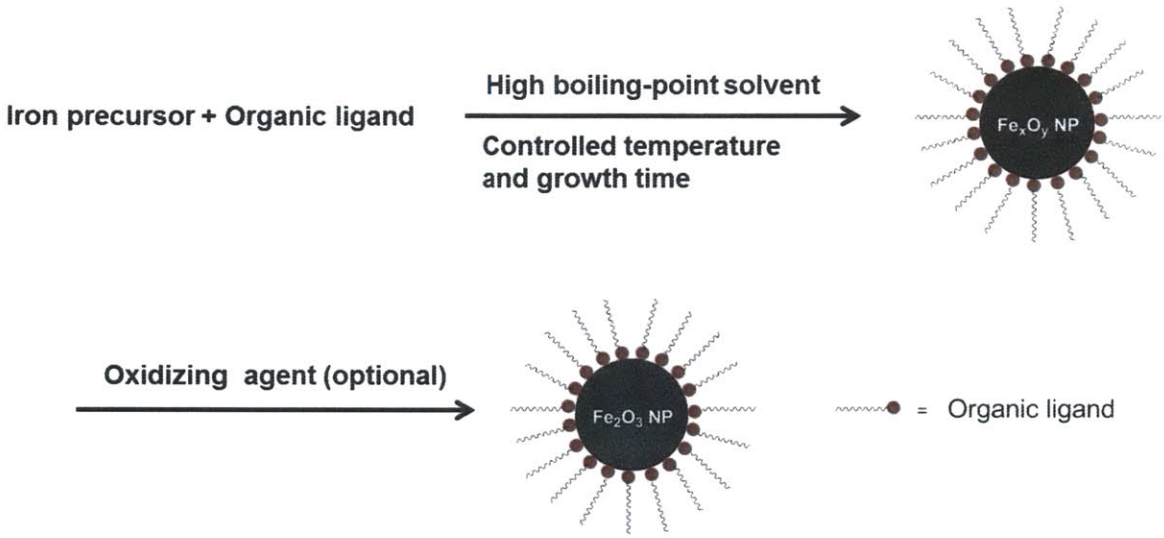

Figure 2.13 A synthetic scheme of different sized SPIONs using different reaction conditions. Iron precursor: iron oleate, iron pentacarbonyl, etc.; organic ligand: oleic acid, stearic acid, nonadecanoic acid, etc.; solvent: 1-tetradecene, 1-hexadecene, 1-octadecene, etc.; oxidizing agent: trimethylamine N-oxide, 4-phenylpyridine N-oxide, etc.

Inorganic diameter of SPION (nm)	Iron precursor	Solvent (mixture)	Molar ratio of native organic ligand : iron precursor	Reaction temperature (°C) / reaction time (hrs)	Heating rate (°C/min)
2.5	Iron oleate	1-hexadecene 1-octadecene	0.6:1	300 / 1	7
3	Iron oleate	1-tetradecene 1-hexadecene	0.6:1	270 / 1	>10
6	Iron pentacarbonyl	1-hexadecene 1-octadecene	2:1	290 / 1	2
7	Iron pentacarbonyl	di-octyl ether	0.75:1	290 / 1	2
8	Iron pentacarbonyl	di-octyl ether	0.8:1	290 / 1	2
11	Iron oleate	1-octadecene	0.6:1	290 / 1	>10
12	Iron oleate	1-hexadecene 1-octadecene	0.6:1	300 / 1	>10
15	Iron oleate	1-octadecene	0.6:1	320 / 1	>10
16	Iron pentacarbonyl	1-octadecene	2:1	320 / 2	2.3
18	Iron oleate	1-docosene	0.6:1	360 / 1	>10
20	Iron oleate	1-docosene	1.2:1	370 / 1	>10
35	Iron oleate	1-docosene	2.4:1	360 / 1	>10

Table 2.1 Different sized SPIONs synthesized at different reaction conditions

3. Chapter 3: Synthesis of novel ligand coatings for magnetic nanoparticles

3.1 Introduction to nanoparticles' ligand exchange

3.1.1 Necessity of ligand exchange

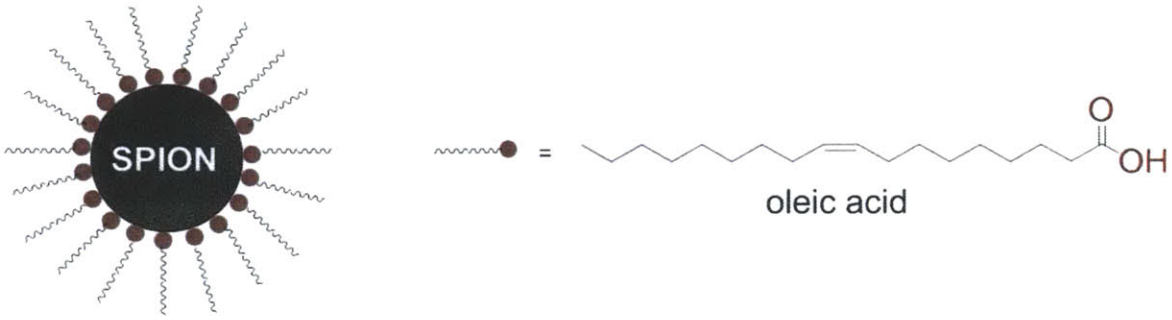

Figure 3.1 Hydrophobic SPIONs that are coated by native oleic acid ligands

Monodisperse (a. k. a. uniformly sized) superparamagnetic iron oxide nanoparticles (SPIONs) are usually synthesized by the high-temperature decomposition of iron precursors in organic solvents with native organic ligands. Consequently, the native organic ligands (such as alkane chains and olefin chains) coat on the surfaces of SPIONs during synthesis and these native organic ligands make the as-synthesized SPIONs hydrophobic, as shown in Figure 3.1. The as-synthesized SPIONs are therefore not able to be dispersed (a. k. a. insoluble) in aqueous systems of biomedical interests.[38] As a result, the surface modification of the as-synthesized SPIONs is essential to endow them with biocompatibility, in which there are two representative methods: encapsulation and ligand exchange. Encapsulation is to coat SPIONs with more hydrophilic shells; for example, gold[39] and silica[40] have been coated on SPIONs. Ligand exchange is to exchange the native organic ligands of SPIONs with new water-soluble ligands. Compared to

encapsulation, ligand exchange is generally better due to two reasons: versatile derivatization pathways and small hydrodynamic diameters (overall sizes).

3.1.2 Challenges of ligand exchange

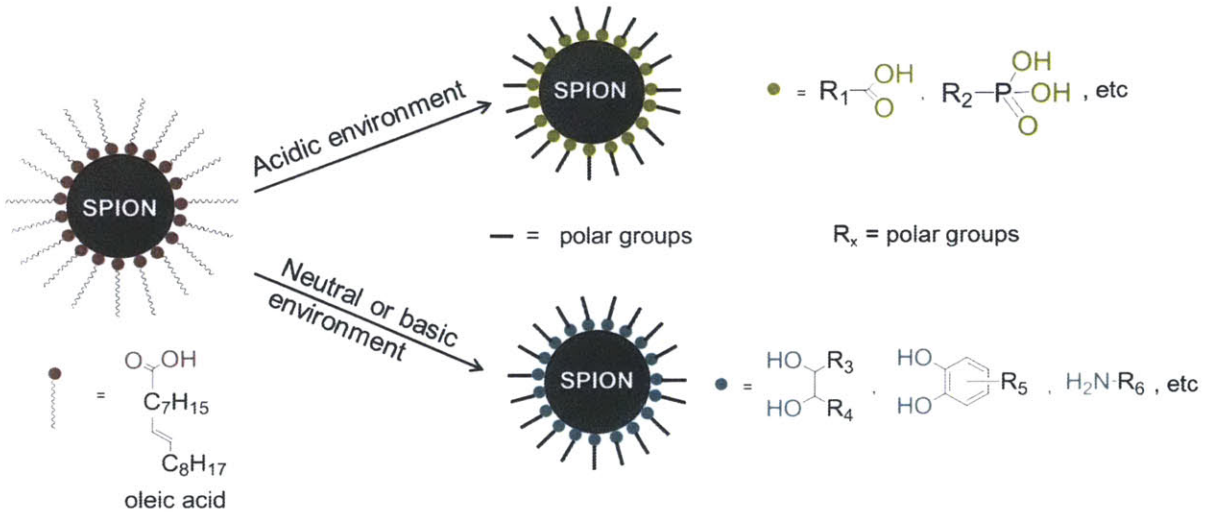

Figure 3.2 Ligand exchange schemes for SPIONs

The challenges of ligand exchange are mainly set by the design of ligands with desirable properties and the followed organic synthesis of as-designed ligands.[41] In the last decade, extensive research has been done in terms of the design and synthesis of ligands for the surface modification of SPIONs. A series of ligands such as alkanephosphonic acid, carboxylalkyltrialkylammonium salt, 2,3-dimercaptosuccinic acid, dextran, and dopamine were produced and used for ligand exchange with SPIONs.[10, 42, 43, 44, 45] Figure 3.2 shows the ligand exchange schemes for SPIONs, which can be divided into two types. The first type is the ligand exchange in acidic environments, and ligands with carboxylic groups and ligands phosphate

groups are commonly used in the first type. The second type is the ligand exchange in neutral or basic environments, and ligands with vicinal diol groups and amino groups are commonly used in the second type.

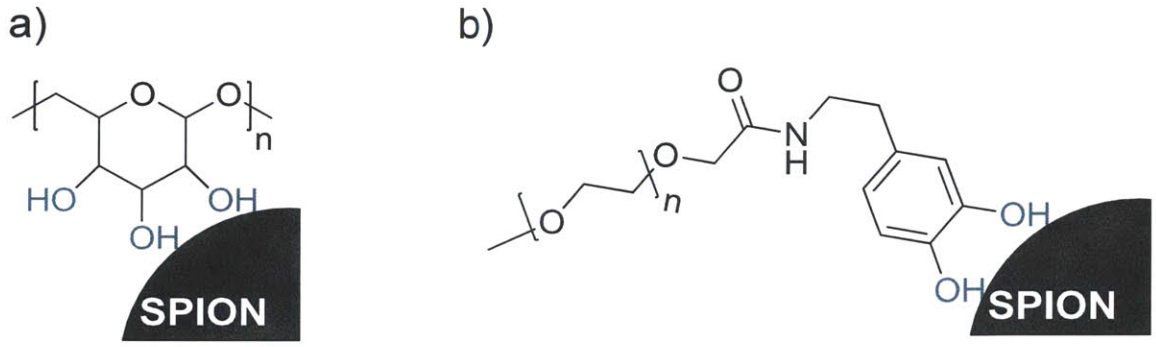

Figure 3.3 a) dextran coated SPIONs and b) PEGylated-dopamine coated SPIONs

Vicinal diol groups are strong binding groups toward SPIONs due to their strong interaction with the surface of iron oxide.[46] Dextran and catechol derivatives both contain vicinal diol groups and thus they have found their use as promising ligand coatings for SPIONs. For example, as shown in Figure 3.3a, dextran derivatives coated SPIONs can be well dispersed in aqueous buffers and they are sufficiently non-toxic with extended blood half-lives.[47] More recently, as shown in Figure 3.3b, it has been discovered that polyethylene glycol (PEG) coupled dopamine (PEGylated-dopamine) could serve as ligand coatings for SPIONs, and the resulting PEGylated-dopamine coated SPIONs are generally stable in aqueous buffers at room temperature.[48] In addition to the strong binding affinity between dopamine and iron oxide surface, the long PEG chains are also well known for ensuring a biologically non-fouling property.[49]

Nevertheless, dextran and PEGylated-dopamine derivatives are both large organic molecules and they usually cause a large increase in the overall size (hydrodynamic diameter) of SPIONs.

Although the inorganic diameters of SPIONs are usually on the order of 10 nm, the hydrodynamic diameters (HDs) of dextran and PEGylated-dopamine derivatives coated SPIONs can be ~30-200 nm. Such large HDs may restrict SPIONs' access to confined biological spaces of interests and large HDs can also prevent the fast clearance of SPIONs through the kidneys, leading to a longer exposure of SPIONs to living animals. Moreover, it has been reported that PEG-based ligands coated SPIONs may aggregate in high-salinity buffers.[50] Consequently, in order to use SPIONs in various biomedical applications, there remains a critical demand for newly biocompatible yet small ligands. The new ligands should have the same desired properties as dextran and PEGylated-dopamine derivatives such as high water solubility, strong binding affinity to SPIONs, biological non-fouling property, as well as long-term stability. More importantly, the new ligands should have small size that can overcome the present difficulties of dextran and PEGylated-dopamine derivatives.

3.2 New ligand - zwitterionic dopamine sulfonate

3.2.1 Design of zwitterionic dopamine sulfonate

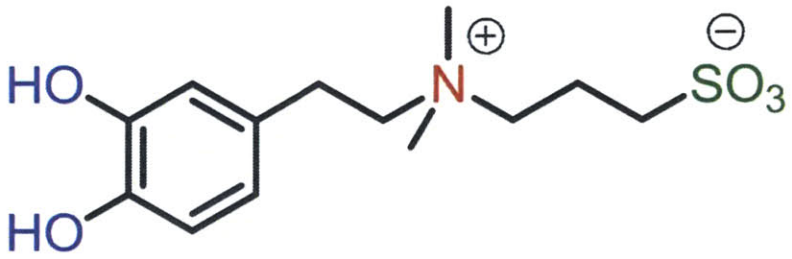

Figure 3.4 Chemical structure of zwitterionic dopamine sulfonate ligand

When designing this new ligand for SPIONs, we have the following considerations in mind: (1) it has strong coordination to the iron oxide surface of SPIONs, (2) it has a relatively small molecular weight, (3) it has highly hydrophilic groups for good water-solubility, and (4) it is biocompatible and has minimized non-specific interactions with proteins. Therefore, as shown in Figure 3.4, a new ligand - zwitterionic dopamine sulfonate (ZDS) - was designed. ZDS has the following advantages: first, the 3,4-dihydroxyl groups (vicinal diol groups, marked by blue color) on the dopamine moiety convey strong coordination to the surface iron oxide of SPIONs; second, the sulfonate group (marked by green color) provides a high water solubility to ZDS; third, the quaternary amine group (marked by red color) is added to carry a positive charge that neutralizes with a negative charge from the sulfonate group, making the ZDS zwitterionic and stable within physiological pH range.

3.2.2 Synthesis of zwitterionic dopamine sulfonate

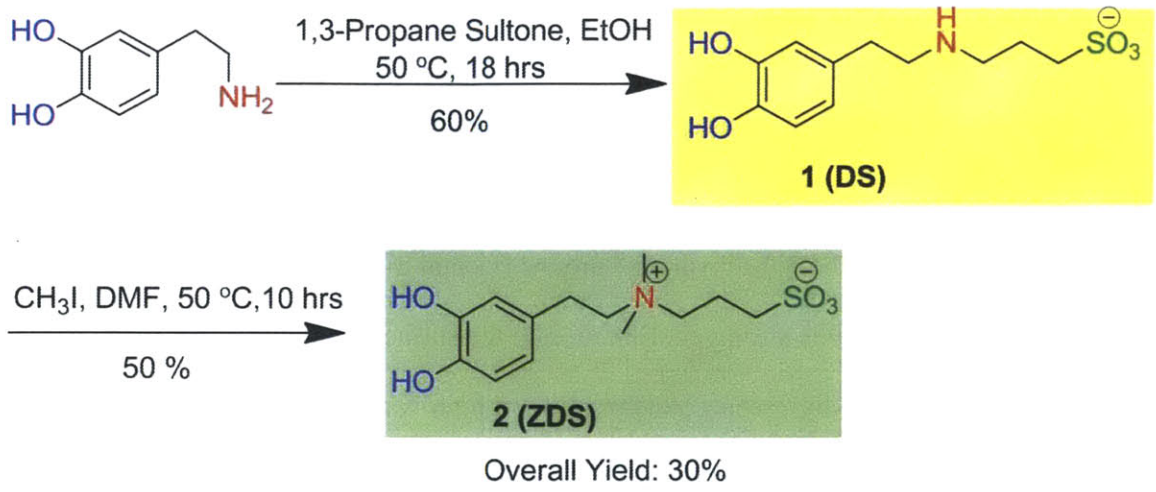

Figure 3.5 Synthetic route of dopamine sulfonate (DS) and zwitterionic dopamine sulfonate (ZDS) ligands. Adapted with permission from (Wei H.; et al. "Compact Zwitterion-Coated Iron Oxide Nanoparticles for Biological Applications" Nano Letters 2012, 12, 22). Copyright (2011) American Chemical Society.

Figure 3.5 shows the synthesis of dopamine sulfonate (DS) and zwitterionic dopamine sulfonate (ZDS) ligands. The first step is the sulfonation of primary amine group of dopamine, which was achieved by a ring opening reaction with 1,3-propane sultone in a solvent of ethanol (EtOH) at 50 °C for 18 hrs. After purification, this first step yielded a white solid - DS. The second step is the methylation of the secondary amine group of DS using iodomethane in a solvent of dimethylformamide (DMF) at 50 °C for 10 hrs. After purification, this second step yielded the ZDS.

3.2.3 Experimental details

Synthesis of Dopamine Sulfonate. 1.1376 g dopamine hydrochloride was added into a solvent of 150 mL ethanol, followed by evacuation and back-filling with nitrogen gas in succession. Next, 0.416 mL of 28% ammonium hydroxide aqueous solution and 0.799 g of 1,3-propanesultone were slowly added in succession. The reaction was allowed to proceed at 50 °C for 18 hrs, leading to the formation of white precipitate. After cooling down to room temperature, the reaction mixture was filtered; the solution was then discarded while the white precipitate was then washed by ethanol (three times). The resulting white solid was dried in vacuo and was found to be pure (by NMR) dopamine sulfonate (DS).

Synthesis of Zwitterionic Dopamine Sulfonate. 0.3286 g dopamine sulfonate from previous synthesis and 0.2544 g anhydrous sodium carbonate were added into a solvent of 150 mL dimethylformamide (DMF), followed by evacuation and back-filling with nitrogen gas in succession. Next, 2.2 mL iodomethane was added and the reaction was allowed to proceed at 50 °C for 10 hrs until the color of reaction mixture became yellow. Upon the removal of DMF by a rotary evaporator at 40 °C, an oily crude product was obtained. After being precipitated by DMF/ethyl acetate (1:10 v/v) and refluxed with DMF/acetone (1:10 v/v), the reaction mixture was then filtered. The reflux and filter procedures were repeated two more times, resulting in a white solid, which was then characterized by NMR. The NMR data showed this white solid to be pure zwitterionic dopamine sulfonate (ZDS).

3.2.4 ^{1}H NMR and ^{13}C NMR of dopamine sulfonate

The ^{1}H NMR of DS ligand at 400 MHz in a D_2O solvent was shown in Figure 3.6a with chemical shifts δ (ppm) at 2.08 (multiplet, 2H), 2.88-2.90 (multiplet, 2H), 2.94-2.99 (multiplet, 2H), 3.14-3.17 (multiplet, 2H), 3.26 (multiplet, 2H), 6.71-6.74 (multiplet, 1H), 6.82-6.88 (multiplet, 2H). All peaks were assigned to the corresponding hydrogen atoms in Figure 3.6a. The $\delta = 4.80$ peak is from the D_2O solvent.

Next, the ^{13}C NMR of DS ligand at 400 MHz in a D_2O solvent was shown in Figure 3.6b with chemical shifts δ (ppm) at 21.11, 30.88, 46.11, 47.77, 48.57, 116.44, 121.06, 128.91, 143.01, 144.19. All peaks were assigned to the corresponding carbon atoms in Figure 3.6b.

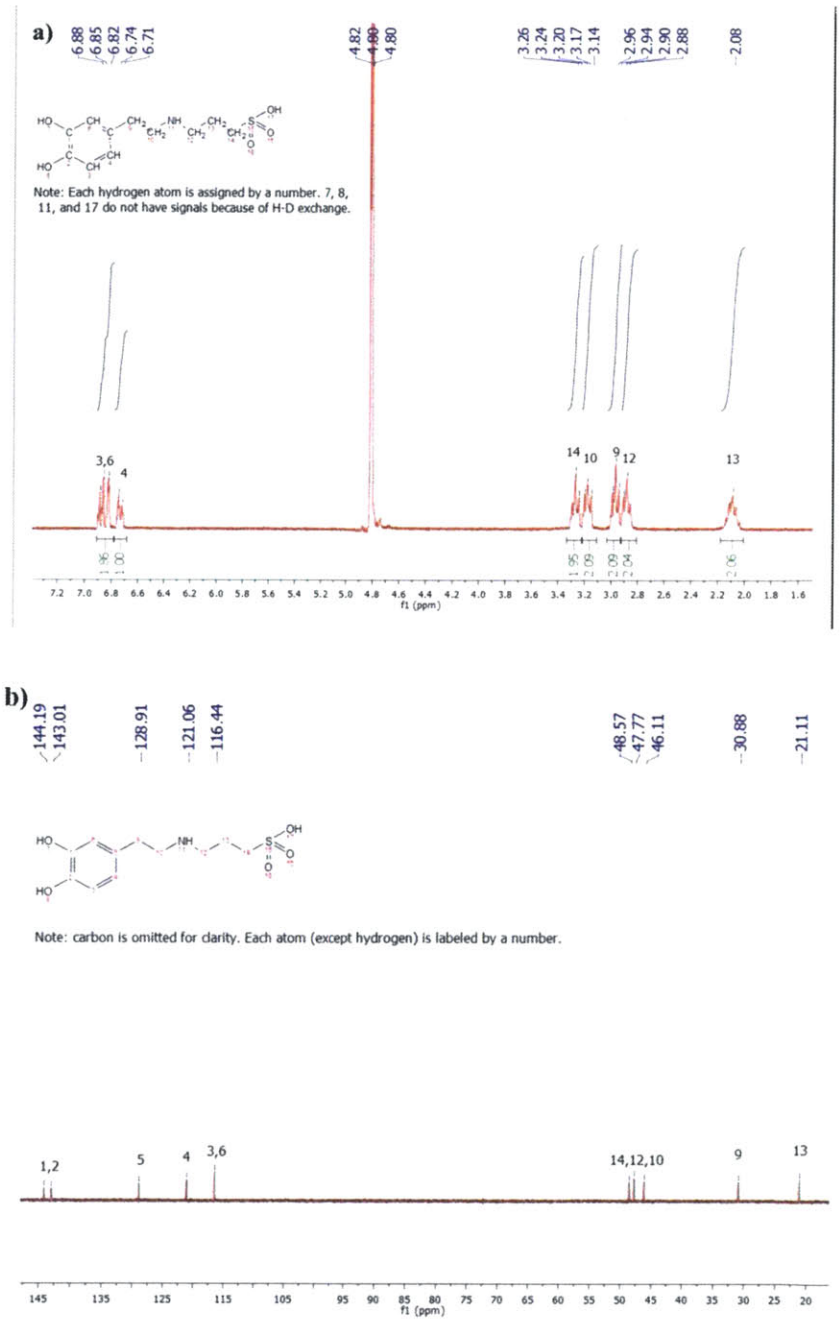

Figure 3.6 a) ^{1}H NMR and b) ^{13}C NMR of DS ligand. Reprinted with permission from (Wei H.; et al. "Compact Zwitterion-Coated Iron Oxide Nanoparticles for Biological Applications" Nano Letters 2012, 12, 22). Copyright (2011) American Chemical Society.

3.2.5 ^{1}H NMR and ^{13}C NMR of zwitterionic dopamine sulfonate

The ^{1}H NMR of ZDS ligand at 400 MHz in a D_2O solvent was shown in Figure 3.7a with chemical shifts δ (ppm) at 2.21 (multiplet, 2H), 2.92-2.95 (multiplet, 4H), 3.13 (singlet, 6H), 3.47-3.51 (multiplet, 4H), 6.74-6.76 (multiplet, 1H), 6.83-6.88 (multiplet, 2H).. All peaks were assigned to the corresponding hydrogen atoms in Figure 3.7a. The δ = 4.80 peak is again from the D_2O solvent. The presence of a singlet peak at 3.13 (six hydrogen atoms) indicates the successful methylation of DS ligand by adding two methyl groups.

Next, the ^{13}C NMR of ZDS ligand at 400 MHz in a D_2O solvent was shown in Figure 3.7b with chemical shifts δ (ppm) at 18.12, 27.66, 47.10, 50.72, 62.02, 64.62, 116.49, 121.21, 128.23, 143.03, 144.18. All peaks were assigned to the corresponding carbon atoms in Figure 3.7b. The presence of a peak at 47.10 confirms the successful methylation of DS ligand.

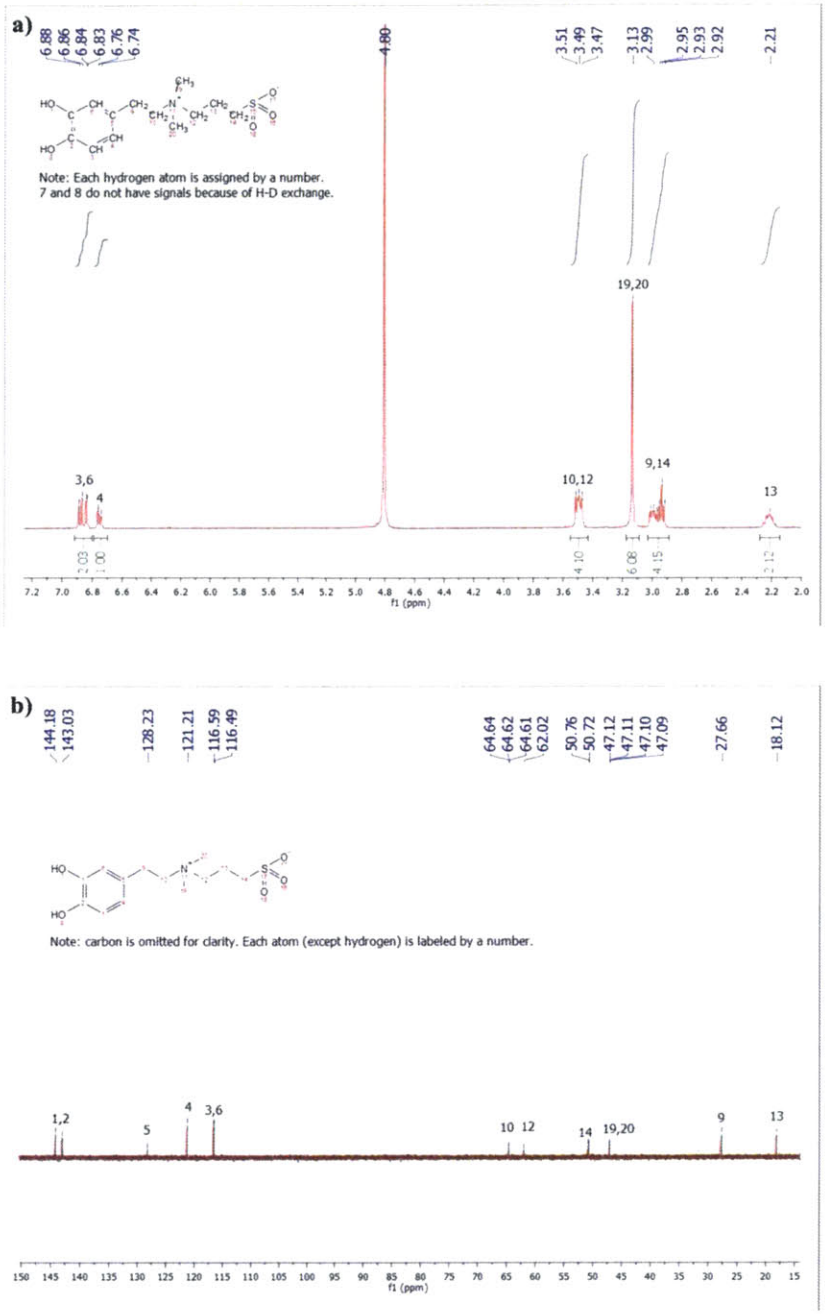

Figure 3.7 a) ^{1}H NMR and b) ^{13}C NMR of ZDS ligand. Reprinted with permission from (Wei H.; et al. "Compact Zwitterion-Coated Iron Oxide Nanoparticles for Biological Applications" Nano Letters 2012, 12, 22). Copyright (2011) American Chemical Society.

3.3 Thiol-terminated catechol derivatives

3.3.1 Design of thiol-terminated catechol-derivative

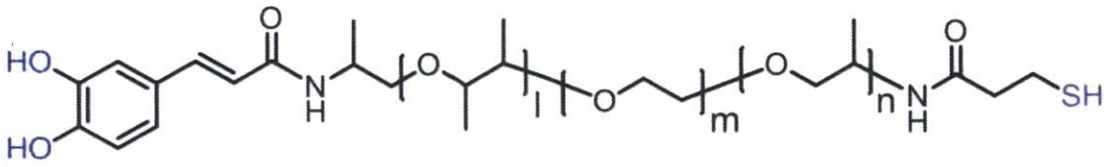

Figure 3.8 Chemical structure of thiol-terminated catechol-derivative (TD) ligand

Although ZDS ligand allowed for the realization of hydrophilic, small, and compact MNPs, the ZDS ligand itself does not have a functional group for further conjugations. To solve this problem, a new ligand, which incorporates the advantages (strong binding to iron oxide surface, high water solubility, and electrically neutral nature) of ZDS ligand and addresses its limitations (the absence of functional group), was therefore designed. The dopamine moiety, sulfonate group, and quaternary amine group will remain in the new ligand, and the main work will be introducing an appropriate functional group. Amino groups, thiol groups, carboxyl groups, and hydroxyl groups are all well-established functional groups for bioconjugate techniques,[51] but the amino group, carboxyl group, and hydroxyl group are known to bind to iron oxide nanoparticles.[42, 45, 52] As a result, the thiol group would be a suitable functional group for providing versatile derivatization pathways to the new ligand using standard thiol-maleimide conjugation scheme. Figure 3.8 shows the as-designed thiol-terminated catechol-derivative (TD) ligand, where a thiol group and a glycol (for water solubility) moiety are linked to the catechol by stable amide bonds.

3.3.2 Synthesis of thiol-terminated catechol-derivative

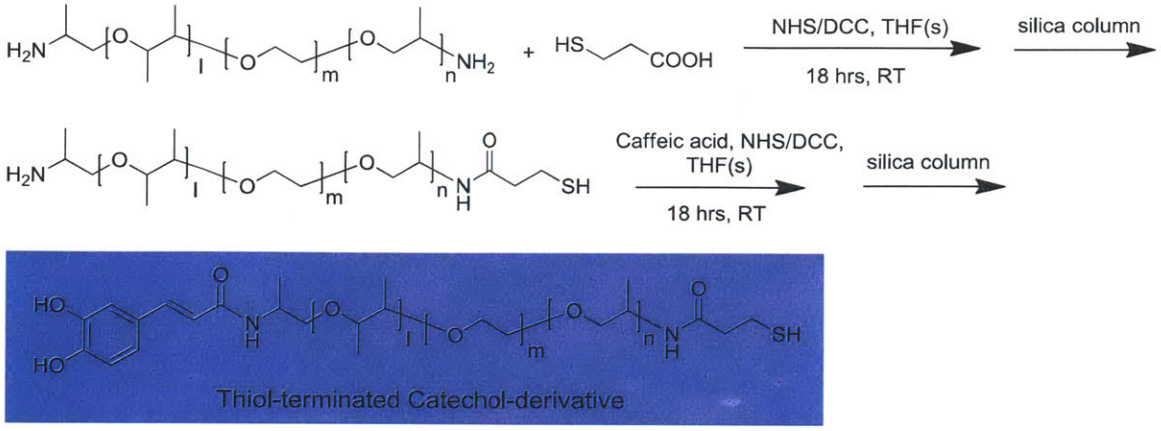

Figure 3.9 Synthetic route of thiol-terminated catechol-derivative (TD) ligand. Reprinted with permission from (Wei H.; et al. "Compact Zwitterion-Coated Iron Oxide Nanoparticles for Biological Applications" Nano Letters 2012, 12, 22). Copyright (2011) American Chemical Society.

Thiol-terminated catechol-derivative was synthesized by two steps of the simple N-hydroxysuccinic anhydride / N,N'-Dicyclohexylcarbodiimide (NHS/DCC) coupling reaction. Experimental details of this synthesis can be found in the supporting information of our publication.[53] Briefly, 3-mercaptopropionic acid was allowed to react with NHS/DCC in a tetrahydrofuran (THF) solvent at room temperature for 18 hrs, yielding 3-mercaptopropionic NHS ester. After purification, 3-mercaptopropionic NHS ester and triethyl amine were added into a THF solution containing O,O′ -Bis(2-aminopropyl) polypropylene glycol-block-polyethylene glycol-block-polypropylene glycol (Jeffamine® ED-600); this reaction was allowed to proceed at room temperature for another 18 hrs. After the product was purified by silica column with methanol/dichloromethane eluents, thiol-terminated Jeffamine® ED-600 was obtained. Second, caffeic acid was allowed to react with NHS/DCC in a THF solvent at room

temperature for 18 hrs, yielding caffeic NHS ester. Similarly, caffeic NHS ester and triethyl amine were added into a THF solution containing thiol-terminated Jeffamine® ED-600; this reaction was also allowed to proceed at room temperature for another 18 hrs, yielding thiol-terminated catechol-derivative as a crude product. The purified thiol-terminated catechol-derivative was again given by silica column separation using methanol/dichloromethane eluents.

3.4 Alkyne-terminated catechol derivatives

3.4.1 Design of alkyne-terminated catechol-derivative

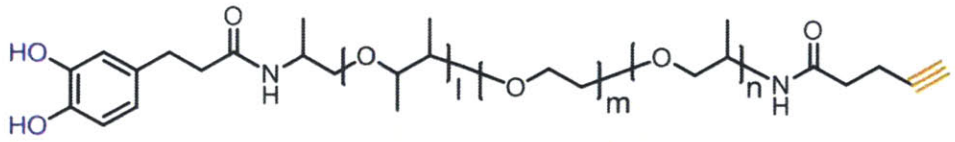

Figure 3.10 Chemical structure of alkyne-terminated catechol-derivative (AD) ligand

Although the thiol group is well-established for thiol-maleimide conjugation schemes, the thiol group is easily to be oxidized in air to form a disulfide bond.[54] The resulting disulfide bond cannot participate in thiol-maleimide conjugation, and the formation of disulfide bond may cause thiol coated nanoparticles (NPs) to cross-link and aggregate. Therefore, prior to the thiol-maleimide conjugation, the use of a reducing agent such as dithiothreitol or tris(2-carboxyethyl) phosphine is necessary for the reduction of disulfide bond into free thiol group.[55] In order to improve the stability of TD ligand, we have designed the alkyne-terminated catechol-derivative (AD) ligand. The alkyne group has the advantage of high stability and the related alkyne-azide

cycloaddition is a bio-orthogonal conjugation (click chemistry).[56] As shown in Figure 3.10, the chemical structure of AD ligand is almost the same as TD ligand, except that the thiol group in TD is changed into the alkyne group in AD and that the caffeic acid moiety in TD is changed into the dihydrocaffeic acid moiety in AD.

3.4.2 Synthesis of alkyne-terminated catechol-derivative

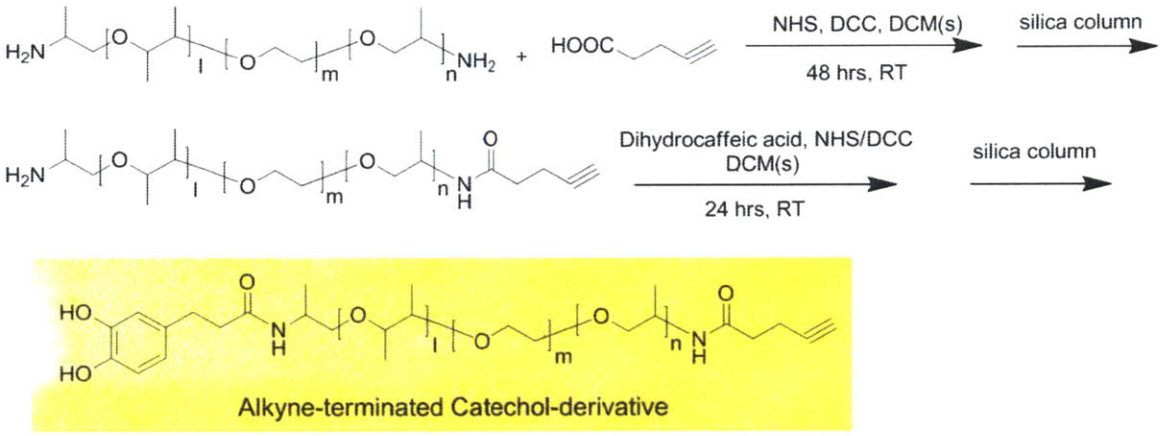

Figure 3.11 Synthetic route of alkyne-terminated catechol-derivative (AD) ligand

Figure 3.11 shows the synthetic pathway of alkyne-terminated catechol derivative (AD) ligand. Similar to the synthetic pathway of TD ligand, twos steps of NHS/DCC coupling reaction were also used here. Briefly, 4-pentynoic acid reacted with NHS/DCC in a dichloromethane (DCM) solvent at room temperature for 2 hrs, yielding 4-pentynoic NHS ester. The purified 4-pentynoic NHS ester in a DCM solution was added to triethyl amine and Jeffamine® ED-600 and the reaction was allowed to proceed at 0 °C and room temperature for a total period of 48 hrs. After the silica column purification with methanol/dichloromethane as eluents, alkyne-

terminated Jeffamine® ED-600 was obtained. Second, dihydrocaffeic acid reacted with NHS/DCC in a tetrahydrofuran (THF) solvent at room temperature for 18 hrs, resulting dihydrocaffeic NHS ester. Afterwards, to a mixed DCM and THF solvent containing alkyne-terminated Jeffamine® ED-600, dihydrocaffeic NHS ester and triethyl amine were added and the reaction was allowed to proceed at room temperature for 24 hrs. The resulting crude product of alkyne-terminated catechol-derivative was later purified by silica column again using methanol/dichloromethane eluents.

3.4.3 Experimental details

Synthesis of Alkyne-terminated Catechol-derivative. As described in Figure 3.11, the synthetic scheme of AD ligand is similar to that of TD ligand.[53] First, 4-pentynoic acid (1.117 g, 12 mmol) was added to a solvent of 50 mL dichloromethane (DCM), followed by successive addition of N-hydroxysuccinic anhydride (NHS, 1.52 g, 13.2 mmol) and N,N'-Dicyclohexylcarbodiimide (DCC, 2.72 g, 13.2 mmol). The reaction was allowed to proceed at room temperature (RT) for 2 hrs before it was filtered and its solvent was rotary evaporated, yielding 4-pentynoic NHS ester. 7.2 g (12 mmol) O,O'-Bis(2-aminopropyl) polypropylene glycol-block-polyethylene glycol-block-polypropylene glycol (Jeffamine® ED-600) and triethyl amine (TEA, 1.21 g, 12 mmol) were added into a 200 mL flask, followed by the slow addition of above 4-pentynoic NHS ester in a solution of 50 mL DCM. The resulting solution was first cooled with an ice bath and then it was allowed to react at RT for 48 hrs, filtered, and the solvent was removed using a rotary evaporator. The crude product was purified by silica gel chromatography with 10% MeOH/Dichloromethane (v/v) as the eluent, yielding alkyne-

terminated Jeffamine® ED-600. Separately, dihydrocaffeic acid (2.68 g, 14.7 mmol) was added to a solvent of 135 mL tetrahydrofuran (THF), followed by successively adding N-hydroxysuccinic anhydride (NHS, 1.86 g, 16.2 mmol) and N,N'-Dicyclohexylcarbodiimide (DCC, 3.34 g, 16.2 mmol). The reaction (under nitrogen protection) was allowed to proceed at room temperature (RT) for 18 hrs before it was filtered and its solvent was rotary evaporated, yielding dihydrocaffeic NHS ester which was later washed by ethyl acetate (EtOAc) against silica gel for purification and the solvent was then rotary evaporated. Next, the alkyne-terminated Jeffamine® ED-600 was dissolved in 60 mL DCM plus 20 mL THF, followed by the addition of the dihydrocaffeic NHS ester (2.52 g, 9 mmol) and TEA (0.91 g, 9 mmol). This reaction (under nitrogen protection) was allowed to proceed at RT for 24 hrs before it was filtered and its solvent was rotary evaporated. Finally, the crude product was purified by silica gel chromatography with 15% MeOH/Dichloromethane (v/v) as the eluent, yielding the alkyne-terminated catechol-derivative (AD) ligand. The presence of alkyne groups was confirmed by potassium permanganate test and the presence of catechol groups was confirmed by iron(III) chloride test.

4. Chapter 4: Preparations and characterizations of hydrophilic magnetic nanoparticles

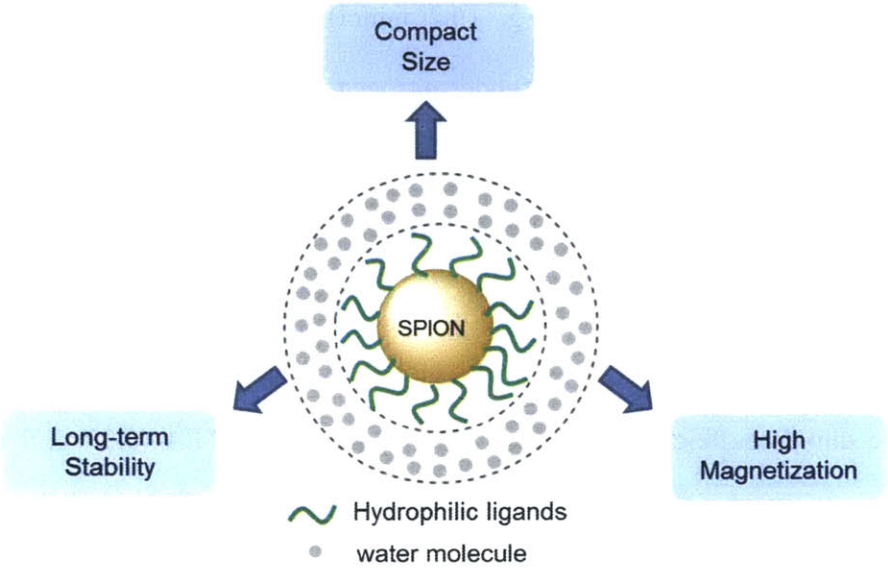

4.1 Preparations of hydrophilic magnetic nanoparticles

4.1.1 Zwitterionic dopamine sulfonate ligand coated magnetic nanoparticles

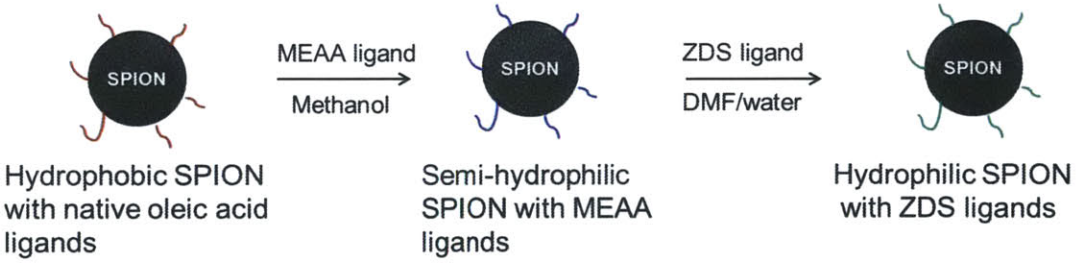

Figure 4.1 Ligand exchange pathway for the preparation of ZDS coated magnetic nanoparticles

As shown in Figure 4.1, the ligand exchange of oleic acid coated superparamagnetic iron oxide nanoparticles (SPIONs) with zwitterionic dopamine sulfonate (ZDS) ligand was achieved

by a two-step process. First, native oleic acid was exchanged by 2-[2-(2-methoxyethoxy)ethoxy] acetic acid (MEAA) ligand in a methanol (MeOH) solvent at 70 °C for 5 hrs. The reason for using MEAA as an intermediate ligand is: 1) hydrophobic SPIONs are not soluble in dimethylformamide (DMF) or water, 2) ZDS is highly hydrophilic and it can only be dissolved in highly polar solvents such as DMF or water (ZDS is almost insoluble in MeOH), and 3) MEAA is soluble in both MeOH and DMF/water mixture. Therefore, after the first step ligand exchange, the MEAA coated SPIONs (MEAA-SPIONs) can be dispersed in DMF/water mixture, which is the solvent of the second step ligand exchange. The MEAA-SPIONs in MeOH were precipitated by adding acetone and hexane. Subsequent centrifugation yielded a supernatant containing oleic acid and excess MEAA, leaving the purified MEAA-SPIONs as a pellet at the bottom.

Second, the intermediate MEAA ligand was exchanged by ZDS ligand in a DMF/water mixed solvent at 70 °C for 12 hrs. The catechol group of ZDS ligand has a stronger binding affinity towards iron oxide surface, compared to that of the carboxylic group of MEAA ligand. Therefore, MEAA ligand is likely to be completely exchanged by ZDS ligand. The resulting ZDS coated SPIONs (ZDS-SPIONs) are highly hydrophilic and they can be purified by adding acetone into the DMF/water mixture containing ZDS-SPIONs. After centrifugation, the purified ZDS-SPIONs pellet at bottom can be well dispersed in water or phosphate buffered saline 1X (PBS 1X). The excess ZDS ligand can be removed by using a dialysis centrifugal unit afterwards.

4.1.2 Thiol-terminated catechol-derivative and zwitterionic dopamine sulfonate ligand mixture coated magnetic nanoparticles

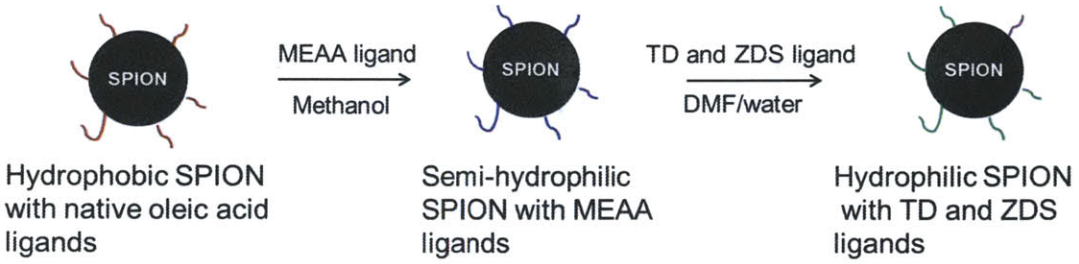

Figure 4.2 Ligand exchange pathway for the preparation of TD and ZDS coated magnetic nanoparticles

As shown in Figure 4.2, the ligand exchange process with a mixture of thiol-terminated catechol-derivative (TD) and zwitterionic dopamine sulfonate (ZDS) ligands is almost the same as the ligand exchange process of pure ZDS ligand. First, same procedures were used to prepare the intermediate MEAA coated SPIONs that can be dispersed in DMF/water mixture. Second, same procedures were used to prepare TD/ZDS coated SPIONs, except that a mixture of TD and ZDS ligand was used instead of pure ZDS ligand. The nitrogen gas protection is more important here, as the free thiol groups are prone to cross-link in air. The resulting TD/ZDS coated SPIONs can also be well dispersed in water or PBS 1X. 15% TD and 85% ZDS (mol%) was found to be an optimal ratio of this ligand mixture in terms of the water-solubility as well as functionality of SPIONs.

4.1.3 Alkyne-terminated catechol-derivative and zwitterionic dopamine sulfonate ligand mixture coated magnetic nanoparticles

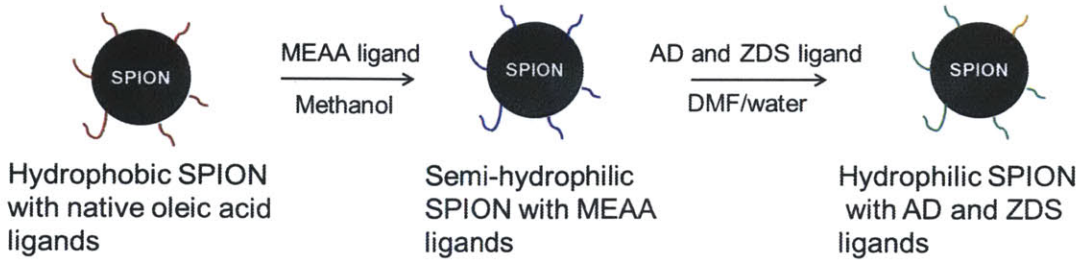

Figure 4.3 Ligand exchange pathway for the preparation of AD and ZDS coated magnetic nanoparticles

Figure 4.3 depicts the pathway for the preparation of Alkyne-terminated catechol-derivative (AD) and zwitterionic dopamine sulfonate (ZDS) ligand mixture coated SPIONs. Similarly, MEAA coated SPIONs were first prepared using the same procedures; afterwards, in order to prepare AD/ZDS coated SPIONs, a mixture of AD and ZDS ligands was used instead of pure ZDS ligand while other procedures were the same. Unlike TD ligand, the AD ligand used here is stable in air.

4.1.4 Experimental details

Ligand exchange with pure DS or ZDS. Ethanol was first added to 25 μL SPION stock solution to precipitate the SPIONs. The resulting solution was centrifuged and then the supernatant was discarded, yielding ~1 mg of dry SPION pellet. 25 μL of 2-[2-(2-methoxyethoxy)ethoxy]acetic acid (MEAA) and 75 μL of methanol (solvent) were added to the SPION pellet, and the reaction mixture was allowed to proceed at 70 °C for 5 hrs before it was

precipitated by the addition of 0.2 mL acetone and 0.8 mL hexane in succession. The resulting cloudy solution was centrifuged again and then the supernatant was discarded, yielding a pellet of MEAA coated SPIONs. Then, ~50 mg of pure DS or ZDS ligand in a mixed solvent of 0.6 mL dimethylformamide (DMF) and 0.3 mL de-ionized water was added to the pellet of MEAA coated SPIONs and the reaction was allowed to proceed at 70 °C for 12 hrs. Upon the completion of ligand exchange, the solution turned into a black color and it was then precipitated by the addition of 5 mL acetone. Next, the solution was centrifuged and the supernatant was again discarded, yielding a pellet of DS or ZDS coated SPIONs, to which 1 mL phosphate buffered saline 1X (PBS 1X) was added to disperse the SPIONs. The DS or ZDS coated SPIONs in PBS 1X were sonicated for 40 min and purified by a dialysis centrifugal unit (by plain PBS 1X, 3 times) to remove excess ligand.

Ligand exchange with a mixture of TD and ZDS. MEAA-coated SPIONs were first prepared using the same procedure as described above. Then, ~50 mg of 15% TD and 85% ZDS ligands (mol%) in a mixed solvent of 0.6 mL dimethylformamide (DMF) and 0.3 mL de-ionized water were added to the pellet of MEAA coated SPIONs and the reaction (under the protection of nitrogen gas) was allowed to proceed at 70 °C for 12 hrs. Upon the completion of ligand exchange, the solution turned into a black color and it was then precipitated by the addition of 5 mL acetone. Next, the solution was centrifuged and the supernatant was again discarded, yielding a pellet of TD and ZDS coated SPIONs, to which 1 mL phosphate buffered saline 1X (PBS 1X) was added to disperse the SPIONs. The TD and ZDS coated SPIONs in PBS 1X were sonicated for 40 min and purified by a dialysis centrifugal unit (by plain PBS 1X, 3 times) to remove excess ligand.

Ligand exchange with a mixture of AD and ZDS. MEAA-coated SPIONs were first prepared using the same procedure as described above. Then, ~50 mg of 15% AD and 85% ZDS ligands (mol%) in a mixed solvent of 0.6 mL dimethylformamide (DMF) and 0.3 mL de-ionized water were added to the pellet of MEAA coated SPIONs and the reaction was allowed to proceed at 70 °C for 12 hrs. Upon the completion of ligand exchange, the solution turned into a black color and it was then precipitated by the addition of 5 mL acetone. Next, the solution was centrifuged and the supernatant was again discarded, yielding a pellet of AD and ZDS coated SPIONs, to which 1 mL phosphate buffered saline 1X (PBS 1X) was added to disperse the SPIONs. The AD and ZDS coated SPIONs in PBS 1X were sonicated for 40 min and purified by a dialysis centrifugal unit (by plain PBS 1X, 3 times) to remove excess ligand.

4.2 Transmission electron microscopy of hydrophilic magnetic nanoparticles

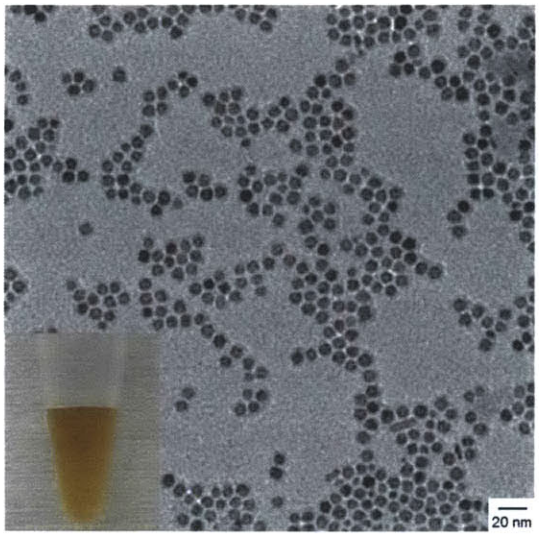

Figure 4.4 TEM image of ZDS ligand coated SPIONs. Inset: Photograph of ZDS ligand coated SPIONs dispersed in PBS 1X. Reprinted with permission from (Wei H.; et al. "Compact Zwitterion-Coated Iron Oxide Nanoparticles for Biological Applications" Nano Letters 2012, 12, 22). Copyright (2011) American Chemical Society.

The photograph in the inset of Figure 4.4 shows that, on a macroscopic level, ZDS ligand coated SPIONs (ZDS-SPIONs) were stable at a high nanoparticle (NP) concentration and those ZDS-SPIONs can be well dispersed in phosphate buffered saline 1X (PBS 1X). In order to understand the dispersion of ZDS-SPIONs on a microscopic level, transmission electron microscopy (TEM) was used. As shown in Figure 4.4, TEM further revealed that the ZDS-SPIONs had an inorganic diameter of ~8 nm. Moreover, there was no noticeable aggregation of ZDS-SPIONs – they were nearly monodisperse. These results suggest that, as designed, ZDS ligand is highly water-soluble and ZDS ligand has a strong binding affinity towards iron oxide surface.

4.3 Dynamic light scattering of hydrophilic magnetic nanoparticles and their pH stability

4.3.1 Dynamic light scattering measurements

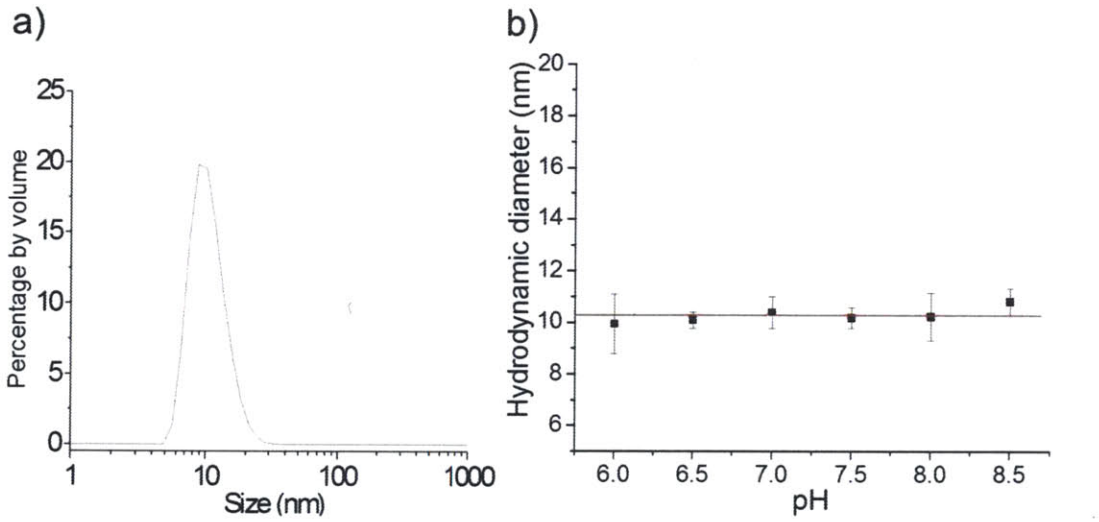

Figure 4.5 Dynamic light scattering measurements showing a) The distribution of hydrodynamic diameter of ZDS ligand coated SPIONs and b) the stability of hydrodynamic diameter of ZDS ligand coated SPIONs over the physiological pH range. Adapted with permission from (Wei H.; et al. "Compact Zwitterion-Coated Iron Oxide Nanoparticles for Biological Applications" Nano Letters 2012, 12, 22). Copyright (2011) American Chemical Society.

Admittedly, the transmission electron microscopy (TEM) image in Figure 4.4 shows about hundreds of nearly monodisperse ZDS ligand coated SPIONs (ZDS-SPIONs). However, a typical SPION sample used for biomedical research has a large number of nanoparticles (NPs) which can be on the order of 1×10^{-9} mol (1 nmol). In order to statistically study the distribution of hydrodynamic diameter (HD) of ZDS-SPIONs, dynamic light scattering (DLS) measurement

was used. Figure 4.5a shows a nearly symmetric HD distribution of ZDS-SPIONs that were dispersed in PBS 1X at pH=7.5. The average HD of ZDS-SPIONs is ~10 nm, which coincided with the peak of its HD distribution. This result suggests that ZDS-SPIONs were indeed nearly monodisperse even if a large number of SPIONs were measured. Figure 4.5b further demonstrates that the average HD of ZDS-SPIONs was insensitive to pH within the physiological pH range (6.0-8.5), indicating that the ZDS ligand does not dissociate from iron oxide surface over physiological pHs and that the ZDS ligand can retain the good colloidal stability of SPIONs in biological buffers.

Moreover, since the ZDS-SPIONs have an inorganic diameter of ~8 nm and a HD of ~10 nm, the ZDS ligand only contributes ~1 nm to the overall radius of hydrophilic SPIONs. In contrast, SPIONs that are coated by dextran ligands[44, 57] or polyethylene glycol coupled (PEGylated) ligands[48] can increase their HDs on the order of 30 to 200 nm, when compared to their inorganic core diameters. Therefore, the size increment introduced by ZDS ligand is significantly smaller than that of dextran or PEGylated ligands. This result suggests that ZDS coated SPIONs are compact when they are dispersed in PBS 1X.

4.3.2 Experimental details

Dynamic light scattering measurements. The hydrodynamic diameters (HDs) of hydrophilic SPIONs were determined by light-scattering analysis using a Malvern Instruments Nano-ZS90 machine. A volume-weighted size distribution analysis was used to obtain HDs, which were reported as the average of three parallel measurements. Each measurement was performed and

averaged for ~10 min, where each autocorrelation function was acquired for ~5 s. The error bars of HDs were reported as the standard deviation of the average given by triplicate measurements.

4.4 Stability of hydrophilic magnetic nanoparticles with respect to time

We have already shown that the hydrophilic ZDS ligand coated SPIONs (ZDS-SPIONs) can be well dispersed in PBS 1X with a small hydrodynamic diameter. However, biomedical applications also require SPIONs to be stable in a reasonable amount of time, including but not limited to the time used for preparation, purification, storage, as well as delivery and so on. To this end, UV-Vis spectra and size-exclusion high-performance liquid chromatography (HPLC) were used to study the long-term stability of ZDS-SPIONs in PBS 1X.

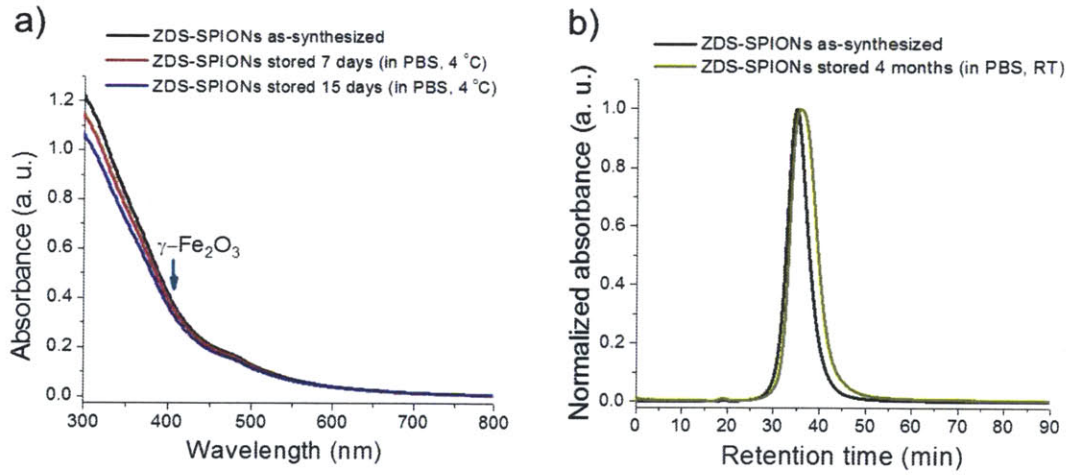

Figure 4.6 a) UV-Vis spectra and b) size-exclusion HPLC chromatograms of ZDS ligand coated SPIONs (ZDS-SPIONs) with increasing storage time; a) Reprinted with permission from (Wei H.; et al. "Compact Zwitterion-Coated Iron Oxide Nanoparticles for Biological Applications" Nano Letters 2012, 12, 22). Copyright (2011) American Chemical Society.

4.4.1 UV-Vis absorbance measurements

Figure 4.6a shows the measurements of UV-Vis absorbance of ZDS-SPIONs (with a ~8 nm inorganic diameter) in PBS 1X solution with the increase of storage time. In this experiment, the UV-Vis absorbance reflects the concentration of ZDS-SPIONs in PBS 1X: if the ZDS-SPIONs aggregated and precipitated to the bottom of cell during the storage, then the UV-Vis absorbance will decrease accordingly. As shown in Figure 4.6a, the UV-Vis absorbance of ZDS-SPIONs as-synthesized (black), stored seven days (red), and stored fifteen days (blue) were nearly identical, indicating that the ZDS-SPIONs are stable at 4 °C in PBS 1X for at least two weeks. Moreover, ZDS-SPIONs were found to be soluble even in saturated sodium chloride aqueous solution. In contrast, aggregations of nanoparticles (NPs) can be observed for PEGylated ligands coated NPs or single charge-stabilized NPs in sodium chloride aqueous solution.[58] Moreover, researchers have previously found that simple dopamine molecule coated SPIONs may have rapid degradation, forming iron(III) oxyhydroxide.[59] For our ZDS-SPIONs, we did not observe these instability behaviors.

4.4.2 Size-exclusion HPLC chromatograms

Figure 4.6b shows the size-exclusion HPLC chromatogram of ZDS-SPIONs (with a ~3 nm inorganic diameter). The size-exclusion HPLC stands for a HPLC machine equipped with a size-exclusion column, in which the retention time of SPIONs has an inversed relationship with the hydrodynamic diameter (HD) of SPIONs.[60] Moreover, the inversed relationship between the retention time of SPIONs and the HD of SPIONs can be plotted in a calibration curve using

protein standards with known HDs. As shown in Figure 4.6b, the retention time distribution (RTD) of ZDS-SPIONs as-synthesized was nearly identical to the RTD of ZDS-SPIONs stored 4 months. Moreover, the peak of RTD of ZDS-SPIONs as-synthesized was almost the same as the peak of RTD of ZDS-SPIONs stored 4 months. These results suggest that ZDS-SPIONs are stable at room temperature in PBS 1X for four months. The high stability of ZDS-SPIONs in biological buffers can be attributed to the strong binding affinity of 3,4-dihydroxybenzene anchor group and the high water solubility of sulfonate group.

4.4.3 Experimental details

Size-exclusion high-performance liquid chromatography. Zwitterionic dopamine sulfonate coated SPIONs (ZDS-SPIONs) in a solvent of phosphate buffered saline 1X (PBS 1X) were first filtered by 0.2 μm HT Tuffryn® membranes, and then the filtered ZDS-SPIONs were injected into a high-performance liquid chromatography (HPLC, manufactured by Agilent Technologies) machine equipped with a size-exclusion column (Superose™ 6, GE Healthcare, 10/300 GL). The PBS 1X was used as the eluent and the absorbance of ZDS-SPIONs at 400 nm was monitored (referencing to 600 nm) for 90 mins. The resulting HPLC chromatograms were normalized by absorbance intensity or integration area.

4.5 SQUID measurements of magnetic nanoparticles

The magnetic properties of as-prepared SPIONs are crucial to their biomedical applications; for example, magnetic separation and hyperthermia both require a high saturation magnetization of SPIONs. In this respect, superconducting quantum interference device (SQUID) was used to carefully investigate the magnetic behaviors, including superparamagnetism and saturation magnetization, of as-prepared SPIONs.

4.5.1 Magnetic behavior of oleic acid coated magnetic nanoparticles

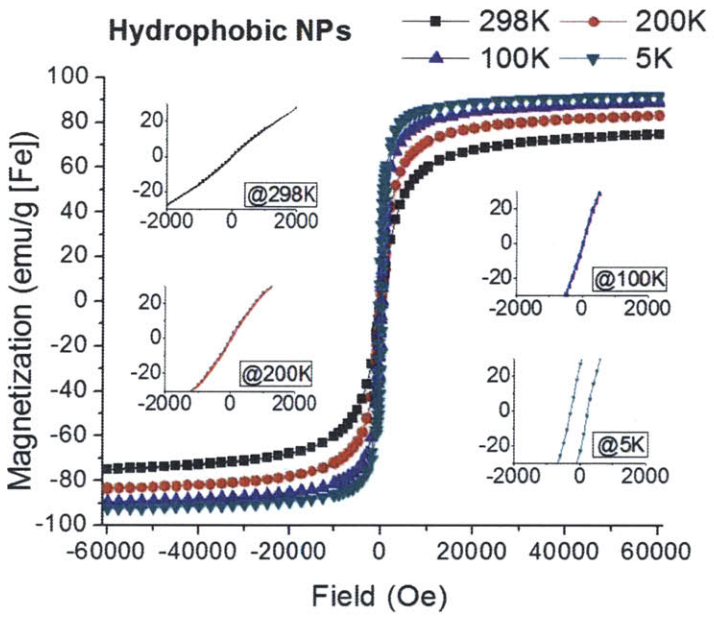

Figure 4.7 SQUID curves of oleic acid coated hydrophobic SPIONs measured at four different temperatures. Adapted from (Wei H.; et al. "Compact zwitterion-coated iron oxide nanoparticles for in vitro and in vivo imaging" Integrative Biology 2013, 5, 108). Reproduced by permission of The Royal Society of Chemistry.

As shown in Figure 4.7, the saturation magnetization and magnetic response of oleic acid coated hydrophobic SPIONs (hydrophobic SPIONs) with an inorganic diameter of ~6 nm were measured by SQUID from -60000 to 60000 Oe (i.e. -6 to 6 Tesla) at 5 K, 100 K, 200 K, and 298

K, separately. The insets in Figure 4.7 clearly show that, at 100 K, 200 K, and 298 K, the hydrophobic SPIONs did not have any hysteresis loop near zero magnetic fields. The hydrophobic SPIONs are indeed superparamagnetic at these temperatures, in which the superparamagnetism at 298 K is the most important because the majority of biomedical applications of SPIONs were done at room temperature or human body temperature. When the temperature was cooled down to 5 K, the hydrophobic SPIONs started to show a hysteresis loop near zero magnetic fields, indicating ferromagnetism of hydrophobic SPIONs at 5 K. This phenomenon is consistent with the reported blocking temperature (~30 K) of maghemite nanoparticles with a ~6 nm inorganic diameter.[61]

In order to calculate the magnetization of SPIONs in a unit of emu/g [Fe] and compare the result with reported values, the mass of iron in hydrophobic SPION sample was determined by using bathophenanthroline (see experimental details in the materials and methods in our publication).[62] After iron determination, the saturation magnetization (M_s) of the hydrophobic SPIONs at 298 K was found to be ~74 emu/g [Fe]. This value compares reasonably well with 106 emu/g [Fe] (i. e., 74 emu/g [Fe_2O_3]), the bulk value of maghemite.[63]

4.5.2 Magnetic behavior of 2-[2-(2-methoxyethoxy)ethoxy]acetic acid coated magnetic nanoparticles

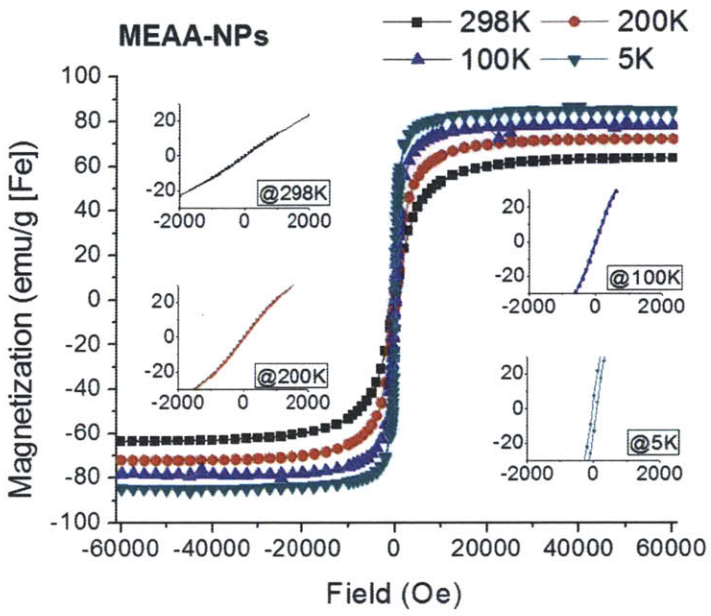

Figure 4.8 SQUID curves of 2-[2-(2-methoxyethoxy)ethoxy]acetic acid coated SPIONs (MEAA-SPIONs) measured at four different temperatures. Adapted from (Wei H.; et al. "Compact zwitterion-coated iron oxide nanoparticles for in vitro and in vivo imaging" Integrative Biology 2013, 5, 108). Reproduced by permission of The Royal Society of Chemistry.

As shown in Figure 4.8 and its insets, SQUID measurements of 2-[2-(2-methoxyethoxy)ethoxy]acetic acid coated SPIONs (MEAA-SPIONs) with magnetic fields ranging from -60000 to 60000 Oe (i. e. -6 to 6 Tesla) also revealed that there were no hysteresis loop of MEAA-SPIONs at 100 K, 200 K, and 298 K. Therefore, the MEAA-SPIONs are also superparamagnetic at 100 K, 200 K, and most importantly 298 K. Similar to the hydrophobic SPIONs, when the temperature was cooled down to 5 K, ferromagnetism has shown in the MEAA-SPIONs. However, the magnetic coercivity of MEAA-SPIONs was smaller than that of hydrophobic SPIONs at 5 K. This is presumably due to changed magnetic coupling between

SPIONs, where different ligand coatings of SPIONs can change the spacing intervals of SPIONs that in turn affect the magnetic coupling.[64]

After determining the mass of iron by bathophenanthroline, the saturation magnetization (M_s) of MEAA-SPIONs was found to be ~63 emu/g [Fe], which is close to the M_s value (~74 emu/g [Fe]) of hydrophobic SPIONs. This result suggests that the MEAA ligand coating does not significantly change the M_s of as-synthesized hydrophobic SPIONs.

4.5.3 Magnetic behavior of zwitterionic dopamine sulfonate and thiol-terminated catechol-derivative coated magnetic nanoparticles

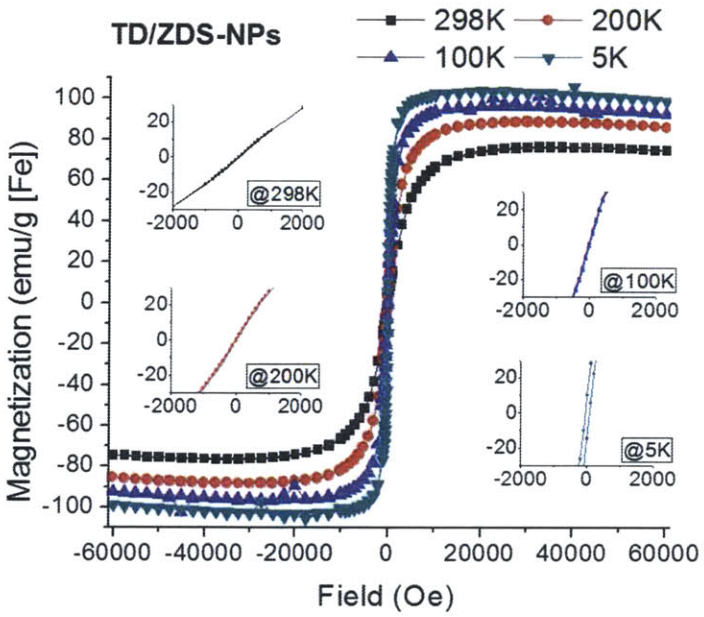

Figure 4.9 SQUID curves of thiol-terminated catechol-derivative and zwitterionic dopamine sulfonate coated SPIONs (TD/ZDS-SPIONs) measured at four different temperatures. Adapted from (Wei H.; et al. "Compact zwitterion-coated iron oxide nanoparticles for in vitro and in vivo imaging" Integrative Biology 2013, 5, 108). Reproduced by permission of The Royal Society of Chemistry.

Figure 4.9 and its insets show the SQUID curves of SPIONs that were coated by a mixture of thiol-terminated catechol-derivative and zwitterionic dopamine sulfonate (TD/ZDS-SPIONs). Similarly, the SQUID curves are measured at 5K, 100 K, 200 K, and 298 K with magnetic fields ranging from -60000 to 60000 Oe (i. e. -6 to 6 Tesla). Like hydrophobic SPIONs and MEAA-SPIONs, the TD/ZDS-SPIONs also showed ferromagnetism at 5 K. Moreover, TD/ZDS-SPIONs were confirmed to be superparamagnetic at 100 K, 200 K, and 298 K.

After the mass of iron in the TD/ZDS-SPION sample was determined, the saturation magnetization (M_S) of TD/ZDS-SPIONs was found to be ~74 emu/g [Fe]. This M_S value is the same as the M_S value of hydrophobic SPIONs, within the error range of SQUID measurements.

These results suggest that the new ligand coatings designed by us do not significantly affect the M_S of as-synthesized hydrophobic SPIONs and that our optimized heating, precipitation, sonication, and dialysis procedures in the processes of ligand exchange and purification do not significantly alter the M_S of as-synthesized hydrophobic SPIONs. Moreover, the magnetic behaviors such as superparamagnetism of hydrophobic SPIONs are largely insensitive to the processes of ligand exchange and purification. These unaltered magnetic properties indicate that the hydrophilic TD/ZDS-SPIONs can retain the highly magnetic performances of as-synthesized hydrophobic SPIONs, which in turn makes TD and ZDS promising ligands for various biomedical applications.[65]

5. Chapter 5: In vitro and in vivo biocompatibility and functionality of hydrophilic magnetic nanoparticles

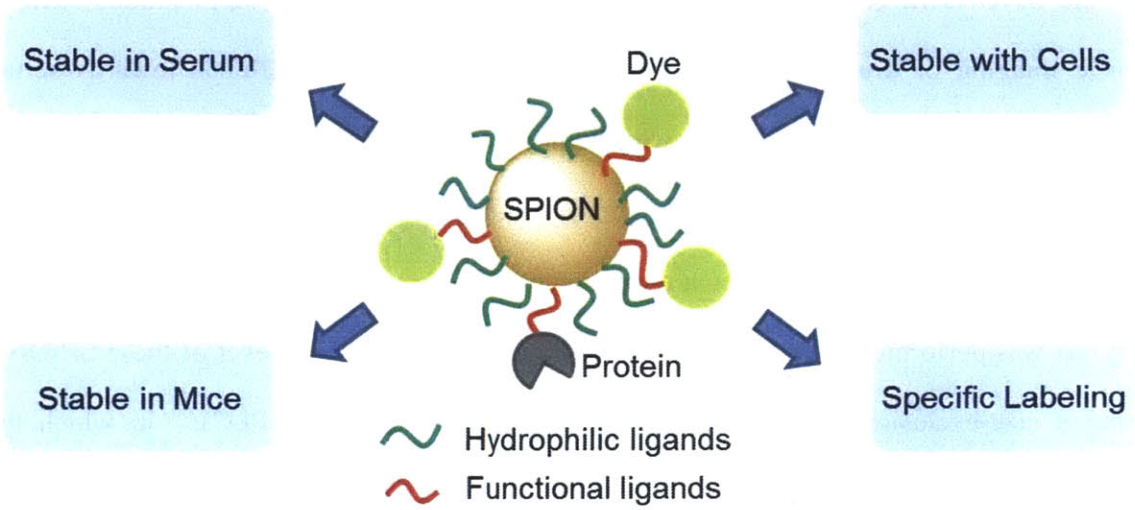

In Chapter 4, we have already shown that the as-prepared hydrophilic superparamagnetic iron oxide nanoparticles (SPIONs) can be well dispersed in biological buffers, showing compact overall size, long-term stability, and high saturation magnetization. These properties of our hydrophilic SPIONs are important and desired for biomedical applications; however, successful applications of SPIONs in biomedicine further require them to have biocompatibility and functionality. To this end, we report here the designs and results of in vitro and in vivo experiments that can evaluate the biocompatibility and functionality of hydrophilic SPIONs (i. e. NPs in this chapter for simplicity).

5.1 In vitro serum binding test

5.1.1 Design of in vitro serum binding test

For the SPIONs (i. e. NPs for simplicity) to be used in biomedical applications such as diagnostic imaging or drug delivery, a low non-specific binding of SPIONs towards serum proteins is a critical property.[66] SPIONs with high non-specific binding property are generally bio-fouling and they can be sticky to serum protein, leading to a large increment of hydrodynamic diameters (HDs) or even a formation of aggregates. To this end, an in vitro serum binding test was performed in order to evaluate the non-specific binding level of these SPIONs. By using a size-exclusion high-performance liquid chromatography (HPLC),[60] in which the retention times of SPIONs have an inversed relationship with the HDs of SPIONs, we were able to compare the HDs of SPIONs incubated with plain phosphate buffered saline 1X (PBS) and fetal bovine serum (FBS). The experimental details can be found in the supporting information of our publication.[53] Here the DS-NPs were used as a control to ZDS-NPs: although both DS-NPs and ZDS-NPs can be well dispersed in PBS, the surface charge of DS-NPs is negative (from sulfonate group) while the surface charge of ZDS-NPs is nearly neutral (from a combination of sulfonate and quaternary amine groups). Electrostatic interactions are thought to play an important role in binding between SPIONs and a major component of FBS – bovine serum albumin,[67] and thus DS-NPs are expected to show a higher non-specific binding affinity towards serum proteins.

5.1.2 Stability of dopamine sulfonate coated magnetic nanoparticles and zwitterionic dopamine sulfonate coated magnetic nanoparticles

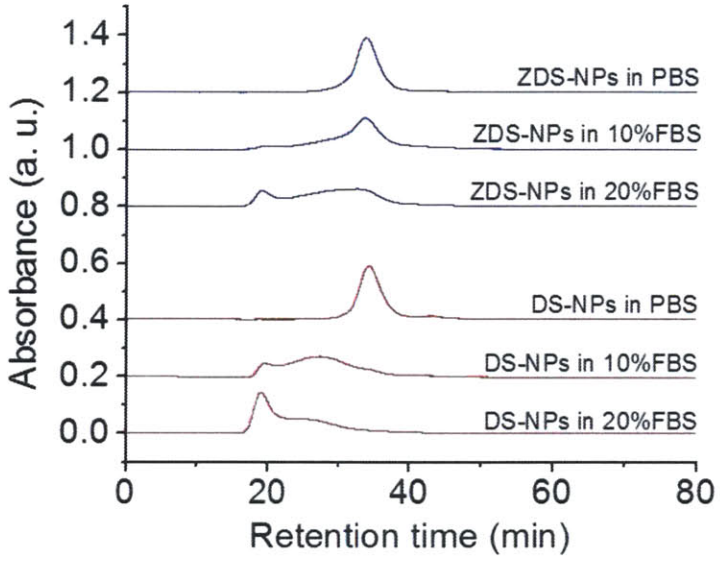

Figure 5.1 Red curves: size-exclusion chromatograms of dopamine sulfonate coated iron oxide nanoparticles (DS-NPs) in phosphate buffered saline (PBS) and fetal bovine serum (FBS). Blue curves: size-exclusion chromatograms of zwitterionic dopamine sulfonate coated iron oxide nanoparticles (ZDS-NPs) in PBS and FBS. Adapted with permission from (Wei H.; et al. "Compact Zwitterion-Coated Iron Oxide Nanoparticles for Biological Applications" Nano Letters 2012, 12, 22). Copyright (2011) American Chemical Society.

As shown in Figure 5.1, both dopamine sulfonate coated SPIONs (DS-NPs, red curves) in PBS and zwitterionic dopamine sulfonate coated SPIONs (ZDS-NPs, blue curves) in PBS were nearly monodisperse with narrow retention time distributions (RTDs) and the same retention time peaks of ~34 min. After an incubation with 10% FBS, the retention time distribution (RTD) of DS-NPs (Figure 5.1, red curves) became a broad distribution between ~20 and ~37 min. This result indicates that, compared to the hydrodynamic diameter (HD) of DS-NPs in PBS, the HD of DS-NPs significantly increased after the incubation with 10% FBS, which was as expected. In

contrast, after an incubation with 10% FBS, the RTD of ZDS-NPs (Figure 5.1, blue curves) was almost not affected when compared to the RTD of ZDS-NPs in PBS, showing a similar retention time peak of ~34 min. This data indicates that the HD of ZDS-NPs after the incubation with 10% FBS was almost the same as the HD of ZDS-NPs in PBS.

When the serum concentration was increased from 10% to 20%, SPIONs accordingly showed more noticeable changes in their HDs. After incubation with 20% FBS, the retention time distribution (RTD) of DS-NPs (Figure 5.1, red curves) shifted to a new retention time peak of ~18 min. As the flow rate of HPLC eluent in this experiment was 0.5 mL/min, 18 min corresponds to 9 mL, which is approximately the void volume of size-exclusion column. This means that the HD of DS-NPs experienced a large increment, which may lead to aggregations of DS-NPs. On the contrary, after incubation with 20% FBS, the RTD of ZDS-NPs (Figure 5.1, blue curves) only had a minor population at ~18 min and the majority of the RTD of ZDS-NPs was still between ~20 and ~37 min. Therefore, in 20% FBS, the HD of ZDS-NPs was smaller than the HD of DS-NPs. This result suggests that, although minor biological species of FBS may still bind to nearly neutral ZDS-NPs in 20% FBS,[68] the majority of ZDS-NPs showed a lower non-specific binding than that of DS-NPs in 20% FBS.

In summary, the different surface charges of DS-NPs and ZDS-NPs lead to different levels of non-specific binding to serum. Although DS-NPs were monodisperse in PBS, the negative charge of DS ligands significantly interacted with some of the proteins in FBS (e. g., albumin), making the DS-NPs unstable in higher concentration FBS. In an advance over DS-NPs, the ZDS-NPs demonstrated a reduced non-specific binding towards serum proteins in FBS, and thus ZDS-NPs were more stable in higher concentration FBS. These results therefore suggest that the electrically neutral character is critical to ligand design[69] and that zwitterionic SPIONs are more

suitable than negatively charged SPIONs for in vitro biomedical applications with the presence of serum.

5.2 In vitro cellular uptake test

5.2.1 Design of in vitro cellular uptake test

The newly developed SPION systems - zwitterionic dopamine sulfonate coated SPIONs (ZDS-SPIONs, or ZDS-NPs for simplicity) as well as a mixture of thiol-terminated catechol-derivative and ZDS coated SPIONs (TD/ZDS-SPIONs, or TD/ZDS-NPs for simplicity) - have potential in specific targeting and imaging applications after they are functionalized by antibodies, aptamers, or peptides.[70] Therefore, the evaluation of ZDS-SPIONs' and TD/ZDS-SPIONs' non-specific uptake into cells becomes an important issue, as non-specific uptake is generally undesired for above applications. To this end, non-specific cell uptakes of ZDS-NPs and TD/ZDS-NPs were studied and their results were compared with non-specific cell uptakes of other iron sources such as $FeCl_3$ and dextran coated SPIONs (Dex-SPIONs, or Dex-NPs for simplicity), which is a well-established SPION system.[71] HeLa cancerous cells were selected as the target cells, in which HeLa cells were incubated with different iron sources separately in a period of 24 hrs and the intracellular iron (if any) was then stained by Prussian blue to show a blue color. Finally the stained HeLa cells were imaged by a Carl Zeiss optical transmission microscope. Experimental details can be found in the materials and methods section in our publication.[62]

5.2.2 Iron cellular uptake

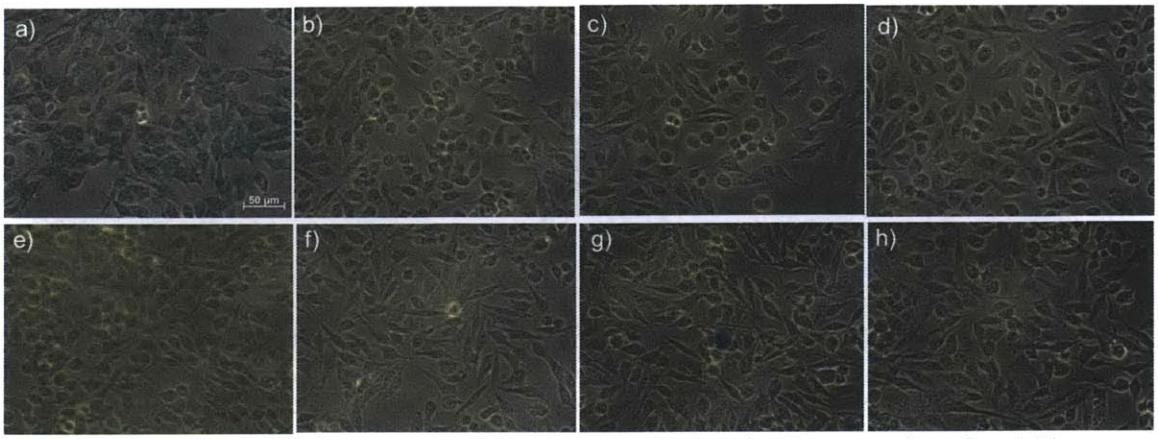

Figure 5.2 Prussian blue stained HeLa cells showing the level of iron uptake after 24 hrs incubation with: a) $FeCl_3$ (400 µg/mL), b) Control (no iron source), c) Dex-SPIONs (400 µg/mL), d) Dex-SPIONs (40 µg/mL), e) ZDS-SPIONs (400 µg/mL), f) ZDS-SPIONs (40 µg/mL), g) TD/ZDS-SPIONs (400 µg/mL), h) TD/ZDS-SPIONs (40 µg/mL). Reprinted from (Wei H.; et al. "Compact zwitterion-coated iron oxide nanoparticles for in vitro and in vivo imaging" Integrative Biology 2013, 5, 108). Reproduced by permission of The Royal Society of Chemistry.

In Figure 5.2, the iron distribution in HeLa cells was shown as blue intracellular signals. HeLa cells incubated with 400 µg/mL $FeCl_3$ showed the intracellular blue signals, indicating their non-specific uptake of the free iron source(Figure 5.2 a). On the contrary, the control HeLa cells incubated with plain cell medium and phosphate buffered saline only showed minimal intracellular iron uptake (Figure 5.2b). Meanwhile, minimal intracellular iron uptakes were also observed for the HeLa cells incubated with Dex-SPIONs, ZDS-SPIONs, and TD/ZDS-SPIONs (Figure 5.2c-h), which is similar to that of the control HeLa cells. A blue ~20 µm spot in the middle of Figure 5.2g was presumably caused by the aggregation of TD/ZDS-SPIONs with surface free thiol groups that cross-linked during the incubation process.[72] These data indicate

that Dex-SPIONs, ZDS-SPIONs, and TD/ZDS-SPIONs all have much lower non-specific cell uptakes when compared with $FeCl_3$.

More interestingly, although ZDS (MW: ~300 g/mol) and TD (MW: ~850 g/mol) are smaller ligands than dextran (MW: ~6000 g/mol), ZDS-SPIONs and TD/ZDS-SPIONs behaved almost the same as Dex-SPIONs in terms of the non-specific cellular uptake. Because the well-established Dex-SPIONs have already found their use in molecular imaging, diagnostics, and therapeutics,[73] it can be expected that ZDS-SPIONs and TD/ZDS-SPIONs with similar low non-specific cell uptakes would show their potential as specific targeting and imaging agents.[74]

5.3 In vivo stability test

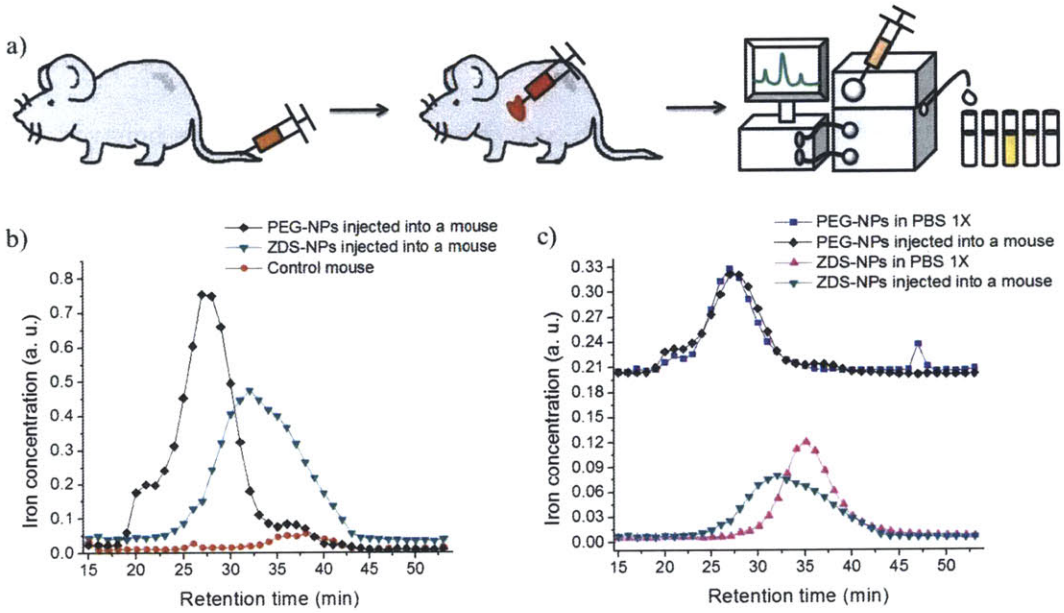

Figure 5.3 In vivo stability tests of SPIONs (i. e. NPs for simplicity) with different ligands a) experimental design, b) size-exclusion chromatograms of SPIONs injected into mice (not normalized), and c) size-exclusion chromatograms of SPIONs in PBS 1X and SPIONs injected into mice (normalized by area). Data in b) are included in c). Reprinted from (Wei H.; et al. "Compact zwitterion-coated iron oxide nanoparticles for in vitro and in vivo imaging" Integrative Biology 2013, 5, 108). Reproduced by permission of The Royal Society of Chemistry.

5.3.1 Design of in vivo stability test

Previous results in 5.1 and 5.2 have already shown that zwitterionic dopamine sulfonate coated SPIONs (ZDS-SPIONs, or ZDS-NPs for simplicity) were stable in vitro in serum and with living cells, it is now important to investigate the in vivo imaging potential of ZDS-NPs. With regards to this, an in vivo stability test was performed, where the hydrodynamic diameter (HD) of SPIONs in phosphate buffered saline 1X (PBS 1X) was compared to the HD of SPIONs injected into mice. As shown in Figure 5.3a, hydrophilic SPIONs were first introduced into mice through tail vein injections. After 10 min, the blood of mice was collected by cardiac punctuation

and the serum (containing SPIONs) was separated from the blood. By using a size-exclusion gel-filtration chromatography, where the retention times of SPIONs have an inversed relationship with the HDs of SPIONs,[60] we were able to fractionize the serum containing SPIONs. Next, the iron concentration of each fraction was determined by using bathophenanthroline (BPT) and finally the chromatograms were plotted as iron concentration (IC, y-axis) versus retention time (x-axis). Here the SPIONs encapsulated in polyethylene glycol lipid micelles (PEG-SPIONs, or PEG-NPs for simplicity) were used as a control to compare with the results of ZDS-NPs. More experimental details can be found in the materials and method section in our publication.[62]

5.3.2 Stability of zwitterionic dopamine sulfonate coated magnetic nanoparticles in vivo in mice

Figure 5.3b shows the non-normalized data of mouse injected with ZDS-NPs, mouse injected with PEG-NPs, and control mouse (no SPIONs injection). We can clearly see that the iron concentrations (ICs) in serum from mice injected with SPIONs were about an order higher than the IC in serum from the control mouse. This means that, by using the bathophenanthroline-based (BPT-based) iron determination method, the IC background in the control mouse does not significantly affect the IC from injected SPIONs.

In Figure 5.3c, the normalized data showed that in PBS 1X both PEG-NPs (blue curve) and ZDS-NPs (pink curve) had narrow retention time distributions (RTDs) with peaks of ~27 min and ~35 min, respectively. This indicates that in PBS 1X both PEG-NPs and ZDS-NPs were nearly monodisperse. After the injection into the mouse, the RTD of PEG-NPs (black curve) retained its narrow distribution with a peak of ~27 min, indicating no change in the HD of PEG-

NPs. Meanwhile, after the injection into the mouse, the RTD of ZDS-NPs (cyan curve) slightly shifted to the left but retained a narrow distribution, showing a new peak of ~32 min. Compared to ZDS-NPs in PBS 1X with an original peak of ~35 min, this 3 min difference corresponds to a small HD increase of ~4 nm.[75] These data therefore suggest that, as expected the PEG-NPs, which is a well-established SPION platform for in vivo applications, have a minimal non-specific binding toward serum proteins in vivo in mice.[76] These data also demonstrate that only a low non-specific binding of ZDS-NPs was observed towards serum proteins in vivo in mice, and consequently ZDS-NPs are also suitable for in vivo applications. Moreover, small ZDS ligands have a significant size advantage (MW: ~300 g/mol) over PEG-lipid ligands (MW: ~2800 g/mol), which in turn guarantees a significantly reduced HD of ZDS-NPs compared to the HD of PEG-NPs.

5.4 Streptavidin-biotin labeling test

5.4.1 Design of streptavidin-biotin labeling test

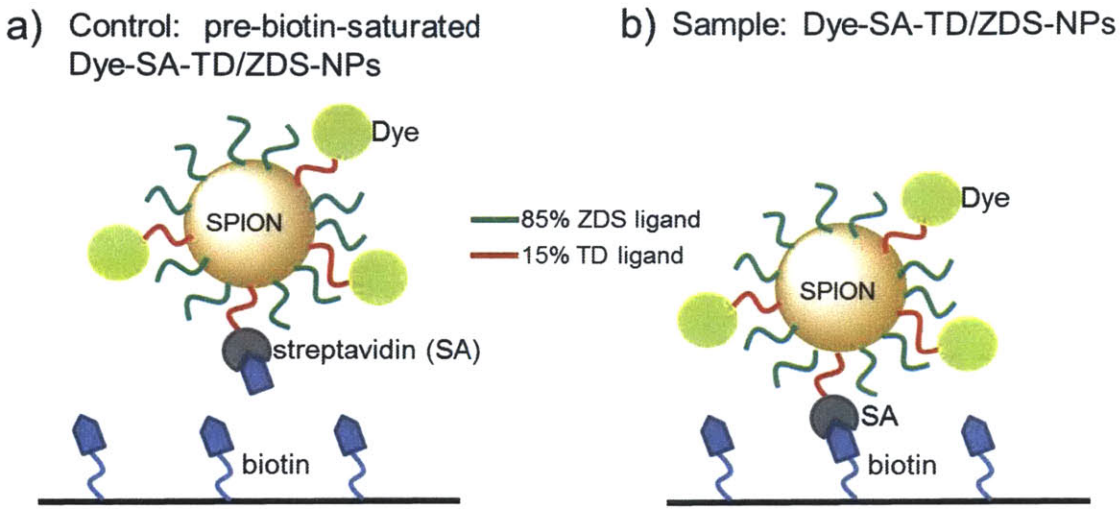

Figure 5.4 Schematic shows of a) the incubation of biotin-saturated dye/streptavidin functionalized SPIONs with a biotin-coated well on a plate and b) the incubation of dye/streptavidin functionalized SPIONs with a biotin-coated well on a plate. Adapted with permission from (Wei H.; et al. "Compact Zwitterion-Coated Iron Oxide Nanoparticles for Biological Applications" Nano Letters 2012, 12, 22). Copyright (2011) American Chemical Society.

In previous sections of Chapter 5, we have already shown that our SPIONs are stable in biological systems both in vitro and in vivo. In order to further show our SPIONs' potential in specific targeting and fluorescent imaging, the SPIONs were functionalized with fluorescent dyes and streptavidin, where the dyes provide detectable fluorescence and the streptavidin can specifically bind to biotin receptors. In this respect, the SPIONs were first treated by a ligand exchange with a mixture of 15% thiol-terminated catechol-derivative (TD) ligand and 85% zwitterionic dopamine sulfonate (ZDS) ligand (mol%). Next, as shown in Figure 5.4, the resulting TD and ZDS coated SPIONs (TD/ZDS-SPIONs, or TD/ZDS-NPs for simplicity) were

functionalized by Alexa Fluor® 488 maleimide dye (Dye) and streptavidin-maleimide (SA) through a standard thiol-maleimide conjugation method. Then the Dye and SA functionalized TD/ZDS-NPs (Dye-SA-TD/ZDS-NPs) were prepared into a control and a sample: in the control, Dye-SA-TD/ZDS-NPs were pre-saturated by biotin molecules so that SA lost their specific binding ability towards biotin receptors; in the sample, there was not such a pre-saturation process and Dye-SA-TD/ZDS-NPs were used as prepared. Finally, the pre-biotin-saturated Dye-SA-TD/ZDS-NPs (control) and normal Dye-SA-TD/ZDS-NPs (sample) were separately incubated with biotin-coated wells on a plate for 20 min before the NP solutions were discarded. Afterwards, the biotin-coated wells were washed by phosphate buffered saline 1X (PBS 1X) three times in order to remove unbound NPs before their fluorescent spectra were measured. More experimental details can be found in the supporting information of our publication.[53]

5.4.2 Biotin specific labeling using functionalized magnetic nanoparticles

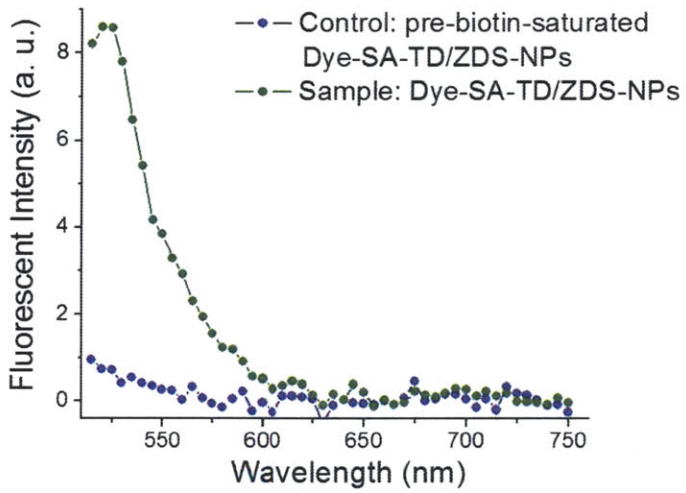

Figure 5.5 Fluorescent profiles of both control and sample biotin-coated wells, which were measure separately. Adapted with permission from (Wei H.; et al. "Compact Zwitterion-Coated Iron Oxide Nanoparticles for Biological Applications" Nano Letters 2012, 12, 22). Copyright (2011) American Chemical Society.

The Alexa Fluor® 488 maleimide dye (Dye) used for the functionalization of Dye-SA-TD/ZDS-NPs has an absorption peak of 488 nm and an emission peak of 520 nm. As shown in Figure 5.5, the specific binding ability of Dye-SA-TD/ZDS-NPs was determined by measuring the residual fluorescence intensity on both the control biotin-coated well and the sample biotin-coated well. We found that, at the Dye emission peak of 520 nm, the fluorescent intensity of Dye-SA-TD/ZDS-NPs (sample) was about an order higher than that of pre-biotin-saturated Dye-SA-TD/ZDS-NPs (control), indicating a successful specific labeling using Dye-SA-TD/ZDS-NPs. This data therefore suggests that our functionalized TD/ZDS-NPs may server as a specific labeling agent for targeting cell receptors in vitro.

6. Chapter 6: Magnetic resonance imaging using hydrophilic magnetic nanoparticles

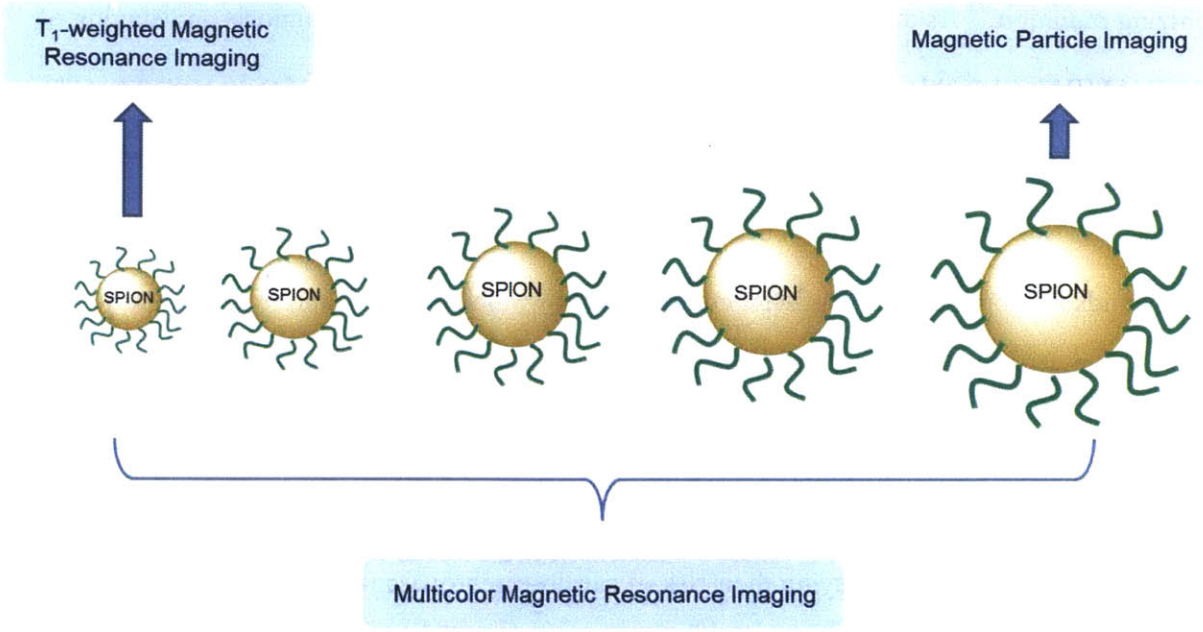

6.1 Introduction to magnetic resonance imaging

6.1.1 Contrast-enhanced magnetic resonance imaging

Medical imaging techniques have successfully provided the visual images of internal structures of a body that are beneath skins and bones over three billion studies until 2007,[77] greatly contributing to the diagnosis, monitoring, and treatment planning for patients. Dense structures of a body (e. g., bones) can be easily and clearly imaged by X-ray computed tomography (CT); however, it is usually difficult to obtain high-quality images of soft tissues and organs (e. g., brain, blood vessels, kidneys) using CT. Fortunately, nuclear magnetic resonance imaging (MRI) is able to excite and detect the water protons which are abundant in soft tissues and organs, hereby giving rise to more clear images than those from CT.

Moreover, MRI has the advantage of generating high-resolution images with no exposure to ionizing radiation.[78] As a result, the MRI technique is widely used for diagnosis and staging of disease; MRI is also able to investigate the anatomical and functional characteristics of healthy and diseased tissues.[21a, 79] In order to enhance the contrasts in MRI and to obtain clearer MR images, a variety of paramagnetic chemical compounds have been developed. These chemical compounds are routinely used as MRI contrast agents, which influence the relaxation time of protons.[80] For example, the diagnostic accuracy in conditions such as inflammation of the brain, spine, or soft tissues can be improved by contrast agents. Furthermore, MRI contrast agent plays an essential role in magnetic resonance angiography (MRA), in which the blood vessels in patients are visualized for studying their risk of cardio-cerebrovascular diseases. There are about 60 million MRI procedures that are performed each year globally, and it is estimated that ~35% of them are contrast-enhanced MRI, where contrast agents are introduced in the imaging procedures.[81]

As discussed before, MRI signals arise from the excitation and relaxation of protons in water molecules within the body. It is known that tissues such as fat, muscle, and bone have water protons that are different in terms of their concentrations and chemical environments; therefore, these differences in protons give rise to the contrast in MR images. Furthermore, in contrast-enhanced MRI those chemical compounds can further change the relaxation times of surrounding water protons (T_1 relaxation time and T_2 relaxation time) for MR contrast enhancement. The MRI contrast agents used today can be divided into two types: the first type is to decrease the T_1 relaxation time and to produce positive contrast (more bright signals) in MR images, while the second type is to decrease the T_2 relaxation time and to produce negative contrast (more dark signals) in MR images. In comparison, T_1–weighted MRI does not suffer from the artifacts seen

in T_2–weighted MRI that are caused by breathing or air/tissue boundaries.[31] Especially, in contrast-enhanced MRI, the bright signals from T_1 contrast agents, unlike T_2 contrast agents, are not obfuscated by bleeding or metal deposition. Therefore, currently radiologists widely prefer the use of T_1 contrast agents such as gadolinium based compounds.

6.1.2 Challenges in contrast-enhanced magnetic resonance imaging

Gadolinium based contrast agents (GBCA), which include nine U. S. Food and Drug Administration (FDA) approved compounds, are currently the most common MRI contrast agents used in the clinic.[82] The chemical structures of GBCA are generally Gadolinium (Gd) chelates, in which the paramagnetic Gd atoms are coordinated by organic ligands. These organic ligands play an essential role in the biochemical properties of GBCA and they also prevent tissues from directly interacting with Gd atoms, as free Gd ions are known to have toxicity issues and they are thought to interfere with cell membranes and intracellular enzymes.[83] Moreover, the small hydrodynamic diameters of Gd chelates further enable their rapid renal clearance. As a result, many GBCA have very short blood circulation times, but too short circulation times can sometimes limit the integration time and MR image quality.[21a] 99.97% of GBCA administered into the blood is eliminated through the kidneys for patients with normal renal functions, and 91-99% of the GBCA was found to be excreted within the first 24 hours (hrs) post-injection.[84] On the contrary, for patients with underlying renal insufficiency, the elimination rate of GBCA can be prolonged 20 times, which may lead to adverse effects. As a result, in 2007, the FDA requested GBCA manufacturers to show a black-box warning, which alerts their consumers to the risks related with GBCA.[85] For example, GBCA is contraindicated in patients with acute

kidney injuries as well as with stage 4 and 5 chronic kidney diseases (CKD); many hospitals have even put in strict pre-imaging guidelines for patients with stage 3 CKD.

Nephrogenic systemic fibrosis (NSF) is a rapidly progressive and untreatable disease. It causes both visceral and cutaneous fibrosis in patients with renal failures.[86] For patients afflicted with NSF, they usually suffer from pain, incapacitating contracture of ankles and hands, as well as paresthesia. A strong association has been established between the exposure to GBCA and the NSF in several retrospective studies, in which Gd is believed to possibly play a triggering role in the disease's development.[87,88] Therefore, hospitals worldwide have established screening policies in order to protect patients from developing NSF that may be caused by the use of GBCA in MRI procedures. The screening process includes the evaluation of kidney functions in vulnerable patients (such as patients over age 65 or patients with diabetes) followed by a risk-benefit analysis. Unfortunately, it is estimated that 26% of the population over age 60 has chronic kidney disease (CKD) according to the National Health and Nutrition Examination Survey.[89] Consequently, a large number of patients are currently not able to receive appropriate diagnostic contrast-enhanced MRI, and thus the development of non-toxic alternatives to GBCA may be meaningful to them.

Superparamagnetic iron oxide nanoparticles (SPIONs) are single-domain magnetic iron oxide particles with their sizes of a few nanometers to tens nanometers.[90] SPIONs (e.g., magnetite and maghemite) are known for their monodispersity in synthesis, superior stability, high saturation magnetization, and most importantly, well-defined nontoxicity towards living animals.[21] As a result, SPIONs have found their way into the clinic in the form of the FDA approved Feridex®, Resovist®, and Feraheme®.[44, 57] Presently, however, commercially available

SPION contrast agents are composed of polydisperse inorganic cores coated with a thick coating of hydrophilic polysaccharides (e.g., Dextran) resulting in particles with very large hydrodynamic diameters. Large SPIONs have a strong effect on the r_2 relaxivity, which scales with particle size, and, consequently, all of the commercially available SPIONs are used as T_2 dark contrast agents or iron supplements. Hence, there is still a great need of non-toxic small SPIONs for T_1-weighted MRI.

6.1.3 Prior art

The global contrast agent market has about $8.8 billion in 2009 and this number is expected to grow to about $13.7 billion in 2016.[81] Based on the price data from the Medicare Part B average sale of GBCA and the known fraction of contrast-enhanced MRI,[91] it is estimated that there are about 21 million contrast-enhanced MRI procedures per year with ~$50 per dose, leading to a total MRI contrast agent market of ~$1.0 billion/year globally.

In order to find other ways of removing Gadolinium Based Contrast Agents (GBCA) from the bloodstream of patients with kidney impairments, the manufacturers of GBCA have on-going phase IV clinical trials that study the effectiveness of hemodialysis in terms of removing GBCA post-injection. The research studies indeed showed that hemodialysis could be used to remove GBCA from the bloodstream; however, the elimination rate of GBCA by hemodialysis may be too slow to protect vulnerable patients from the onset of nephrogenic systemic fibrosis (NSF). For example, first, second and third hemodialysis sessions in one study were reported to eliminate averages of 73.8%, 92.4% and 98.9% of total GBCA, respectively.[84] It has been found that, in several other retrospective studies concerning the occurrence of NSF in vulnerable

patients, a significant portion of them still developed NSF even if they received hemodialysis sessions within 24 hrs of GBCA administration.[83]

There are several types of commercially developed SPIONs, including Resovist®, Feridex®, Feraheme®, Sinerem®, Supravist®, and Clariscan®. They have different sized inorganic cores and different ligand coatings and they have been studied in pre-clinical and clinical trials for T_1 and T_2 -weighted MRI.[92] These SPION-based MRI contrast agents are characterized by relatively large hydrodynamic diameters (HDs) from ~11 to >100 nm with broad size distributions, and thus they are usually cleared through the reticuloendothelial system. Because of their large inorganic core size and HD, they are not optimized for T_1-weighted MRI, yet better suited for T_2-weighted MRI. Among these commercially developed SPIONs, Resovist® and Feridex® have large HDs such as ~50 to ~200 nm and therefore they have generally been used as T_2 contrast agents. Feraheme®, Sinerem®, Supravist®, and Clariscan® have relatively smaller HDs such as ~11 to ~40 nm and thus they have been used as both T_1 and T_2 contrast agents. For example, Feridex® was approved by FDA as a T_2 contrast agent for MRI of liver, but its production and distribution were almost discontinued in 2011. Moreover, Feraheme® is approved by FDA for treating iron deficiency anemia currently. In contrast, Supravist® entered phase II clinical studies by Bayer Healthcare Pharmaceuticals but its development has ceased. Similarly, Sinerem® went to phase III clinical trials by Guerbet/AMAG Pharmaceuticals; nevertheless, its application for clinical approval to the European Medicines Agency (EMEA) was withdrawn. Finally, Clariscan® also went to phase III clinical trials by GE Healthcare yet its development has been discontinued too. In all the above commercial cases, the SPION contrast agents have large HDs

and they are better suited for T_2-weighted MRI - they could not compete with GBCA that generate positive contrasts in T_1-weighted MRI.

There are other academic research groups who are developing new SPION-based T_1 contrast agents. For example, in 2011, polyethylene glycol (PEG) coated SPIONs with ~15 nm HD were reported by Hyeon et al. from Seoul National University.[31] Moreover, in 2012, citrate-coated SPIONs with ~7 nm HD were reported by Taupitz et al. from Charité - Universitätsmedizin Berlin.[93] However, the HDs of these new SPION-based T_1 contrast agents are still larger than the 5.5 nm renal clearance HD threshold and therefore they can still exhibit clearance through the reticuloendothelial system.[94] Furthermore, the citrate-coated SPIONs are usually negatively charged, and it is known that negatively charged nanoparticles may show biological fouling, leading to an increased HD in vivo.

6.1.4 Motivation

SPIONs can be coated by hydrophilic ligands to be biologically compatible, showing HDs from a few to >100 nanometers (nm).[90] SPIONs are characterized by their high monodispersity, chemical and biological stability, and high saturation magnetization. More importantly, SPIONs are known to be generally non-toxic in vivo.[21] The current SPION-based contrast agents that are commercially available have polydisperse inorganic cores with thick ligand coatings such as polysaccharides (dextran). As discussed in 6.1.3, the resulting hydrophilic SPIONs show large HDs ranging from ~11nm to >100 nm. These large SPIONs generally have strong effects in terms of T_2 contrast (negative contrast), which scales with the size (both inorganic core and HD)

of SPIONs. Therefore, the majority of commercially available SPIONs are better suited for T_2-weighted MRI, and they are rarely used for routine MRI procedures in the clinic.

Large HD of SPIONs not only causes strong T_2 contrast but also hinders their renal clearance. Rapid renal clearance is important as it minimizes long-term exposure of body to large amounts of contrast agent needed for multiphase dynamic imaging (~0.1 mmol/Kg). Since unbound contrast agent is quickly removed, rapid renal clearance can also allow a more efficient specific targeting in vivo by using MRI. It has been demonstrated that hydrophilic nanoparticles with a HD no more than 5.5 nm can be excreted through the kidneys in mice, and a similar phenomenon is expected in humans.[94] Moreover, hydrophilic nanoparticles that are small enough are expected have effective extravasation from capillaries to surrounding tissues such as inflammation areas or tumor sites, which is similar to the pharmacokinetic properties of GBCA. Nevertheless, the current large SPIONs eliminate from the body through the reticuloendothelial system and they may rely on assistances from monocyte to extravasate. This process usually results in ineffective extracellular MRI contrast when compared to that of GBCA.

Consequently, a SPION-based non-toxic alternative to GBCA is in demand. This alternative should be exceedingly-small in HD in order to be used for T_1-weighted MRI and to have rapid renal clearance. We choose the term exceedingly-small to distinguish our new SPIONs from previous generations of SPIONs, ultra-small SPIONs, and so on. We will show below that our exceedingly-small SPIONs (ES-SPIONs) can be as small as ~5 nm in HD. Unlike previous generations of SPIONs, ES-SPIONs can have similar T_1 contrast and pharmacokinetic properties such as rapid renal clearance and extravasation when compared to those of GBCA.

6.2 Characterization of hydrophilic exceedingly-small magnetic nanoparticles

6.2.1 Magnetic properties of exceedingly-small magnetic nanoparticles

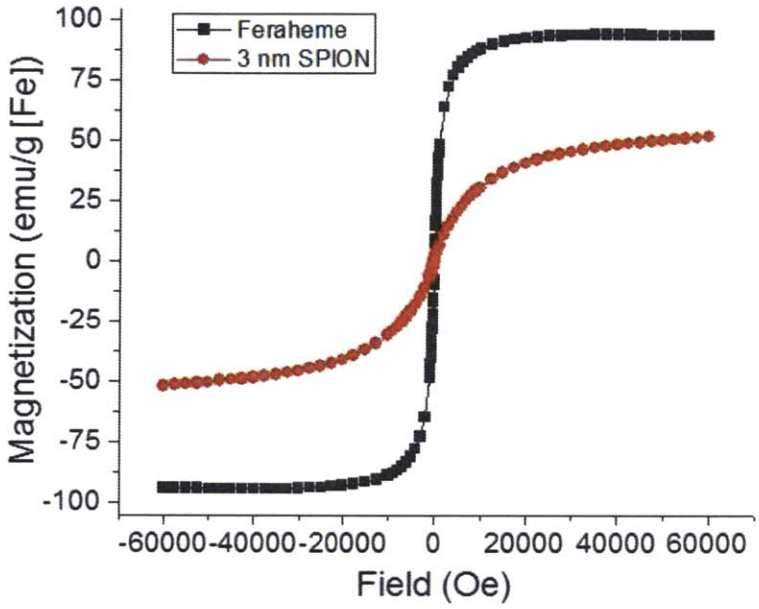

Figure 6.1 SQUID curves of 3 nm SPIONs and Feraheme® measured at room temperature

In order to characterize the magnetic behavior and saturation magnetization (M_s) of SPIONs, the SQUID curves of 3 nm hydrophobic SPIONs and Feraheme® were measured at room temperature (298 K) with the magnetic field strength H ranging from -6000- to 60000 Oe (i. e. -6 to 6 Tesla), as shown in Figure 6.1.[95] After determining the mass of iron in the 3 nm hydrophobic SPIONs, the M_s of 3 nm hydrophobic SPIONs at room temperature was found to be 52 emu/g [Fe], which is about a half of the bulk value for maghemite of 106 emu/g [Fe].[63] Moreover, the superparamagnetism of 3 nm hydrophobic SPIONs at room temperature is confirmed by the absence of hysteresis loops near zero magnetic fields.[96] More importantly,

Figure 6.1 shows that the magnetization of Feraheme® rapidly approaches its maximum (94 emu/g [Fe]) when the magnetic field $|H| > 0.5$ T while the magnetization of 3 nm hydrophobic SPIONs does not reach its maximum even at $|H| = 6$ T. This phenomenon indicates that the magnetic field required to saturate the magnetization of Feraheme® is ~0.5 T; however, the magnetic field required to saturate the magnetization of 3 nm hydrophobic SPIONs is beyond 6 T. This is due to the size difference of SPIONs and their corresponding magnetic anisotropy energy difference, and this relationship between inorganic core size and H is consistent with literatures.[31] The 3 nm SPIONs with a high saturating magnetic field are desired for T_1-weighted MR contrast agents, as this type of SPIONs will have a lower magnetization at clinical magnetic field strength of 1.5-3 Tesla and a correspondingly high T_1 contrast.

6.2.2 Hydrodynamic diameter of exceedingly-small magnetic nanoparticles

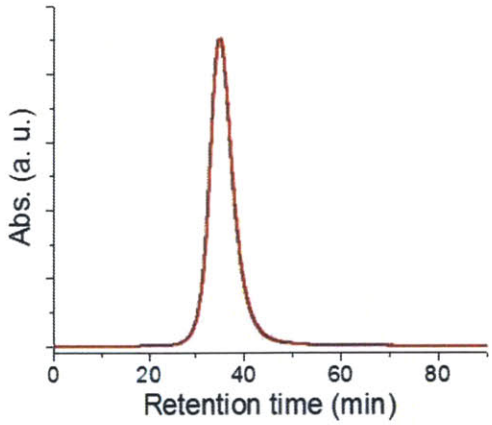

Figure 6.2 Size-exclusion HPLC of exceedingly-small SPIONs (ES-SPIONs)

To stabilize the as-synthesized 3 nm SPIONs in aqueous media for magnetic resonance imaging, ligand exchange is needed. To this end, zwitterionic dopamine sulfonate (ZDS) - was used to coated 3 nm SPIONs. After the 3 nm SPIONs were ligand-exchanged from native oleic acid to ZDS, size-exclusion high-performance liquid chromatography (HPLC) measurement revealed that the ZDS coated SPIONs (ZDS-SPIONs) in phosphate buffed saline (PBS) have narrow size distributions with hydrodynamic diameters (HD) of ~ 5 nm at pH = 7.4. This result confirms that the ZDS ligand only contributes ~1 nm to the overall radius, and this size change induced by the ZDS ligand and their stability are consistent with our prior study.[53] More importantly, the ZDS-SPIONs have a HD smaller than 5.5 nm, which is the HD threshold for efficient renal clearance.[97]

6.3 T_1-weighted magnetic resonance imaging using exceedingly-small magnetic nanoparticles

In collaboration with Harald Ittrich group at University Medical Center Hamburg-Eppendorf

6.3.1 T_1-weighted magnetic resonance imaging of mice

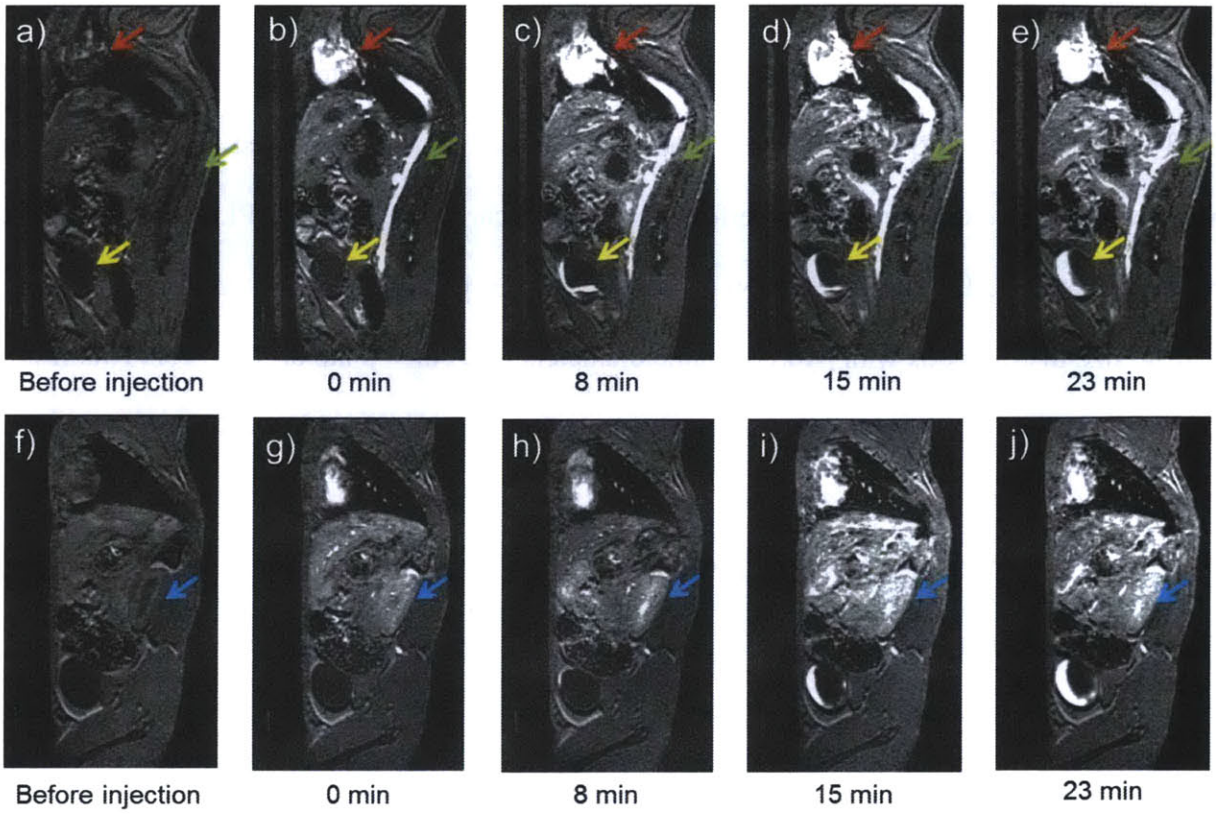

Figure 6.3 T_1-weighted MR images of a mouse injected with exceedingly-small SPIONs (ES-SPIONs). Time points beneath each image: the time after ES-SPIONs injection. a)-e) one sagittal slice showing the heart (red arrow), the artery (green arrow), and the bladder (yellow arrow); and f)-j) one sagittal slice showing the kidney (blue arrow)

By using a 4.7 Tesla MRI scanner, the T_1-weighted MR images of mice injected with exceedingly-small SPIONs (ES-SPIONs) are shown in Figure 6.3. Figure 6.3a shows that, before the injection of ES-SPIONs, the heart (red arrow), the artery (green arrow), and the bladder (yellow arrow) of mice did not have positive contrasts. Figure 6.3b shows that, after the injection of ES-SPIONs, the heart and the artery of mice immediately displayed highly positive contrasts. Later on, Figure 6.3c shows that, at 8 min after the injection of ES-SPIONs, the bladder of mice started to show positive contrasts, indicating an excretion of urine containing ES-SPIONs. With

the increase of time post-injection, Figure 6.3d-e show that positive contrast region of the bladder became larger, suggesting an accumulation of urine with ES-SPIONs.

At a different sagittal slice of mice, Figure 6.3f shows that the kidney (blue arrow) of mice did not have positive contrasts either. After the injection of ES-SPIONs, the kidney of mice immediately displayed positive contrasts. With the increase of time post-injection, Figure 6.3g-j demonstrated an increment of positive contrasts in the kidney.

These results suggest that, in addition to having a high T_1 contrast, our ES-SPIONs have rapid renal clearance and thus they may minimize the long-term exposure of large amounts of contrast agents (approximately 0.1mmol/Kg), which are required in multiphase dynamic imaging, to human bodies. The rapid renal clearance also enables the in vivo specific targeting of ES-SPIONs because the unbound contrast agents will be removed quickly.

6.3.2 T_1-weighted magnetic resonance imaging of rats

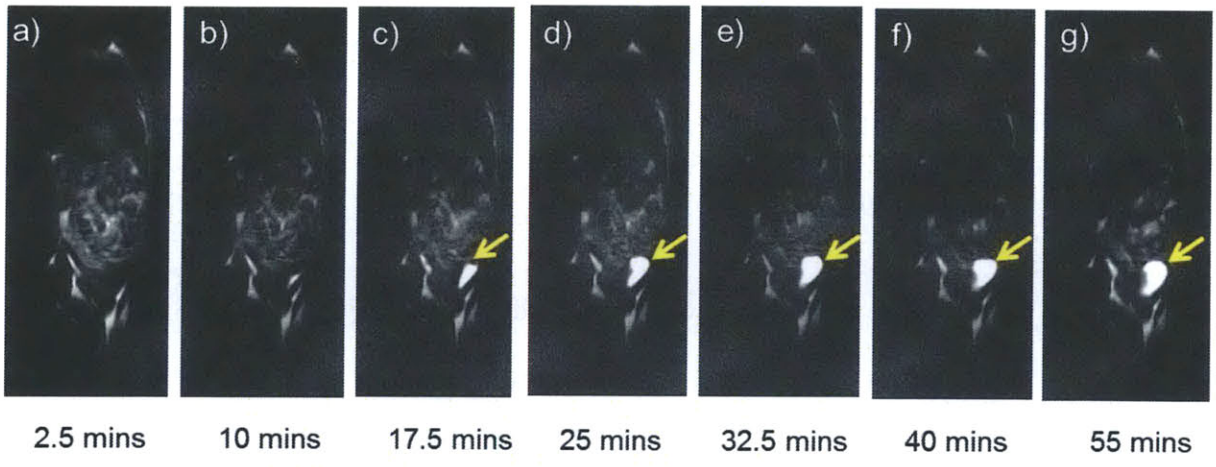

Figure 6.4 a)-g) T_1-weighted MR images of a rat injected with exceedingly-small SPIONs (ES-SPIONs). Time points beneath each image: the time after ES-SPIONs injection.

A 9.4 Tesla MRI scanner was used to study a rat injected with exceedingly-small SPIONs (ES-SPIONs). As shown in Figure 6.4, the ES-SPIONs were first circulating in the rat blood vessels at 2.5 and 10 mins post-injection. Beginning from 17.5 mins post-injection, ES-SPIONs started to accumulate in urine of the bladder in rat, showing high positive contrasts. This result confirms the high T_1 contrast and rapid renal clearance of ES-SPIONs that were observed in mice MRI scans.

6.3.3 Visualization of renal excretion of exceedingly-small magnetic nanoparticles

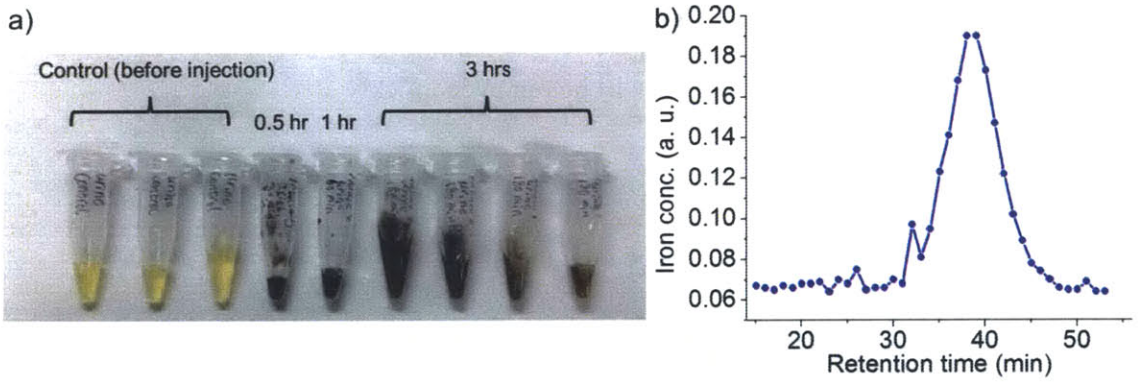

Figure 6.5 a) Urines from mice taken at different time points showing renal clearance of exceedingly-small SPIONs (ES-SPIONs) in vivo, and b) a size-exclusion Gel Filtration chromatogram of urine@1 hr

In order to visualize the renal clearance, our exceedingly-small SPIONs (ES-SPIONs) were intravenously injected into mice and their urines were collected at different time points, separately. Figure 6.5a shows that the mice urine without ES-SPIONs injection retained an original pale-yellow color; in contrast, after 0.5, 1, and 3 hrs post ES-SPIONs injection, mice urines all became black (the color of ES-SPIONs and their ZDS ligand coatings), showing a

remarkable renal clearance. In Figure 6.5b, the existence of ES-SPIONs in mice urine was further confirmed by fractionizing on the mice urine @ 1 hr using gel-filtration chromatography (GFC) with a size-exclusion column, followed by iron determination on each fraction using bathophenanthroline. We can see that, in Figure 6.5b, ES-SPIONs in urine @ 1hr have a retention time of 38 min, corresponding to a hydrodynamic diameter (HD) of ~4 nm. This result indicates that the observed black color is indeed from ES-SPIONs and the HD of injected ES-SPIONs is almost not affected in vivo in mice.

6.4 T_1-weighted magnetic resonance angiography using exceedingly-small magnetic nanoparticles

6.4.1 T_1-weighted magnetic resonance angiography of mice

In collaboration with Harald Ittrich group at University Medical Center Hamburg-Eppendorf

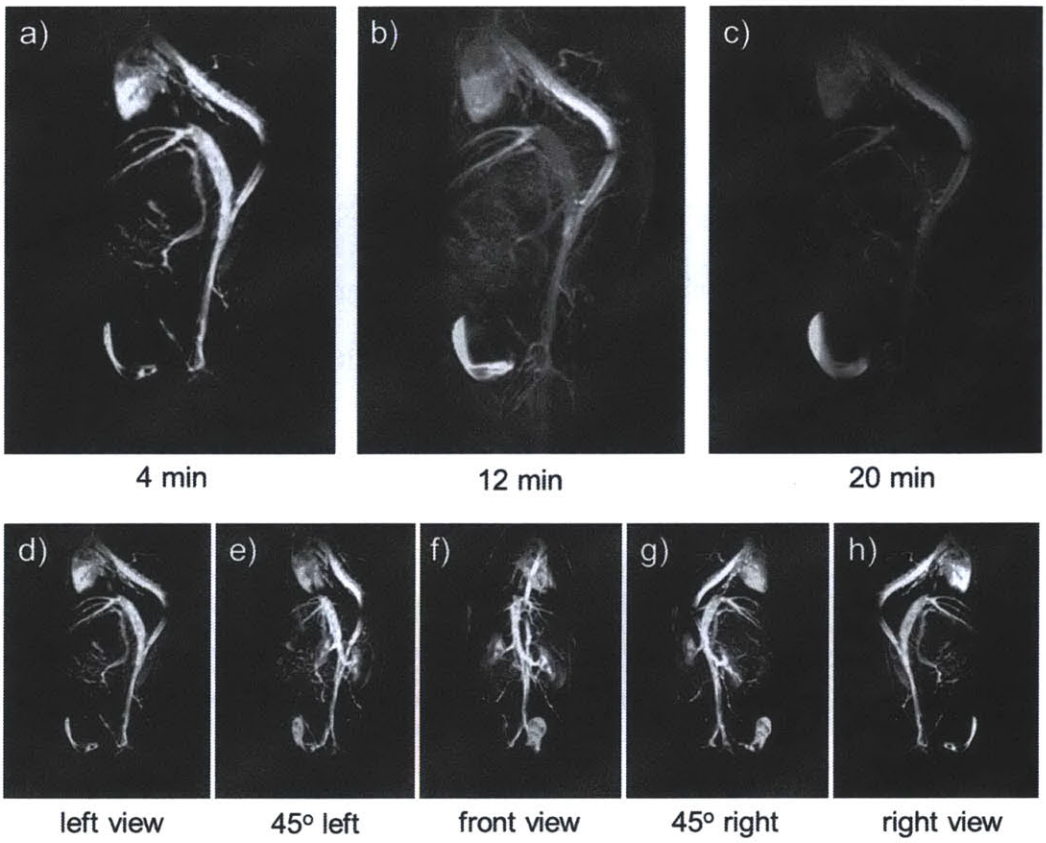

Figure 6.6 a)-c) T_1-weighted magnetic resonance angiography (MRA) of mice injected with exceedingly-small SPIONs (ES-SPIONs); time points beneath each image: the time after ES-SPIONs injection. d)-h) five different perspectives of MRA of mice

T_1-weighted magnetic resonance angiography (MRA) is widely used for studying human arteries, including but not limit to cerebral arteries, the aorta with its branches, and the arteries in the kidneys as well as in the lower limbs.[98] MRA has shown to be non-invasive with ionizing radiation and contrast agent toxicity reductions compared to CT angiography and invasive catheter angiography.

Figure 6.6a-c show the MRA of mice injected with ES-SPIONs. In addition to high T_1 contrasts, the blood vessels of mice in our MRA study can be imaged with a high resolution of

~0.2 mm. As shown in Figure 6.6a-c, with the increase of time post injection, the positive contrasts in the heart and arties darkened while the positive contrasts in the bladder brightened, indicating that the positive contrasts given by ES-SPIONs migrated from the circulatory system to the excretory system. This is in accordance with our previous discovery of ES-SPIONs being cleared through kidney. More interestingly, Figure 6.6b shows that, at 12 min, our ES-SPIONs may have entered the extravascular tissues of mice. This possible intravenous extravasation of ES-SPIONs is similar to that of Gadolinium based contrast agents (GBCA). Furthermore, this MRA using ES-SPIONs can be done in three-dimensional perspectives, as shown in Figure 6.6d-h. These results suggest that the ES-SPIONs can have the same performance as GBCA in terms of MRA and extravasation, making ES-SPIONs a promising non-toxic alternative to GBCA in studying human arteries.

6.4.2 T_1 contrast power of exceedingly-small magnetic nanoparticles

In collaboration with Michael Cima group at the Massachusetts Institute of Technology

	r_1 ($s^{-1}mM^{-1}$)	r_2 ($s^{-1}mM^{-1}$)	r_2/r_1
ES-SPIONs*	2.4	3.7	1.5
Gd-DTPA* (Magnevist®)	5.0	5.7	1.1

* measured at 0.5 T

	Core (nm)	HD (nm)	r_1 ($s^{-1}mM^{-1}$)	r_2 ($s^{-1}mM^{-1}$)	r_2/r_1
ES-SPIONs*	3	5	2.4	3.7	1.5
Taupitz group's SPIONs***	4	7	15	32	2.1
Hyeon group's SPIONs**	3	15	4.77	29.2	6.1
Feraheme® *	7	20-30	38	83	2.2

* measured at 0.5 T; ** measured at 3 T; *** measured at 1.5 T

Figure 6.7 Comparison of T_1 contrast power among different contrast agents. The ratio r_2/r_1 is the figure of merit.

The relaxivity r equals to $\frac{1}{T*[M]}$, where T is the T_1 or T_2 relaxation time and [M] is the concentration of metal ions. Since every contrast agent will enhance both T_1 and T_2 contrasts, the ratio of r_2/r_1 is used as a figure of merit to evaluate an agent's T_1 or T_2 contrast ability; a low (high) r_2/r_1 is good for T_1 (T_2) MR imaging. This r_2/r_1 ratio also depends on the field strength used in the experiment. The relaxivity data of Feraheme®, [99] other reported SPIONs from Hyeon's group,[31] and Taupitz's group[93] as well as Magnevist®[21a, 100] are taken from published references.

Our exceedingly-small SPIONs (ES-SPIONs) with a ~3 nm inorganic core and a ~5 nm hydrodynamic diameter achieved an r_2/r_1 ratio as low as 1.5, which matches the strongest T_1 SPION-based contrast agents reported so far.[82d,82e,31,101] This low r_2/r_1 ratio is even comparable with Gadolinium based contrast agents (GBCA) such as Magnevist® and PGP/dextran-K01.[23a, 103]

6.5 Multicolor magnetic resonance imaging

In collaboration with Alan Jasanoff group at the Massachusetts Institute of Technology

6.5.1 Introduction

Multicolor magnetic resonance imaging (MRI) is a novel technique that assigns different colors to SPIONs based on their distinct r_2/r_1 ratios. Multicolor MRI is unlike T_1-weighted MRI, where a low r_2/r_1 ratio is preferred in the clinic and images are usually black and white; on the contrary, in multicolor MRI, the SPIONs with different r_2/r_1 ratios are preferred for biomedical research in the laboratory. These SPIONs with different r_2/r_1 ratios can serve as mimics to multicolor fluorescent quantum dots, enabling multiplexing SPION-based imaging. For example, two types of SPIONs can be functionalized with two types of antibodies, respectively; then these two types of functionalized SPIONs can label different biological receptors in mice and display different colors on receptors upon the use of multicolor MRI technique. Researchers have shown in vitro multicolor MRI using Gadolinium based contrast agents (GBCA) with different r_2/r_1 ratios.[102]

6.5.2 Hydrophilic magnetic nanoparticles with tunable r_2/r_1 ratios

	Core (nm)	HD (nm)	r_1 ($s^{-1}mM^{-1}$)	r_2 ($s^{-1}mM^{-1}$)	r_2/r_1
Feraheme®*	3-10	16	3.1	68	22
ZDS-coated Fe_2O_3 NPs*	7	12	3.4	60	18
ZDS-coated Fe_2O_3 NPs*	6	9	2.9	51	18
ZDS-coated Fe_2O_3 NPs*	4	6	2.0	32	16
DS-coated Fe_2O_3 NPs*	2.5	4	1.3	17	13
ZDS-coated Fe_2O_3 NPs*	3	5	1.5	17	11

* Measured at 7 Tesla

Figure 6.8 SPIONs with different r_2/r_1 ratios. Inorganic core diameters were determined by transmission electron microscopy; hydrodynamic diameters (HD) were determined by size-exclusion HPLC; relaxivities r_2 and r_1 were determined by a 7 Tesla MRI scanner.

As discussed before, the key to multicolor MRI is the preparation of SPIONs with different r_2/r_1 ratios. Figure 6.8 shows that we can achieve different r_2/r_1 ratios by changing the inorganic core diameter and hydrodynamic diameter (HD) of SPIONs, in which the relaxivities were measured by a 7 Tesla MRI scanner. As shown in Figure 6.8, the r_2/r_1 ratios of our zwitterionic dopamine sulfonate (ZDS) or dopamine sulfonate (DS) coated SPIONs can be tuned between 11 and 18 at 7 Tesla. Moreover, the r_2/r_1 ratio of commercially available Feraheme® is 22 at 7 Tesla. These results suggest that our hydrophilic SPIONs have a tunable range of r_2/r_1 ratios and several types of hydrophilic SPION can be rationally synthesized for multicolor MRI.

6.5.3 In vitro multicolor magnetic resonance imaging

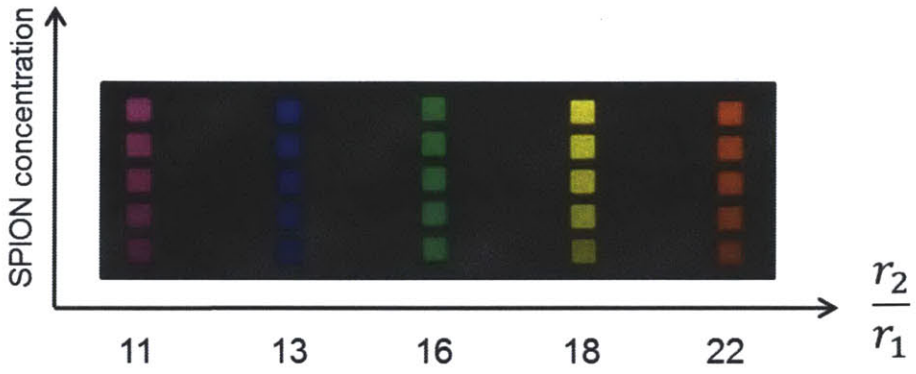

Figure 6.9 Multicolor MRI using SPIONs with different r_2/r_1 ratios

In Figure 6.9, the hydrophilic SPIONs with five distinct r_2/r_1 ratios, including our as-prepared SPIONs and Feraheme®, are shown via multicolor MRI using a 7 Tesla scanner. SPIONs with r_2/r_1 ratios of 11, 13, 16, 18, and 22 were assigned with purple, blue, green, yellow, and red colors, respectively. Figure 6.9 also shows that the signal intensity of multicolor MRI was proportional to the concentration of SPIONs. These results indicate that our hydrophilic SPIONs and commercially available hydrophilic SPIONs are promising for multicolor MRI applications.

6.6 Magnetic particle imaging

6.6.1 Introduction

Magnetic particle imaging (MPI) is a novel and revolutionary pre-clinical three-dimensional imaging technique, in which the MPI signals only come from the fast and non-linear magnetization response of SPIONs.[11] First, MPI is background-free and quantitative towards SPIONs for the reason that animal tissues, which are generally diamagnetic, have zero MPI signal at low frequency magnetic fields used for in vivo imaging.[12] Compared to magnetic resonance imaging (MRI), MPI has ~100 times higher sensitivity up to 10^{-9} mol/L. Moreover, MPI has the advantage of high temporal resolution that enables real time imaging. Furthermore, at the same spatial resolution of positron emission tomography (PET), MPI can be ~1000 times faster.[103]

Theoretical calculations have shown that the optimal inorganic diameter of SPIONs for MPI is ~30-40 nm with a very high saturation magnetization.[11] However, the synthesis of high-quality single domain SPIONs with an inorganic diameter larger than 25 nm has not been reported so far. For example, Resovist®, which is currently used as a MPI contrast agent,[12] consists of SPIONs with ~4 nm inorganic diameter.[92] The large hydrodynamic diameter of Resovist® (50-100 nm) and other iron oxide nanoparticles[104] may be attributed to the formation of nanoclusters which can be revealed by transmission electron microscopy. Therefore, the synthesis of >25 nm and highly magnetic SPIONs is a demanding challenge for successful MPI application at the moment.

6.6.2 SQUID measurements of large-sized magnetic nanoparticles

In Figure 2.12, we have shown the successful synthesis of large SPIONs with an inorganic diameter of ~35 nm. In order to study the magnetic behaviors and saturation magnetization (M_s) of the large SPIONs, superconducting quantum interference device (SQUID) measurements were performed, as shown below.

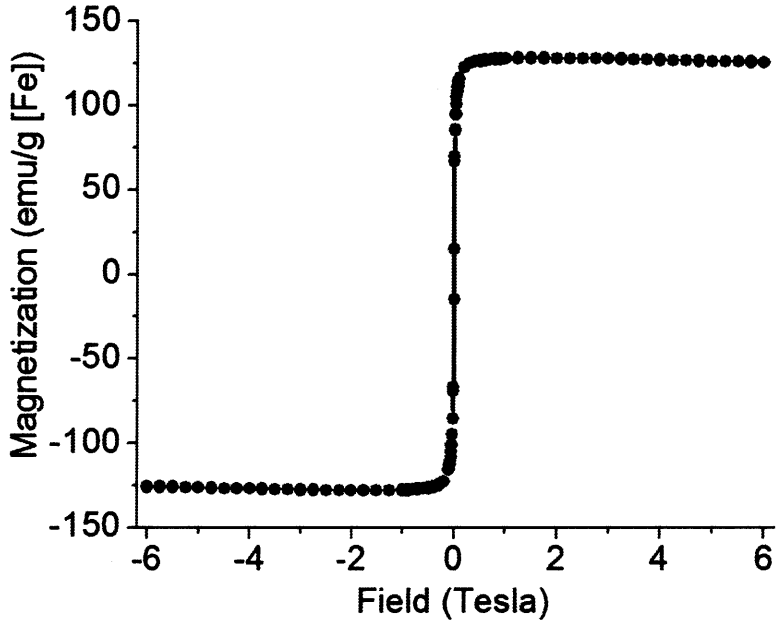

Figure 6.10 SQUID curve of ~35 nm SPIONs at 298 K

In Figure 6.10, SQUID measurements were done with the large SPIONs with an inorganic diameter of ~35 nm at 298 K with magnetic fields ranging from -6 to 6 Tesla (i. e. -60000 to 60000 Oe). There is not a noticeable hysteresis loop, indicating that these ~35 nm SPIONs are almost superparamagnetic. Most importantly, these ~35 nm SPIONs have a M_s of 126 emu/g [Fe], which is close to the bulk M_s value of magnetite (127 emu/g [Fe]). Therefore, these ~35 nm SPIONs may present the most magnetic SPIONs that are made of magnetite.

6.6.3 Silica-coated hydrophilic magnetic nanoparticles

Further biomedical MPI application of these ~35 nm SPIONs require them to be hydrophilic. However, the water-solubilization process of ~35 nm SPIONs is different from the method used in Chapter 4, here a hydrophilic silica shell was deposited on these ~35 nm SPIONs. This is because experiments have shown that 2-[2-(2-methoxyethoxy)ethoxy]acetic acid (MEAA) coated large SPIONs was not able to be well dispersed in methanol. Therefore, it was difficult to accomplish the ligand exchange of native oleic acid on large SPIONs with zwitterionic dopamine sulfonate.

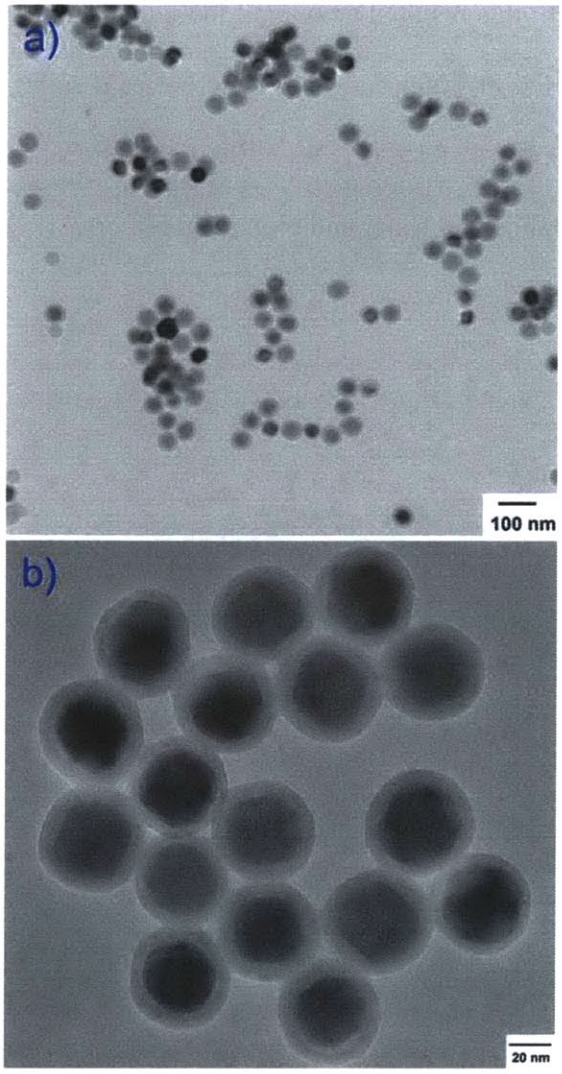

Figure 6.11 Transmission electron microscopy (TEM) images of silica coated ~35 nm SPIONs

The silica shell was deposited onto SPIONs in a cyclohexane solution containing Igepal CO-520, tetraethyl orthosilicate, and ammonium hydroxide. The reaction was allowed to proceed at room temperature before the silica coated SPIONs were purified by centrifugation and magnetic separation. In Figure 6.11a and b, transmission electron microscopy (TEM) images demonstrate that the silica coated SPIONs were still monodisperse, with a ~35 nm inorganic iron oxide core

and ~7.5 nm silica shell; this resulted an overall inorganic diameter of ~50 nm. The silica coated SPIONs can be dispersed in water and phosphate buffered saline (PBS) 1X. Further coating of methoxy polyethylene glycol silane (M. W. ~5000) onto the silica coated SPIONs was found be able to increase their stability in water and biological buffers.

7. Chapter 7: Biography

7.1 Publications from 2009 to 2014

1. Wei H, Insin N, Lee J, Han HS, Cordero JM, Liu W, Bawendi MG. "Compact Zwitterion-Coated Iron Oxide Nanoparticles for Biological Applications." *Nano Letters.* **2012**, 12, 22-25.

2. Wei H, Bruns OT, Chen O, Bawendi MG. "Compact zwitterion-coated iron oxide nanoparticles for in vitro and in vivo imaging." *Integrative Biology.* **2013**, 5, 108-114.

3. Chen O, Zhao J, Chauhan VP, Cui J, Wong C, Harris DK, Wei H, Han H-S, Fukumura D, Jain RK, Bawendi MG. "Compact high-quality CdSe-CdS core-shell nanocrystals with narrow emission linewidths and suppressed blinking." *Nature Materials.* **2013**, 12, 445-451.

4. Chen O, Wei H, Maurice A, Bawendi MG, Reiss P. Pure colors from core-shell quantum dots. *MRS Bulletin.* **2013**, 38, 696-702.

5. Chen O, Riedemann L, Etoc F, Herrmann H, Coppey M, Barch M, Farrar CT, Zhao J, Bruns OT, Wei H, Guo P, Cui J, Jensen R, Chen Y, Harris DK, Cordero JM, Wang ZW, Jasanoff AP, Fukumura D, Reimer R, Dahan M, Jain RK, Bawendi MG "Magneto-Fluorescent Core-Shell Supernanoparticles" *Nature Communications.* Accepted, **2014**

6. Wei H, Bawendi MG, et al. "Achieving Positive MRI with High Contrasts and Rapid Renal Clearances using Exceedingly-small Iron Oxide Nanoparticles" *Manuscript in preparation,* **2014**

7.2 Presentations from 2009 to 2014

1. Wei H, Bawendi MG, et al. *Cancer Nanotechnology - Gordon Research Conferences.* Waterville, ME, July 2011 (poster)

2. Wei H, Bawendi MG, et al. *Materials Research Society meetings.* Boston, MA, November 2012 (poster)

3. Wei H, Bawendi MG, et al. *GlaxoSmithkline Symposium.* Boston, MA, May 2013 (poster)

4. Wei H, Bawendi MG, et al. *Clusters, Nanocrystals & Nanostructures - Gordon Research Conferences.* South Hadley, MA, August 2013 (poster)

5. Wei H, Bawendi MG, et al. *Materials Research Society meetings.* San Francisco, CA, April 2014 (oral presentation)

7.3 Patents and disclosures from 2009 to 2014

1. Bawendi MG, Wei H, Insin N, Han HS "Compact nanoparticles for biological applications", WO 2013090601 A3

2. Wei H, Bruns OT, Chen O, Bawendi MG "Nanoparticles for MRI and MPI applications" disclosure with the Technology Licensing Office at the Massachusetts Institute of Technology (case 16726)

8. Chapter 8: Acknowledgements

First of all, I would like to thank my research advisor and thesis supervisor - Professor Moungi Bawendi - for his enlightening guidance and highly useful advices in my whole Ph. D. study process. His knowledge and instructions are valuable and strongly influence the directions and scientific approaches of my research projects. I am grateful for his insight to the blueprint of iron oxide nanoparticle projects ranging from synthesis to clinical applications. I also would like to thank him for the financial support to my Ph. D. study.

Moreover, I would like to thank my Ph. D. thesis committee chair - Professor Keith Nelson - for his helpful advices and other perspectives to my research projects as always. I am grateful for his understanding and encouragement. I also appreciate the research knowledge that he shared with me during our annual meetings.

I also would like to thank my Ph. D. thesis committee member - Professor Robert Griffin - for his good suggestions to my research projects as always. Professor Griffin taught me Quantum Mechanics at the beginning of my Ph. D. study, and he suggested good books of magnetic resonance imaging to me. I am also grateful for his prompt responses to my questions.

I would like to thank Professor Alan Jasanoff and Dr. Harald Ittrich for their kind help to my magnetic resonance imaging studies.

I want to thank Ms. Li Miao for her great help and encouragement to my Ph. D. study. My Ph. D. study has gone more smoothly with her supports.

I also want to thank Dr. Numpon Insin, Dr. Oliver Bruns, Dr. Ou Chen, Dr. Jie Bao, Dr. Jongnam Park, Dr. Wenhao Liu, Mr. Jose Cordero, Mr. Daniel Montana, Ms. Yue Chen as well as many labmates from the Bawendi research group, Dr. Mariya Barch, and Ms. Agata Wisniowska, for many research collaborations and fruitful discussions with them.

I am thankful to my whole family members, who always support me. I want to thank Robert T. Haslam presidential fellowship from the Massachusetts Institute of Technology.

I thank Dr. Yong Zhang for his assistance with transmission electron microscopy and Dr. Shaoyan Chu for his help with superconducting quantum interference device.

9. Chapter 9: Bibliographic references

1. Hyeon, T.; Lee, S. S.; Park, J.; Chung, Y.; Bin Na, H., Synthesis of highly crystalline and monodisperse maghemite nanocrystallites without a size-selection process. *J Am Chem Soc* **2001,** *123* (51), 12798-12801.
2. Sun, S. H.; Zeng, H., Size-controlled synthesis of magnetite nanoparticles. *J Am Chem Soc* **2002,** *124* (28), 8204-8205.
3. Lee, J. H.; Huh, Y. M.; Jun, Y.; Seo, J.; Jang, J.; Song, H. T.; Kim, S.; Cho, E. J.; Yoon, H. G.; Suh, J. S.; Cheon, J., Artificially engineered magnetic nanoparticles for ultra-sensitive molecular imaging. *Nature Medicine* **2007,** *13* (1), 95-99.
4. Kang, E.; Park, J.; Hwang, Y.; Kang, M.; Park, J. G.; Hyeon, T., Direct synthesis of highly crystalline and monodisperse manganese ferrite nanocrystals. *J Phys Chem B* **2004,** *108* (37), 13932-13935.
5. Wang, J. Y.; Ren, F. L.; Yi, R.; Yan, A. G.; Qiu, G. Z.; Liu, X. H., Solvothermal synthesis and magnetic properties of size-controlled nickel ferrite nanoparticles. *J Alloy Compd* **2009,** *479* (1-2), 791-796.
6. Sun, S. H.; Murray, C. B.; Weller, D.; Folks, L.; Moser, A., Monodisperse FePt nanoparticles and ferromagnetic FePt nanocrystal superlattices. *Science* **2000,** *287* (5460), 1989-1992.
7. Sun, X. C.; Jia, Z. Y.; Huang, Y. H.; Harrell, J. W.; Nikles, D. E.; Sun, K.; Wang, L. M., Synthesis and magnetic properties of CoPt nanoparticles. *J Appl Phys* **2004,** *95* (11), 6747-6749.
8. Yoon, T. J.; Lee, H.; Shao, H. L.; Weissleder, R., Highly Magnetic Core-Shell Nanoparticles with a Unique Magnetization Mechanism. *Angew Chem Int Edit* **2011,** *50* (20), 4663-4666.
9. Kobayashi, Y.; Horie, M.; Konno, M.; Rodriguez-Gonzalez, B.; Liz-Marzan, L. M., Preparation and properties of silica-coated cobalt nanoparticles. *J Phys Chem B* **2003,** *107* (30), 7420-7425.
10. Gupta, A. K.; Gupta, M., Synthesis and surface engineering of iron oxide nanoparticles for biomedical applications. *Biomaterials* **2005,** *26* (18), 3995-4021.
11. Gleich, B.; Weizenecker, R., Tomographic imaging using the nonlinear response of magnetic particles. *Nature* **2005,** *435* (7046), 1214-1217.
12. Goodwill, P. W.; Saritas, E. U.; Croft, L. R.; Kim, T. N.; Krishnan, K. M.; Schaffer, D. V.; Conolly, S. M., X-Space MPI: Magnetic Nanoparticles for Safe Medical Imaging. *Adv Mater* **2012,** *24* (28), 3870-3877.
13. (a) Park, K.; Lee, S.; Kang, E.; Kim, K.; Choi, K.; Kwon, I. C., New Generation of Multifunctional Nanoparticles for Cancer Imaging and Therapy. *Advanced Functional Materials* **2009,** *19* (10), 1553-1566; (b) Tartaj, P.; Morales, M. D.; Veintemillas-Verdaguer, S.; Gonzalez-Carreno, T.; Serna, C. J., The preparation of magnetic nanoparticles for applications in biomedicine. *Journal of Physics D-Applied Physics* **2003,** *36* (13), R182-R197.
14. Pankhurst, Q. A.; Connolly, J.; Jones, S. K.; Dobson, J., Applications of magnetic nanoparticles in biomedicine. *Journal of Physics D-Applied Physics* **2003,** *36* (13), R167-R181.
15. Jordan, A.; Scholz, R.; Wust, P.; Fahling, H.; Felix, R., Magnetic fluid hyperthermia (MFH): Cancer treatment with AC magnetic field induced excitation of biocompatible superparamagnetic nanoparticles. *J Magn Magn Mater* **1999,** *201*, 413-419.
16. (a) Bialas, I.; Bessell, E. M.; Sokal, M.; Slack, R., A Prospective-Study of Urinary-Tract Infection during Pelvic Radiotherapy. *Radiotherapy and Oncology* **1989,** *16* (4), 305-309; (b) Groopman, J. E.; Itri, L. M., Chemotherapy-induced anemia in adults: Incidence and treatment. *Journal of the National Cancer Institute* **1999,** *91* (19), 1616-1634.

17. Lee, J. H.; Jang, J. T.; Choi, J. S.; Moon, S. H.; Noh, S. H.; Kim, J. W.; Kim, J. G.; Kim, I. S.; Park, K. I.; Cheon, J., Exchange-coupled magnetic nanoparticles for efficient heat induction. *Nature Nanotechnology* **2011,** *6* (7), 418-422.
18. Thiesen, B.; Jordan, A., Clinical applications of magnetic nanoparticles for hyperthermia. *Int J Hyperther* **2008,** *24* (6), 467-474.
19. Falk, M. H.; Issels, R. D., Hyperthermia in oncology. *Int J Hyperther* **2001,** *17* (1), 1-18.
20. Lu, M.; Cohen, M. H.; Rieves, D.; Pazdur, R., FDA report: Ferumoxytol for intravenous iron therapy in adult patients with chronic kidney disease. *Am J Hematol* **2010,** *85* (5), 315-319.
21. (a) Na, H. B.; Song, I. C.; Hyeon, T., *Adv. Mater.* **2009,** *21;* (b) Latham A. H.; Williams, M. E., *Accounts Chem Res* **2008,** *41.*
22. Rao, C. N. R.; Matte, H. S. S. R.; Voggu, R.; Govindaraj, A., Recent progress in the synthesis of inorganic nanoparticles. *Dalton T* **2012,** *41* (17), 5089-5120.
23. Kim, D. K.; Zhang, Y.; Voit, W.; Rao, K. V.; Muhammed, M., Synthesis and characterization of surfactant-coated superparamagnetic monodispersed iron oxide nanoparticles. *J Magn Magn Mater* **2001,** *225* (1-2), 30-36.
24. Takami, S.; Sato, T.; Mousavand, T.; Ohara, S.; Umetsu, M.; Adschiri, T., Hydrothermal synthesis of surface-modified iron oxide nanoparticles. *Mater Lett* **2007,** *61* (26), 4769-4772.
25. delMonte, F.; Morales, M. P.; Levy, D.; Fernandez, A.; Ocana, M.; Roig, A.; Molins, E.; OGrady, K.; Serna, C. J., Formation of gamma-Fe2O3 isolated nanoparticles in a silica matrix. *Langmuir* **1997,** *13* (14), 3627-3634.
26. Woo, K.; Hong, J.; Choi, S.; Lee, H. W.; Ahn, J. P.; Kim, C. S.; Lee, S. W., Easy synthesis and magnetic properties of iron oxide nanoparticles. *Chem Mater* **2004,** *16* (14), 2814-2818.
27. Park, J.; An, K. J.; Hwang, Y. S.; Park, J. G.; Noh, H. J.; Kim, J. Y.; Park, J. H.; Hwang, N. M.; Hyeon, T., Ultra-large-scale syntheses of monodisperse nanocrystals. *Nat Mater* **2004,** *3* (12), 891-895.
28. Teng, X. W.; Yang, H., Effects of surfactants and synthetic conditions on the sizes and self-assembly of monodisperse iron oxide nanoparticles. *Journal of Materials Chemistry* **2004,** *14* (4), 774-779.
29. Park, J.; Lee, E.; Hwang, N. M.; Kang, M. S.; Kim, S. C.; Hwang, Y.; Park, J. G.; Noh, H. J.; Kini, J. Y.; Park, J. H.; Hyeon, T., One-nanometer-scale size-controlled synthesis of monodisperse magnetic iron oxide nanoparticles. *Angew Chem Int Edit* **2005,** *44* (19), 2872-2877.
30. Laurent, S.; Forge, D.; Port, M.; Roch, A.; Robic, C.; Elst, L. V.; Muller, R. N., Magnetic iron oxide nanoparticles: Synthesis, stabilization, vectorization, physicochemical characterizations, and biological applications. *Chem Rev* **2008,** *108* (6), 2064-2110.
31. Kim, B. H.; Lee, N.; Kim, H.; An, K.; Park, Y. I.; Choi, Y.; Shin, K.; Lee, Y.; Kwon, S. G.; Na, H. B.; Park, J. G.; Ahn, T. Y.; Kim, Y. W.; Moon, W. K.; Choi, S. H.; Hyeon, T., Large-Scale Synthesis of Uniform and Extremely Small-Sized Iron Oxide Nanoparticles for High-Resolution T-1 Magnetic Resonance Imaging Contrast Agents. *J Am Chem Soc* **2011,** *133* (32), 12624-12631.
32. Woo, K. H., J.; Choi, S.; Lee, H. W.; Ahn, J. P.; Kim, C. S.; Lee, S. W., *Chem. Mater.* **2004,** *16.*
33. Schladt, T. D.; Graf, T.; Tremel, W., Synthesis and Characterization of Monodisperse Manganese Oxide Nanoparticles-Evaluation of the Nucleation and Growth Mechanism. *Chem Mater* **2009,** *21* (14), 3183-3190.
34. Gu, H.; Soucek, M. D., Preparation and characterization of monodisperse cerium oxide nanoparticles in hydrocarbon solvents. *Chem Mater* **2007,** *19* (5), 1103-1110.
35. In *Online Database, ChemSpider, The Royal Society of Chemistry.*
36. Huber, D. L., Synthesis, properties, and applications of iron nanoparticles. *Small* **2005,** *1* (5), 482-501.

37. Peng, S.; Wang, C.; Xie, J.; Sun, S. H., Synthesis and stabilization of monodisperse Fe nanoparticles. *J Am Chem Soc* **2006,** *128* (33), 10676-10677.
38. (a) J. W. M. Bulte, M. M. J. M., *Springer* **2008;** (b) Alivisatos, A. P., *Nat. Biotechnol.* **2004,** *22;* (c) Rosi N. L.; Mirkin, C. A., *Chem. Rev.* **2005,** *105.*
39. Wang, L. Y.; Luo, J.; Fan, Q.; Suzuki, M.; Suzuki, I. S.; Engelhard, M. H.; Lin, Y. H.; Kim, N.; Wang, J. Q.; Zhong, C. J., Monodispersed core-shell Fe3O4@Au nanoparticles. *J Phys Chem B* **2005,** *109* (46), 21593-21601.
40. Insin, N. T., J. B.; Lee, H.; Zimmer, J. P.; Westervelt, R. M.; Bawendi, M. G., *ACS Nano* **2008,** *2.*
41. Crabtree, R. H., *Science* **2010,** *330.*
42. Lee, J. H., Y.; Jun, Y.; Seo, J.; Jang, J.; Song, H.; Kim, S.; Cho, E.; Yoon, H.; Suh, J.; Cheon, J., *Nature Medicine* **2007,** *13.*
43. Song, H. T.; Choi, J. S.; Huh, Y. M.; Kim, S.; Jun, Y. W.; Suh, J. S.; Cheon, J., Surface modulation of magnetic nanocrystals in the development of highly efficient magnetic resonance probes for intracellular labeling. *J Am Chem Soc* **2005,** *127* (28), 9992-9993.
44. Wang, Y. X.; Hussain, S. M.; Krestin, G. P., *Eur. J. Radiol.* **2001,** *11.*
45. Xu C.; Xu K.; Gu, H. Z., R.; Liu, H.; Zhang, X.; Guo, Z.; Xu, B., *J Am Chem Soc* **2004,** *126.*
46. Avdeef, A.; Sofen, S. R.; Bregante, T. L.; Raymond, K. N., Coordination Chemistry of Microbial Iron Transport Compounds .9. Stability-Constants for Catechol Models of Enterobactin. *J Am Chem Soc* **1978,** *100* (17), 5362-5370.
47. Tassa, C.; Shaw, S. Y.; Weissleder, R., Dextran-Coated Iron Oxide Nanoparticles: A Versatile Platform for Targeted Molecular Imaging, Molecular Diagnostics, and Therapy. *Accounts Chem Res* **2011,** *44* (10), 842-852.
48. Amstad, E.; Gillich, T.; Bilecka, I.; Textor, M.; Reimhult, E., *Nano Letters* **2009,** *9.*
49. Sun, C.; Veiseh, O.; Gunn, J.; Fang, C.; Hansen, S.; Lee, D.; Sze, R.; Ellenbogen, R. G.; Olson, J.; Zhang, M., In vivo MRI detection of gliomas by chlorotoxin-conjugated superparamagnetic nanoprobes. *Small* **2008,** *4* (3), 372-379.
50. D'Addio, S. M. K., C.; Akbulut, M.; Beattie, P.; Saad, W.; Herrera, M.; Kennedy M. T.; Prud'homme R. K., *Molecular Pharmaceutics* **2010,** *7* (2).
51. Hermanson, G. T., *Bioconjugate techniques.* Academic Press: San Diego, 1996; p xxv, 785 p.
52. Chung, H. J. L., H.; Bae, K. H.; Lee, Y.; Park, J.; Cho, S. W.; Hwang, J. Y.; Park, H.; Langer, R.; Anderson, D.; Park, T. G., *ACS Nano* **2011.**
53. Wei, H.; Insin, N.; Lee, J.; Han, H. S.; Cordero, J. M.; Liu, W. H.; Bawendi, M. G., Compact Zwitterion-Coated Iron Oxide Nanoparticles for Biological Applications. *Nano Letters* **2012,** *12* (1), 22-25.
54. Eaton, P., Protein thiol oxidation in health and disease: Techniques for measuring disulfides and related modifications in complex protein mixtures. *Free Radical Bio Med* **2006,** *40* (11), 1889-1899.
55. (a) Kuwajima, K.; Ikeguchi, M.; Sugawara, T.; Hiraoka, Y.; Sugai, S., Kinetics of Disulfide Bond Reduction in Alpha-Lactalbumin by Dithiothreitol and Molecular-Basis of Superreactivity of the Cys6-Cys120 Disulfide Bond. *Biochemistry-Us* **1990,** *29* (36), 8240-8249; (b) Burns, J. A.; Butler, J. C.; Moran, J.; Whitesides, G. M., Selective Reduction of Disulfides by Tris(2-Carboxyethyl)Phosphine. *J Org Chem* **1991,** *56* (8), 2648-2650.
56. Lutz, J. F.; Zarafshani, Z., Efficient construction of therapeutics, bioconjugates, biomaterials and bioactive surfaces using azide-alkyne "click" chemistry. *Adv Drug Deliver Rev* **2008,** *60* (9), 958-970.
57. Jung, C. W. J., P., *Magn. Reson. Imaging* **1995,** *13.*
58. (a) Radziuk, D.; Skirtach, A.; Sukhorukov, G.; Shchukin, D.; Mohwald, H., Stabilization of silver nanoparticles by polyelectrolytes and poly(ethylene glycol). *Macromolecular Rapid Communications* **2007,** *28* (7), 848-855; (b) Bakandritsos, A.; Psarras, G. C.; Boukos, N., Some Physicochemical Aspects

of Nanoparticulate Magnetic Iron Oxide Colloids in Neat Water and in the Presence of Poly(vinyl alcohol). *Langmuir* **2008,** *24* (20), 11489-11496.
59. Shultz, M. D. R., J. U.; Khanna, S. N.; Carpenter E. E., *J. Am. Chem. Soc.* **2007,** *129*.
60. Tromsdorf, U. I.; Bruns, O. T.; Salmen, S. C.; Beisiegel, U.; Weller, H., A Highly Effective, Nontoxic T(1) MR Contrast Agent Based on Ultrasmall PEGylated Iron Oxide Nanoparticles. *Nano Letters* **2009,** *9* (12), 4434-4440.
61. Martinez-Perez, M. J.; de Miguel, R.; Carbonera, C.; Martinez-Julvez, M.; Lostao, A.; Piquer, C.; Gomez-Moreno, C.; Bartolome, J.; Luis, F., Size-dependent properties of magnetoferritin. *Nanotechnology* **2010,** *21* (46).
62. Wei, H.; Bruns, O. T.; Chen, O.; Bawendi, M. G., Compact zwitterion-coated iron oxide nanoparticles for in vitro and in vivo imaging. *Integrative Biology* **2013,** *5* (1), 108-114.
63. Serna, C. J.; Morales, M. P., Maghemite (y-Fe203): A Versatile Magnetic Colloidal Material. *Surface and Colloid Science* **2004,** *17*, 27-81.
64. Gross, A. F.; Diehl, M. R.; Beverly, K. C.; Richman, E. K.; Tolbert, S. H., Controlling magnetic coupling between cobalt nanoparticles through nanoscale confinement in hexagonal mesoporous silica. *J. Phys. Chem. B* **2003,** *107* (23), 5475-5482.
65. (a) Choi, J. S.; Lee, J. H.; Shin, T. H.; Song, H. T.; Kim, E. Y.; Cheon, J., Self-Confirming "AND" Logic Nanoparticles for Fault-Free MRI. *J Am Chem Soc* **2010,** *132* (32), 11015-11017; (b) Kim, B. H.; Lee, N.; Kim, H.; An, K.; Park, Y. I.; Choi, Y.; Shin, K.; Lee, Y.; Kwon, S. G.; Na, H. B.; Park, J. G.; Ahn, T. Y.; Kim, Y. W.; Moon, W. K.; Choi, S. H.; Hyeon, T., Large-Scale Synthesis of Uniform and Extremely Small-Sized Iron Oxide Nanoparticles for High-Resolution T-1 Magnetic Resonance Imaging Contrast Agents. *J Am Chem Soc* **2011,** *133* (32), 12624-12631; (c) Bruns, O. T.; Ittrich, H.; Peldschus, K.; Kaul, M. G.; Tromsdorf, U. I.; Lauterwasser, J.; Nikolic, M. S.; Mollwitz, B.; Merkell, M.; Bigall, N. C.; Sapra, S.; Reimer, R.; Hohenberg, H.; Weller, H.; Eychmuller, A.; Adam, G.; Beisiegel, U.; Heeren, J., Real-time magnetic resonance imaging and quantification of lipoprotein metabolism in vivo using nanocrystals. *Nat Nanotechnol* **2009,** *4* (3), 193-201; (d) Freund, B. T., U. I.; Bruns, O. T.; Heine, M.; Giemsa, A.; Bartelt, A.; Salmen, S. C.; Raabe, N.; Heeren, J.; Ittrich, H.; Reimer, R.; Hohenberg, H.; Schumacher, U.; Weller, H.; Nielsen, P., *ACS Nano* **2012,** *6*, 7318.
66. Veiseh, O.; Gunn, J. W.; Zhang, M. Q., Design and fabrication of magnetic nanoparticles for targeted drug delivery and imaging. *Adv Drug Deliver Rev* **2010,** *62* (3), 284-304.
67. Yang, Q. Q.; Liang, J. G.; Han, H. Y., Probing the Interaction of Magnetic Iron Oxide Nanoparticles with Bovine Serum Albumin by Spectroscopic Techniques. *J Phys Chem B* **2009,** *113* (30), 10454-10458.
68. Simberg, D.; Park, J. H.; Karmali, P. P.; Zhang, W. M.; Merkulov, S.; McCrae, K.; Bhatia, S. N.; Sailor, M.; Ruoslahti, E., Differential proteomics analysis of the surface heterogeneity of dextran iron oxide nanoparticles and the implications for their in vivo clearance. *Biomaterials* **2009,** *30* (23-24), 3926-3933.
69. Liu, W. H.; Choi, H. S.; Zimmer, J. P.; Tanaka, E.; Frangioni, J. V.; Bawendi, M., Compact cysteine-coated CdSe(ZnCdS) quantum dots for in vivo applications. *J Am Chem Soc* **2007,** *129* (47), 14530-+.
70. (a) Gao, J. H.; Gu, H. W.; Xu, B., Multifunctional Magnetic Nanoparticles: Design, Synthesis, and Biomedical Applications. *Acc. Chem. Res.* **2009,** *42* (8), 1097-1107; (b) Yoo, D.; Lee, J. H.; Shin, T. H.; Cheon, J., Theranostic Magnetic Nanoparticles. *Acc. Chem. Res.* **2011,** *44* (10), 863-874.
71. Tassa, C.; Shaw, S. Y.; Weissleder, R., Dextran-Coated Iron Oxide Nanoparticles: A Versatile Platform for Targeted Molecular Imaging, Molecular Diagnostics, and Therapy. *Acc. Chem. Res.* **2011,** *44* (10), 842-852.

72. Liu, W. H.; Choi, H. S.; Zimmer, J. P.; Tanaka, E.; Frangioni, J. V.; Bawendi, M., Compact cysteine-coated CdSe(ZnCdS) quantum dots for in vivo applications. *J Am Chem Soc* **2007,** *129* (47), 14530-+.
73. Kelly, K. A.; Shaw, S. Y.; Nahrendorf, M.; Kristoff, K.; Aikawa, E.; Schreiber, S. L.; Clemons, P. A.; Weissleder, R., Unbiased discovery of in vivo imaging probes through in vitro profiling of nanoparticle libraries. *Integr Biol* **2009,** *1* (4), 311-317.
74. (a) Gu, H. W.; Xu, K. M.; Xu, C. J.; Xu, B., Biofunctional magnetic nanoparticles for protein separation and pathogen detection. *Chem Commun* **2006,** (9), 941-949; (b) Ho, D. N.; Kohler, N.; Sigdel, A.; Kalluri, R.; Morgan, J. R.; Xu, C. J.; Sun, S. H., Penetration of Endothelial Cell Coated Multicellular Tumor Spheroids by Iron Oxide Nanoparticles. *Theranostics* **2012,** *2* (1), 66-75; (c) Karlsson, H. L.; Cronholm, P.; Gustafsson, J.; Moller, L., Copper oxide nanoparticles are highly toxic: A comparison between metal oxide nanoparticles and carbon nanotubes. *Chem Res Toxicol* **2008,** *21* (9), 1726-1732.
75. (a) Choi, H. S.; Liu, W.; Misra, P.; Tanaka, E.; Zimmer, J. P.; Ipe, B. I.; Bawendi, M. G.; Frangioni, J. V., Renal clearance of quantum dots. *Nat. Biotechnol.* **2007,** *25* (10), 1165-1170; (b) Wong, C.; Stylianopoulos, T.; Cui, J. A.; Martin, J.; Chauhan, V. P.; Jiang, W.; Popovic, Z.; Jain, R. K.; Bawendi, M. G.; Fukumura, D., Multistage nanoparticle delivery system for deep penetration into tumor tissue. *Proc. Natl. Acad. Sci. U.S.A.* **2011,** *108* (6), 2426-2431.
76. (a) Ai, H.; Flask, C.; Weinberg, B.; Shuai, X.; Pagel, M. D.; Farrell, D.; Duerk, J.; Gao, J. M., Magnetite-loaded polymeric micelles as ultrasensitive magnetic-resonance probes. *Adv Mater* **2005,** *17* (16), 1949-+; (b) Tong, S.; Hou, S. J.; Ren, B. B.; Zheng, Z. L.; Bao, G., Self-Assembly of Phospholipid-PEG Coating on Nanoparticles through Dual Solvent Exchange. *Nano Lett* **2011,** *11* (9), 3720-3726; (c) Mulder, W. J. M.; Strijkers, G. J.; Van Tilborg, G. A. F.; Cormode, D. P.; Fayad, Z. A.; Nicolay, K., Nanoparticulate Assemblies of Amphiphiles and Diagnostically Active Materials for Multimodality Imaging. *Acc. Chem. Res.* **2009,** *42* (7), 904-914.
77. Hricak, H.; Brenner, D. J.; Adelstein, S. J.; Frush, D. P.; Hall, E. J.; Howell, R. W.; McCollough, C. H.; Mettler, F. A.; Pearce, M. S.; Suleiman, O. H.; Thrall, J. H.; Wagner, L. K., Managing Radiation Use in Medical Imaging : A Multifaceted Challenge. *Radiology* **2011,** *258* (3), 889-905.
78. Gore, J. C.; Manning, H. C.; Quarles, C. C.; Waddell, K. W.; Yankeelov, T. E., Magnetic resonance in the era of molecular imaging of cancer. *Magn Reson Imaging* **2011,** *29* (5), 587-600.
79. Zhu, D. R.; Liu, F. Y.; Ma, L. N.; Liu, D. J.; Wang, Z. X., Nanoparticle-Based Systems for T-1-Weighted Magnetic Resonance Imaging Contrast Agents. *International Journal of Molecular Sciences* **2013,** *14* (5), 10591-10607.
80. Harisinghani, M. G.; Barentsz, J.; Hahn, P. F.; Deserno, W. M.; Tabatabaei, S.; van de Kaa, C. H.; de la Rosette, J.; Weissleder, R., Noninvasive detection of clinically occult lymph-node metastases in prostate cancer. *New Engl J Med* **2003,** *348* (25), 2491-U5.
81. Contrast Media: A Market Snapshot. *Contrast Media: A Market Snapshot, GlobalData* **2010.**
82. (a) Seo, W. S.; Lee, J. H.; Sun, X. M.; Suzuki, Y.; Mann, D.; Liu, Z.; Terashima, M.; Yang, P. C.; McConnell, M. V.; Nishimura, D. G.; Dai, H. J., FeCo/graphitic-shell nanocrystals as advanced magnetic-resonance-imaging and near-infrared agents. *Nat Mater* **2006,** *5* (12), 971-976; (b) McDonald, M. A.; Watkin, K. L., Investigations into the physicochemical properties of dextran small particulate gadolinium oxide nanoparticles. *Acad Radiol* **2006,** *13* (4), 421-427; (c) Bridot, J. L.; Faure, A. C.; Laurent, S.; Riviere, C.; Billotey, C.; Hiba, B.; Janier, M.; Josserand, V.; Coll, J. L.; Vander Elst, L.; Muller, R.; Roux, S.; Perriat, P.; Tillement, O., Hybrid gadolinium oxide nanoparticles: Multimodal contrast agents for in vivo imaging. *J Am Chem Soc* **2007,** *129* (16), 5076-5084; (d) Hifumi, H.; Yamaoka, S.; Tanimoto, A.; Citterio, D.; Suzuki, K., Gadolinium-based hybrid nanoparticles as a positive MR contrast agent. *J Am Chem Soc* **2006,** *128* (47), 15090-15091; (e) Na, H. B.; Lee, J. H.; An, K. J.; Park, Y. I.; Park, M.; Lee, I. S.; Nam, D. H.; Kim, S. T.; Kim, S. H.; Kim, S. W.; Lim, K. H.; Kim, K. S.; Kim, S. O.; Hyeon, T.,

Development of a T-1 contrast agent for magnetic resonance imaging using MnO nanoparticles. *Angew Chem Int Edit* **2007,** *46* (28), 5397-5401.
83. Perez-Rodriguez, J.; Lai, S.; Ehst, B. D.; Fine, D. M.; Bluemke, D. A., Nephrogenic Systemic Fibrosis: Incidence, Associations, and Effect of Risk Factor Assessment-Report of 33 Cases. *Radiology* **2009,** *250* (2), 371-377.
84. Tomoya Saitoh; Kazumasa Hayasaka; Yoshiaki Tanaka; Tsutomu Kuno; Nagura, Y., Dialyzability of gadodiamide in hemodialysis patients. *Radiat Med* **2006,** *24*, 445-451.
85. U.S. Food and Drug Administration, FDA Requests Boxed Warning for Contrast Agents Used to Improve MRI Images.
http://www.fda.gov/NewsEvents/Newsroom/PressAnnouncements/2007/ucm108919.htm **2007**.
86. Derrick J. Todd; Anna Kagan; Lori B. Chibnik; Kay, J., Cutaneous Changes of Nephrogenic Systemic Fibrosis. *ARTHRITIS & RHEUMATISM* **2007,** *56*, 3433-3441.
87. Grobner, T., Gadolinium - a specific trigger for the development of nephrogenic fibrosing dermopathy and nephrogenic systemic fibrosis? *Nephrol Dial Transpl* **2006,** *21* (4), 1104-1108.
88. Elmholdt, T. R.; Pedersen, M.; Jorgensen, B.; Sondergaard, K.; Jensen, J. D.; Ramsing, M.; Olesen, A. B., Nephrogenic systemic fibrosis is found only among gadolinium-exposed patients with renal insufficiency: a case-control study from Denmark. *Brit J Dermatol* **2011,** *165* (4), 828-836.
89. Clearinghouse, N. K. a. U. D. I., Kidney Disease Statistics for the United States. **2012.**
90. (a) Harisinghani, M. G.; Barentsz, J.; Hahn, P. F.; Deserno, W. M.; Tabatabaei, S.; van de Kaa, C. H.; de la Rosette, J.; Weissleder, R., Noninvasive detection of clinically occult lymph-node metastases in prostate cancer. *New Engl J Med* **2003,** *348* (25), 2491-U5; (b) Hyeon, T.; Lee, S. S.; Park, J.; Chung, Y.; Bin Na, H., Synthesis of highly crystalline and monodisperse maghemite nanocrystallites without a size-selection process. *J Am Chem Soc* **2001,** *123* (51), 12798-12801; (c) Jun, Y. W.; Lee, J. H.; Cheon, J., Chemical design of nanoparticle probes for high-performance magnetic resonance imaging. *Angew Chem Int Edit* **2008,** *47* (28), 5122-5135.
91. Centers for Medicare & Medicaid Services, 2014 ASP Drug Pricing Files
http://www.cms.gov/Medicare/Medicare-Fee-for-Service-Part-B-Drugs/McrPartBDrugAvgSalesPrice/2014ASPFiles.html.
92. Ittrich, H.; Peldschus, K.; Raabe, N.; Kaul, M.; Adam, G., Superparamagnetic Iron Oxide Nanoparticles in Biomedicine: Applications and Developments in Diagnostics and Therapy. *Rofo-Fortschr Rontg* **2013,** *185* (12), 1149-1166.
93. Schnorr, J.; etal., *Cardiac Magnetic Resonance* **2012,** *184*, 105-112.
94. Choi, H. S.; Liu, W.; Misra, P.; Tanaka, E.; Zimmer, J. P.; Kandapallil, B.; Bawendi, M. G.; Frangioni, J. V., *Nature Biotechnology* **2007,** *25*.
95. Chertok, B.; Moffat, B. A.; David, A. E.; Yu, F. Q.; Bergemann, C.; Ross, B. D.; Yang, V. C., Iron oxide nanoparticles as a drug delivery vehicle for MRI monitored magnetic targeting of brain tumors. *Biomaterials* **2008,** *29* (4), 487-496.
96. (a) Lin, C. R.; Chiang, R. K.; Wang, J. S.; Sung, T. W., Magnetic properties of monodisperse iron oxide nanoparticles. *J. Appl. Phys.* **2006,** *99* (8); (b) Zhang, D. J.; Klabunde, K. J.; Sorensen, C. M.; Hadjipanayis, G. C., Magnetization temperature dependence in iron nanoparticles. *Phys. Rev. B* **1998,** *58* (21), 14167-14170.
97. Choi, H. S. L., W.; Misra, P.; Tanaka, E.; Zimmer, J. P.; Kandapallil, B.; Bawendi, M. G.; Frangioni, J. V. , *Nat. Biotechnol.* **2007,** *25*.
98. Manning, W. J.; Li, W.; Edelman, R. R., A Preliminary-Report Comparing Magnetic-Resonance Coronary Angiography with Conventional Angiography. *New Engl J Med* **1993,** *328* (12), 828-832.
99. Khurana, A.; Nejadnik, H.; Chapelin, F.; Lenkov, O.; Gawande, R.; Lee, S.; Gupta, S. N.; Aflakian, N.; Derugin, N.; Messing, S.; Lin, G.; Lue, T. F.; Pisani, L.; Daldrup-Link, H. E., Ferumoxytol:

a new, clinically applicable label for stem cell tracking in arthritic joints with MRI. *Nanomedicine-Uk* **2013,** *8* (12), 1969-1983.
100. Strijkers G. J. ; Mulder W. J.; Kluza E.; K., N., *Proc. Intl. Soc. Mag. Reson. Med.* **2006,** *14*, 1835.
101. Bennett, C. L.; etal., *Clin Kidney J* **2012,** *5*, 82-88.
102. Catanzaro, V.; Gringeri, C. V.; Menchise, V.; Padovan, S.; Boffa, C.; Dastru, W.; Chaabane, L.; Digilio, G.; Aime, S., A R2p/R1p Ratiometric Procedure to Assess Matrix Metalloproteinase-2 Activity by Magnetic Resonance Imaging. *Angew Chem Int Edit* **2013,** *52* (14), 3926-3930.
103. Magnetic Partilce Imaging brochure. *Koninklijke Philips Electronics N.V* **2014.**
104. Hergt, R.; Dutz, S.; Muller, R.; Zeisberger, M., Magnetic particle hyperthermia: nanoparticle magnetism and materials development for cancer therapy. *J Phys-Condens Mat* **2006,** *18* (38), S2919-S2934.